SIGNAL PROPAGATION

WITHIN A HETEROGENEOUS BACTERIAL COMMUNITY

A Dissertation

Submitted to the Faculty

of

Purdue University

by

Xiaoling Zhai

In Partial Fulfillment of the

Requirements for the Degree

of

Doctor of Philosophy

December 2019

Purdue University

West Lafayette, Indiana

THE PURDUE UNIVERSITY GRADUATE SCHOOL
STATEMENT OF DISSERTATION APPROVAL

Dr. Andrew Mugler, Chair

> Department of Physics and Astronomy

Dr. Gabor Csathy

> Department of Physics and Astronomy

Dr. Paul Muzikar

> Department of Physics and Astronomy

Dr. Sergei Savikhin

> Department of Physics and Astronomy

Approved by:

> Dr. John P. Finley
>> Head of the Graduate Program

ACKNOWLEDGMENTS

TABLE OF CONTENTS

ABBREVIATIONS

WT   wild type

FN   FitzHugh-Nagumo

ThT   thioflavin T

ABSTRACT

Zhai, Xiaoling Ph.D., Purdue University, December 2019. Signal Propagation within a Heterogeneous Bacterial Community. Major Professor: Andrew Mugler Professor.

Reliable signal transmission among cells is important for long-range coordination [1,2]. While higher organisms have designated structures for signal transmission, such as axons, it remains unclear how simpler communities of cells are organized to relay signals [3,4]. Furthermore, many biological systems exhibit spatial heterogeneity, which can interrupt signal propagation. In this thesis, we investigate this problem by modeling the spatial organization and dynamics of electrochemical signaling, and we compare our results to experiments from our collaborators on *Bacillus subtilis* bacterial biofilms. The experiments show that only a fraction of cells participates in signal propagation and that these cells are spatially clustered with a size distribution that follows a power-law decay. These observations suggest that the fraction of participating cells is just at the tipping point between a disconnected and a fully connected conduit for signal transmission. We utilize percolation theory and a minimal FitzHugh-Nagumo-type excitable dynamics model to test this hypothesis, and genetically modified biofilms with altered structure and dynamics to validate our modeling. Our results suggest that the biofilm is organized near the critical percolation point in order to negotiate the benefit and cost of long-range signal transmission. Then, more detailed experiments show that the participation probability is correlated from cell to cell and varies in space. We use these observations to develop an enhanced percolation model, and show using simulations and a renormalization argument that the main conclusions are unaffected by these features. Finally, we use our dynamic model to investigate the effects of heterogeneity beyond the radial wave regime and into the spiral wave regime. We find that spatial correlations in the heterogeneity pro-

mote or suppress spiraling depending on the parameters, a surprising feature that we explain by demonstrating that these spirals form by distinct mechanisms. We characterize the dependence of the spiral period on the heterogeneity using techniques from percolation theory. Taken together, our results reveal that the spatial structure of cell-to-cell heterogeneity can have important consequences for signal propagation in cellular communities.

1. INTRODUCTION

Biological systems such as tissues or bacterial communities often require reliable signal transmission among cells to coordinate actions at a distance [1,2]. In metaozoans, highly specialized and sophisticated structures are dedicated to signal transmission, such as axons that relay electrical signals in the nervous system. Densely-packed bacterial communities have also been shown to benefit from coordinating their metabolic activities over long distances (exceeding hundreds of cell lengths) to cope with nutrient competition [5,6]. However, these bacterial communities face at least two main challenges to coordinating cellular actions at long distances. First, it is unclear how bacterial communities can achieve reliable signal propagation to desired target sites without specialized structures that direct the signals. Second, bacterial communities exhibit significant cell-to-cell heterogeneity that can constitute a key obstacle for long-range signal propagation [7–9]. For example, if only a fraction of cells contributes to signal transmission, the resulting cell-to-cell heterogeneity could cause the propagating signal to die out before reaching its desired target [4, 10–12]. It is thus of importance to determine the heterogeneity of bacterial communities in the context of long-range signal transmission.

The molecular mechanism that underlies signal propagation from the interior of the *Bacillus subtilis* community towards its edge is based on ion channel-mediated electrical cell-to-cell signaling. Specifically, electrical signaling is initiated by cells in the biofilm interior when they experience glutamate starvation during biofilm expansion. This nutrient starvation leads to the opening of the metabolically-gated YugO potassium ion channel and subsequent release of intracellular potassium. Potassium ions cannot diffuse far in the densely packed biofilm community, and thus the resulting local increase in extracellular potassium causes immediately adjacent cells to depolarize, which interferes with their uptake of glutamate, a charged amino acid.

Consequently, the depolarized neighboring cell also experiences glutamate limitation and opens its potassium ion channels, releasing its own potassium ions [13]. This cell-to-cell relay mechanism gives rise to a chain-reaction that propagates the signal to the biofilm periphery. When the electrical signaling reaches the biofilm edge, it halts growth of peripheral cells and thereby reduces their nutrient consumption. This reduction in nutrient consumption allows higher nutrient availability to the stressed cells in the biofilm interior. When nutrient stress in the interior is alleviated, electrical signaling ceases. Now the biofilm resumes growth, which again results in a renewed starvation of interior cells and initiation of the electrical signaling. In this way, the biofilm periodically generates electrical signaling to propagate stress signals from the interior to the periphery of the biofilm to achieve transient starvation relief for interior cells. Electrochemical signaling thus increases the overall fitness of the biofilm against chemical attack by maintaining a viable population of sheltered interior cells.

In addition to the population-level benefit, electrical signaling carries a measurable cost to individual cells, in the form of a reduction in growth rate [5]. This trade-off between single-cell level cost and population-level benefit suggests that perhaps not all cells must carry the burden of relaying the signal for long-range transmission to succeed. But it is unclear what fraction of signaling cells is needed and how these cells would be organized in space to transmit the signal. Notably, signal propagation through inhomogeneous populations is not a problem exclusive to biological systems, but a general question that has been deeply explored in fields such as physics, chemistry and materials science [14–16]. Percolation theory has emerged as the simplest statistical physics approach that directly addresses this problem. Percolation theory has been commonly applied to study signal propagation through various spatially extended heterogeneous systems [17,18]. In particular, percolation denotes the emergence of a connected path (connected cluster of cells) that can span the entire size of a spatially extended system, providing a conduit for signal transmission.

Here, we apply the framework of percolation theory to understand how electrochemical signals are propagated across a heterogeneous *B. subtilis* biofilm community.

By incorporating excitable dynamics into a percolation model, we predict the ability of a biofilm to transmit a signal given different fractions of cells participating in signaling as well as different signaling dynamics. We define cost and benefit functions for each set of signaling parameters and predict a region in parameter space, determined by the critical percolation point, where the signaling benefit outweighs the associated cost. Integration of mathematical predictions with quantitative experimental data from wild type and mutant biofilms suggests that wild type biofilms operate near this region. Our findings are likely to apply to other percolation systems where the benefit exhibits a sharp sigmoidal shape because it is a population-level property and thus determined by the percolation threshold, while the cost is associated with the individual units that comprise the system and thus increases linearly with the fraction of signaling units. We argue that in such systems, the benefit will outweigh the cost near the percolation threshold.

2. THESIS PLAN

Here we brifly describe the basic components of the thesis. Further details on each component will follow in Chapter 3-6.

2.1 Signal percolation within a bacterial community

Reliable signal transmission is of fundamental importance for long-range coordination among cells. However, many biological systems exhibit spatial heterogeneity, which can interrupt signal propagation. Here we show how electrical signaling in a *Bacillus subtilis* biofilm community overcomes organized cell-to-cell heterogeneity to enable reliable signal transmission. We integrated quantitative measurements of genetically modified biofilms with the mathematical framework of percolation theory, to relate the spatial organization of biofilm heterogeneity to signal propagation. This approach revealed signal percolation, in other words, fully connected pathways of signaling cells within heterogeneous biofilms.

2.2 Dynamic model of electrical signaling in a bacterial community

Here we focus on the dynamics of the electrochemical signals in the biofilm using the FitzHugh-Nagumo (FN) model of excitable dynamics [19]. This simple model, commonly used for studying action potential dynamics in neurons, accounts here for excitable dynamics in individual cells as well as for the transmission of signals between neighboring cells. We integrated the FN model with percolation theory by evolving the dynamics on a two dimensional lattice of excitable cells. Simulations show that successful signal propagation through the lattice of cells depends on both the firing duration and the fraction of firing cells. Specifically, high cell-level excitability can

reduce the threshold of signal percolation. Importantly, for the same dynamic parameters, a fraction of firing cells near or above the threshold enables successful signal transmission, while a fraction below the threshold fails to propagate the signal.

2.3 Statistics of correlated percolation in a bacterial community

Despite the success of percolation theory in describing signaling in the biofilm, two key assumptions of percolation theory are violated in this system. First, the probability for a cell to signal is not independent from other cells but instead is correlated with its nearby neighbors. We develop a mechanistic model, in which correlated signaling emerges from cell division, phenotypic inheritance, and cell displacement, that reproduces the experimental results. Second, the fraction of signaling cells is not constant but instead varies from biofilm to biofilm. We find that the first violation does not significantly affect the spatial statistics, which we rationalize using a renormalization argument. We find that the second violation widens the range of signaling fractions around the percolation threshold at which one observes the characteristic power-law statistics of cluster sizes, consistent with our experimental results. We validate our model using a mutant biofilm whose signaling probability decays along the propagation direction. Our results identify key statistical features of a correlated percolating system and demonstrate their functional utility for a multicellular community.

2.4 Spiral wave propagation in communities with spatially correlated heterogeneity

Many multicellular communities propagate signals in a directed manner via excitable waves. Cell-to-cell heterogeneity is a ubiquitous feature of multicellular communities, but the effects of heterogeneity on wave propagation are still unclear. Here we use our minimal FN model to investigate excitable wave propagation in a two-dimensional heterogeneous community. The model shows three dynamic regimes in which waves either propagate directionally, die out, or spiral indefinitely, and we

characterize how these regimes depend on the heterogeneity parameters. We find that in some parameter regimes, spatial correlations in the heterogeneity enhance directional propagation and suppress spiraling. However, in other regimes, spatial correlations promote spiraling, a surprising feature that we explain by demonstrating that these spirals form by a second, distinct mechanism. Finally, we characterize the dependence of the spiral period on the degree of heterogeneity in the system by using techniques from percolation theory. Our results reveal that the spatial structure of cell-to-cell heterogeneity can have important consequences for signal propagation in cellular communities.

3. SIGNAL PERCOLATION WITHIN A BACTERIAL COMMUNITY

Signal transmission among cells enables long-range coordination in biological systems. However, such propagation in extended systems is strongly influenced by spatial heterogeneities [14–16,20] that frequently cause transmission failures [11,21,22]. Such heterogeneities are common in biological systems [7–9], provoking the question of how biologically important signals are robustly propagated. Here we studied this problem in a bacterial biofilm community that benefits from the transmission of electrical signals through a cell-to-cell relay mechanism. We find that only a fraction of cells participates in electrical signaling, and that these cells are spatially clustered with a size distribution that follows a power-law. These traits suggest the emergence of a cluster that can span the entire system, what is known in statistical physics as percolation [23].
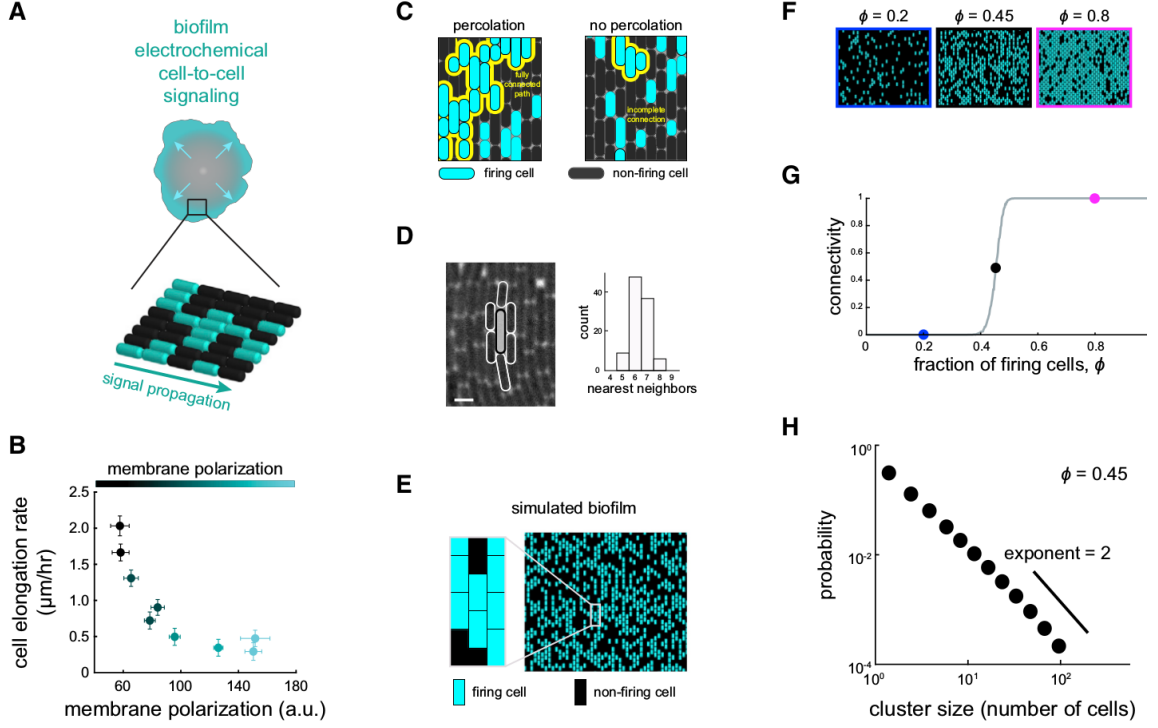
Fig. 3.1. (A) Biofilms undergo electrochemical signaling where the stressed biofilm interior periodically signals cells at the biofilm edge (arrows). Bottom cartoon depicts heterogeneous signaling where some cells participate in signaling (cyan), becoming hyperpolarized, while some cells do not participate (black). (B) Cell elongation rate is inversely correlated with membrane polarization, indicating a cost of electrical signaling activity to individual cells (N = 35 cells, error bars, ± SEM). (C) Percolation theory predicts the emergence of a connected path of firing cells (yellow outline) when the fraction of firing cells exceeds a critical value (left) but not below this critical value (right). (D) Image illustrating a method for counting the number of neighbors for a given cell, highlighted in white (left). Scale bar, 2 mm. Histogram (right) indicates the modal number of nearest neighbors is 6 (N = 100 cells). (E) Using the experimentally constrained nearest neighbor value of 6, firing and non-firing cells are randomly positioned on a two-dimensional lattice with probability ϕ (0.5 in this image). (F) Representative snapshots showing lattice simulations at various values of ϕ. (G) Onset of connectivity (percolation) is predicted when ϕ exceeds 0.45. The ϕ values for the representative images in (F) are indicated on the graph by their respective colored circles. (H) Model-generated cluster size distribution at the percolation threshold ($\phi = 0.45$), where clusters are distributed according to a power law.

3.1 Heterogeneity in signaling

Cells that reside in large, dense communities such as biofilms and tissues must coordinate so that inner cells maintain sufficient access to resources. It was recently discovered that in biofilms of Bacillus subtilis bacteria, this coordination takes the form of a metabolic tradeoff [5]: cells on the interior of the biofilm have limited access to nutrients from the exterior, but periodically withhold a key metabolic compound (ammounium) from the exterior cells. This causes reduced growth of the exterior cells, allowing nutrients to diffuse into the interior. The interior cells then release the ammonium, allowing the exterior cells to resume growth, altogether resulting in growth oscillations. It was further discovered that this process is mediated by an oscillatory electrical signal [13]. Ion channels regulate the release of potassium ions, which diffuse within the extracellular space and trigger subsequent release by nearby cells. This cell-to-cell cascading mechanism results in spatially propagating waves of potassium from the center of the biofilm to the periphery (Fig. 3.1A). These waves coordinate the metabolic activity and have many properties in common with electrical signal transmission in neurons, as well as other types of active cell-cell communication. Here, we demonstrate that participation in the electric signaling comes at a cost to individual cells. Using a fluorescent reporter of membrane potential (the cationic dye thioflavin T, ThT; cyan in Fig. 3.1A), we find that cells with increased potential have a reduced growth rate. Thus, although participating in the signal transmission carries a metabolic benefit to the entire community, it carries a metabolic cost to individual cells. Indeed, we find that as a result, not all cells participate in the signal transmission, leading to cell-to-cell heterogeneity in membrane potential across the population. How to maintain the connected signal path but minimize the fraction of firing cells, is thus a percolation problem.

A

B

C

D
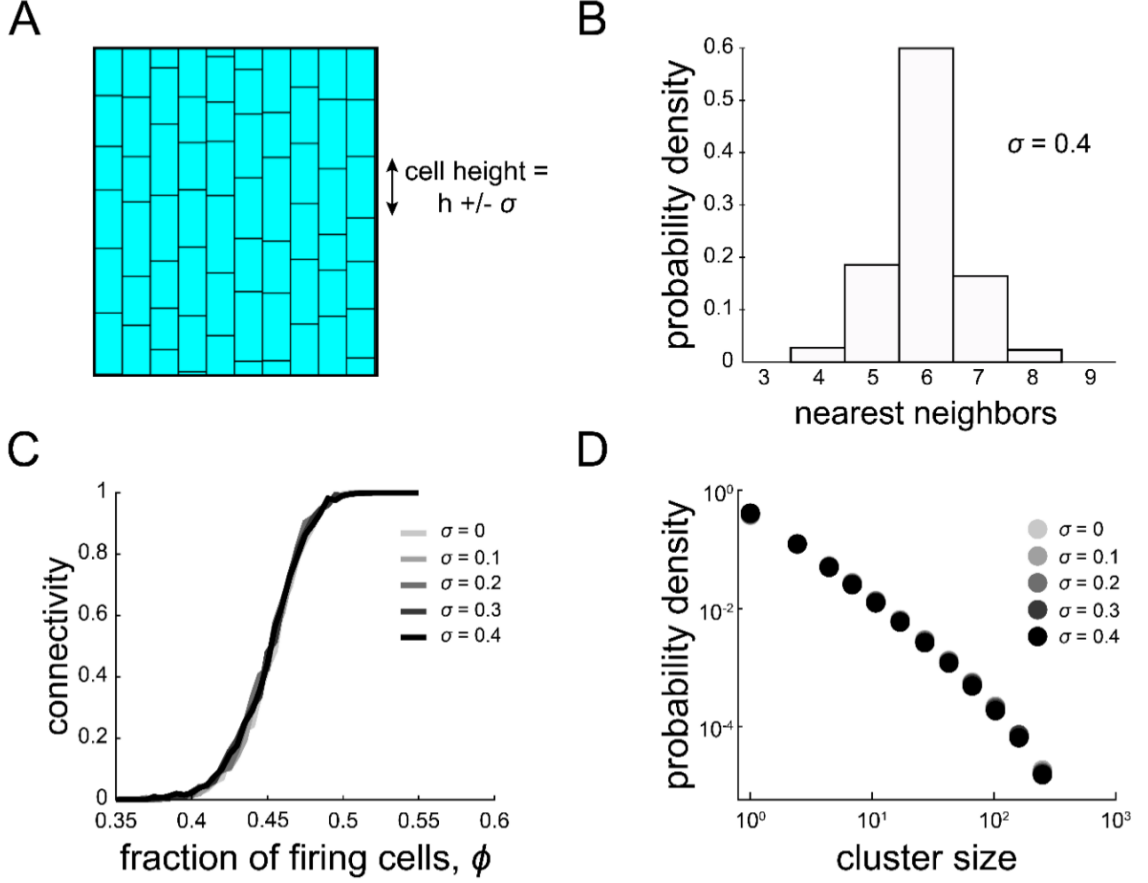
Fig. 3.2. Disordered lattices have the same percolation properties as triangular lattices. Related to Fig. 3.1. (A) A disordered lattice may be created by starting with a triangular lattice and adding random noise (σ) to the height of each cell. (B) This yields a model biofilm with a distribution of nearest neighbor numbers, as shown in this histogram from a $\sigma = 0.4$ biofilm. Some cells have more than 6 nearest neighbors, some fewer. (C) These perturbations do not affect the percolation threshold, as shown in this connectivity plot near the threshold value of $\phi_c = 0.45$. $\sigma = 0$ represents the triangular lattice used in the paper. All curves overlap. (D) For different σ values, the cluster size distribution is not significantly changed near the percolation threshold, as shown in this cluster size distribution plot for different σ values.

3.2   Percolation theory

To describe the connectivity and clustering statistics of firing cells in the biofilm, we simulate cells on a regular two-dimensional lattice. Because cells in the experi-

mental biofilms have a modal value of six neighbors (Fig. 3.1D), we use a triangular lattice, in which cells have six nearest neighbors to which they connect forming triangles [23]. Other lattices that would be good approximations of the biofilm predict similar results to those of the triangular lattice (Fig. 3.2). Percolation theory describes the statistics of lattices in which a fraction ϕ of cells are firing. Firing cells are positioned uniform randomly within the lattice.

Percolation theory predicts that for sufficiently large lattices there is a critical threshold ϕ_c at which several key features occur [23]. First, the probability of a connected path (a contiguous path of firing cells that spans from one side of the lattice to the other) transitions from 0 to 1 at ϕ_c (Fig. 3.1G). Second, at ϕ_c the distribution of cluster sizes becomes a power law, $p(n) \propto n^{-\alpha}$(Fig. 3.1H), where a cluster is defined as a group of contiguous firing cells, and n is the number of cells in the cluster. For two-dimensional infinite lattices, the exponent is $\alpha = \frac{187}{91} \approx 2.05$ [23]). Below ϕ_c the distribution falls off exponentially (Fig. 3.3), and above ϕ_c the distribution acquires weight near the lattice size due to the emergence of a giant cluster (Fig. 3.3).

In all simulations we use a lattice size that corresponds to the approximate observation window in the experiments, L = 35 cell heights by W = 200 cell widths. Connectivity is determined along the shorter direction L, since this is the direction of signal propagation in the biofilm. The asymmetric geometry (L $\neq$ W) is responsible for the deviation of the percolation threshold ($\phi_c = 0.45$) seen in the main figures from the predicted value for a symmetric triangular lattice ($\phi_c = 0.5$) (Stauffer and Aharony, 1994). Fig. 3.1G, 3.1H, and 3.3 were generated using 2000 realizations of the lattice.

Percolation theory predicts the transition of a network from having only localized short-range connections to the emergence of a fully connected path that spans the entire system (Fig. 3.1 C). Specifically, for a defined two-dimensional lattice, the onset of percolation occurs when the fraction of randomly positioned firing cells, ϕ, reaches a critical value, ϕ_c [23]. At this point, the system undergoes a sharp phase transition in its connectivity, giving rise to a connected cluster of firing cells with a size close

to that of the entire system. Below the critical ϕ, too few cells are firing to have sufficient adjacent cells to comprise a fully connected cluster that can span the entire size of the system. Therefore, the probability of having a fully connected conduit for signal transmission across the system remains zero below the critical fraction, but then suddenly jumps to 1 (complete connectivity) as ϕ reaches the critical value. In other words, only when ϕ has reached the critical fraction of firing cells can there be clusters of firing cells that are large enough to span the system. This gives rise to the characteristic sudden phase transitions associated with criticality (Fig. 3.1 G) [23].
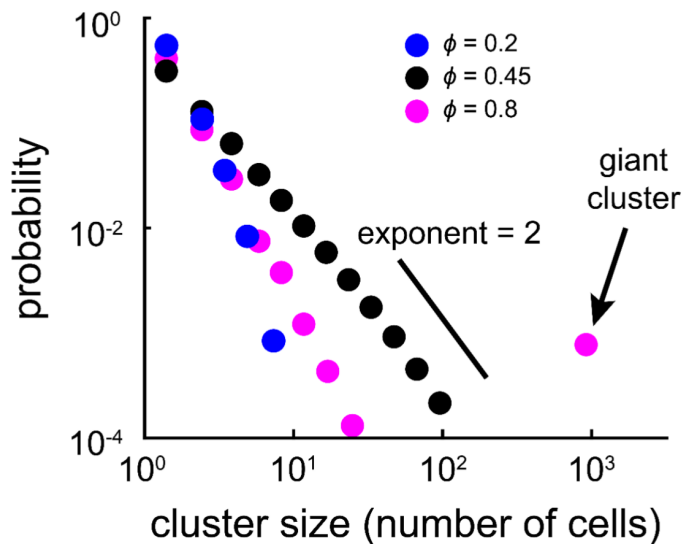
Fig. 3.3. Cluster size distribution in model biofilms changes with fraction of firing cells. Related to Fig. 3.1. Model-generated cluster size distributions for values of ϕ depicted in Figure 3.1 F, G. Only when $\phi = \phi_c$, are clusters distributed according to a power-law (black circles). Above the percolation threshold (magenta circles), a giant cluster develops near the system size.

Given the experimentally constrained size of the system and a modal value of six neighbors for the biofilm cells (Fig. 3.1 D), the model predicts an onset of signaling connectivity (percolation) when the fraction of firing cells in the biofilm reaches 0.45 (Figures 1E−1G, see Fig. 3.2 C for lattices with different numbers of nearest neigh-

bors). At this critical fraction, a firing cell is likely to have at least one immediately adjacent neighbor that is also a firing cell. Consequently, the cluster size distribution of firing cells will have a long tail. In other words, there is always a finite probability of finding a very large, system-spanning cluster of firing cells. Specifically, theory predicts that near this critical percolation threshold, and only near this point, the distribution of cluster sizes formed by signaling cells follows a power-law decay with an exponent of 2.05 [23] (Fig. 3.1H and Fig. 3.3). While the critical value for the fraction of firing cells depends on the specifics of the lattice, such as the number of neighboring cells, the exponent is universal (Fig. 3.2 D). This means that the exponent value is the same for any two-dimensional lattice and thus a very stringent and general prediction [24].

To reiterate, percolation theory thus makes two precise predictions required for signal transmission to become possible in bacterial communities: (1) the fraction of firing cells in the biofilm should be at, or above, the critical percolation threshold of 0.45, and (2) near the percolation threshold, the distribution of cluster sizes formed by firing cells should follow a power-law decay with a slope of 2.05.
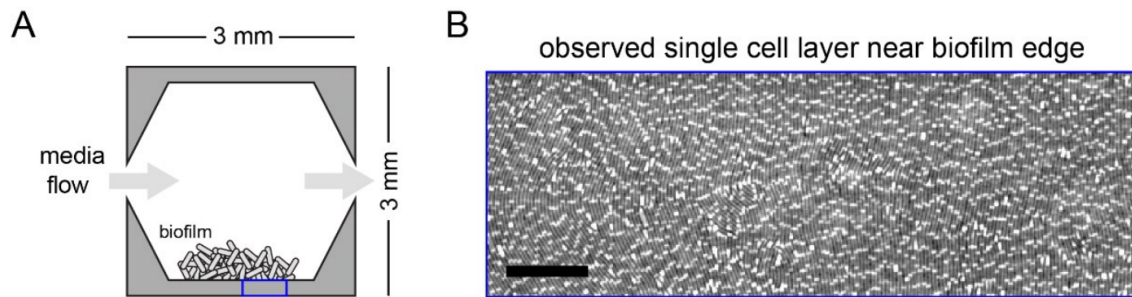
Fig. 3.4. Microfluidic system for single molecule measurements of biofilms. (A) Schematic of microfluidic device used in these experiments. Cells are seeded under a strip of PDMS (bottom) and allowed to grow into a biofilm as media flow is controlled. During biofilm growth, the edge region under the PDMS strip is confined to single cell thickness (e.g. blue rectangle), enabling imaging at single-cell resolution, as shown in the phase image in (B), Scale bar, 20 μm.
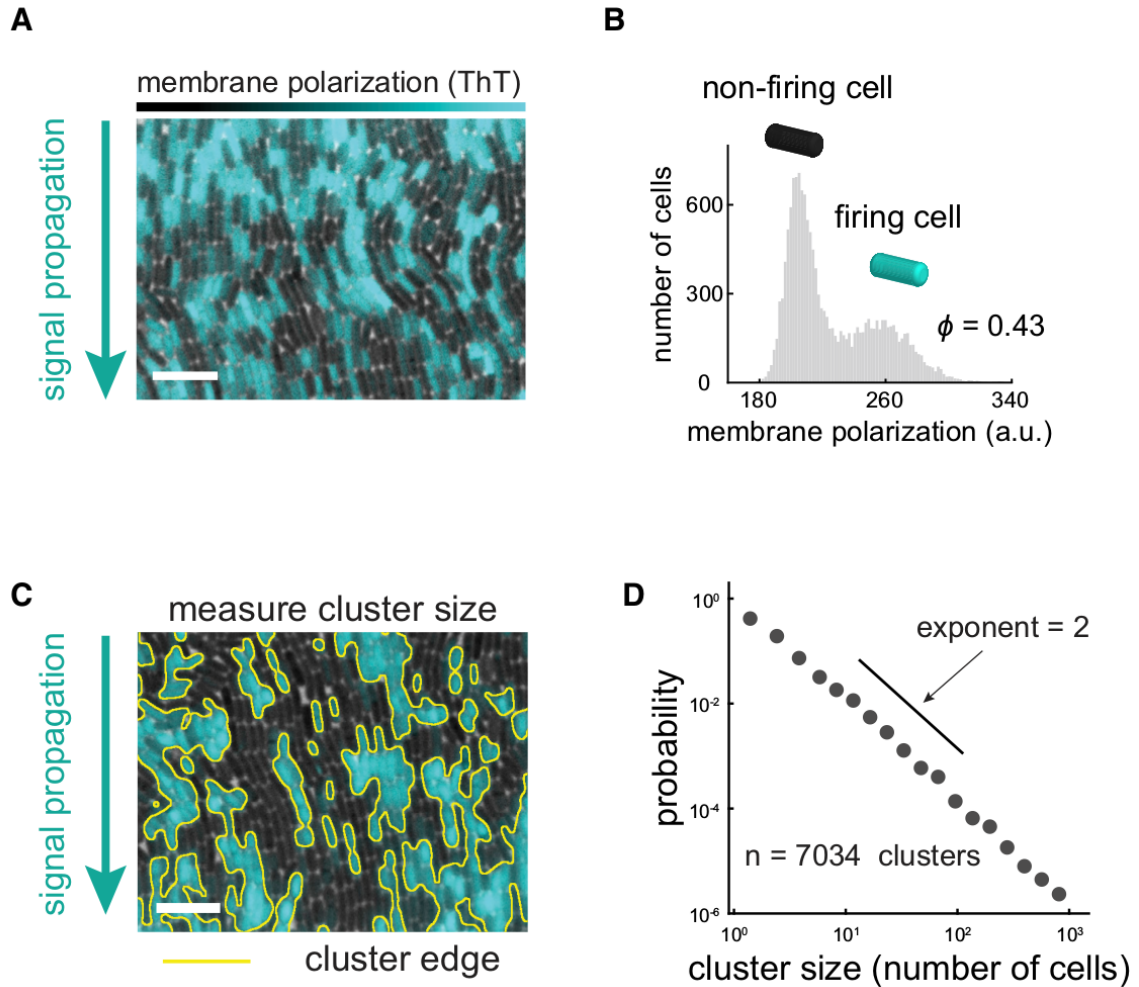
Fig. 3.5. Electrical signaling within biofilms is heterogeneous at the single-cell level. (A) Membrane polarization is heterogeneous at the single-cell level within signaling biofilms. Cyan overlay indicates fluorescence of Thioflavin T (ThT), a cationic membrane polarization reporter. Scale bar, 10 μm (see also Fig. 3.4). (B) Histogram of individual cell ThT intensity (N = 14,936 cells) during a signal pulse. The bimodal shape of the histogram indicates that only a fraction of firing cells (cyan) participate in signaling (0.43 $\pm$ 0.02, mean $\pm$ SEM). (C) Firing cells are spatially clustered within biofilms. Yellow outlines indicate cluster edges identified by image analysis based on ThT fluorescence. Scale bar, 10 μm. (D) Cluster sizes (N = 7,034 clusters) are distributed according to a power-law decay across 3 decades with an approximate exponent of 2. These properties indicate that the arrangement of firing cell clusters within the biofilm can be described by percolation theory.

3.3 Testing percolation theory predictions

To test these theoretical predictions, we determined the spatial arrangement of signaling cells within biofilms. We utilized a microfluidic platform to grow B. subtilis biofilm communities [5] and image them with single-cell resolution (Fig. 3.4). The microfluidic growth chamber contained designated regions where the biofilm was constrained in height to a two-dimensional monolayer. This allowed us to accurately quantify the spatial organization and dynamics of electrochemical signaling at the single-cell level. Furthermore, the two-dimensional geometry allowed us to directly investigate signal transmission in a geometry where the number of neighboring cells is limited, compared with three-dimensional regions of the biofilm where each cell has more than six neighbors on average. The ability of the biofilm to transmit signals even in a monolayer is crucial, since the leading edge of the biofilm is predominantly a monolayer [25] and constitutes the destination for electrochemical signaling (Fig. 3.5A).

To measure membrane potential of individual bacteria within biofilms during electrochemical signaling, we used the previously characterized fluorescent reporter thioflavin-T (ThT), which acts as a Nernstian membrane potential indicator [13]. Specifically, the higher the membrane potential of the cell, the larger the amplitude of the fluorescent ThT signal. Single-cell resolution measurements of the biofilm show that only some cells exhibit pulses in electrical activity, while others do not appear to participate in signaling (Fig. 3.5A, 3.5B, and 3.6). Analysis of all cells reveals a bimodal distribution of membrane potential amplitudes during signal propagation, with the fraction of signaling cells being $\phi = 0.43 \pm 0.02$ (Fig. 3.5B, in agreement with the theoretically predicted percolation threshold. We then measured the spatial distribution of signaling (firing) cells and determined that they were clustered in space (Fig. 3.5C). Moreover, the distribution of cluster sizes follows a power-law decay that extends across three decades and has an exponent of approximately 2 (Fig. 3.5D). Both the fraction of firing cells and the distribution of firing cell cluster sizes are thus

consistent with percolation theory predictions. These results suggest that the spatial organization of signaling cells within the bacterial community may be organized near the percolation threshold.
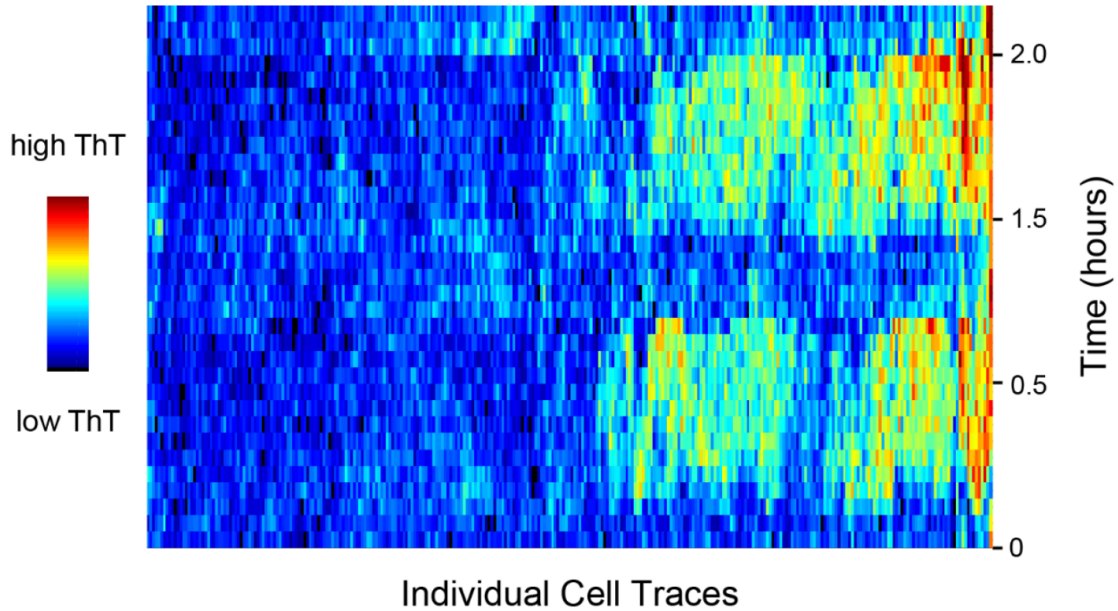
Fig. 3.6. Cells generally do not switch signaling state between pulses. Related to Fig. 3.5. A heatmap of 320 single cell ThT traces from two consecutive pulses in a wild-type biofilm. Each column is a ThT trace from one cell with time increasing along the vertical axis. The traces are organized with hierarchical clustering. The heatmap illustrates that the cells maintain their firing state. Cells that fire on the first pulse have a much higher probability of firing on the second pulse than those that do not and vice versa.
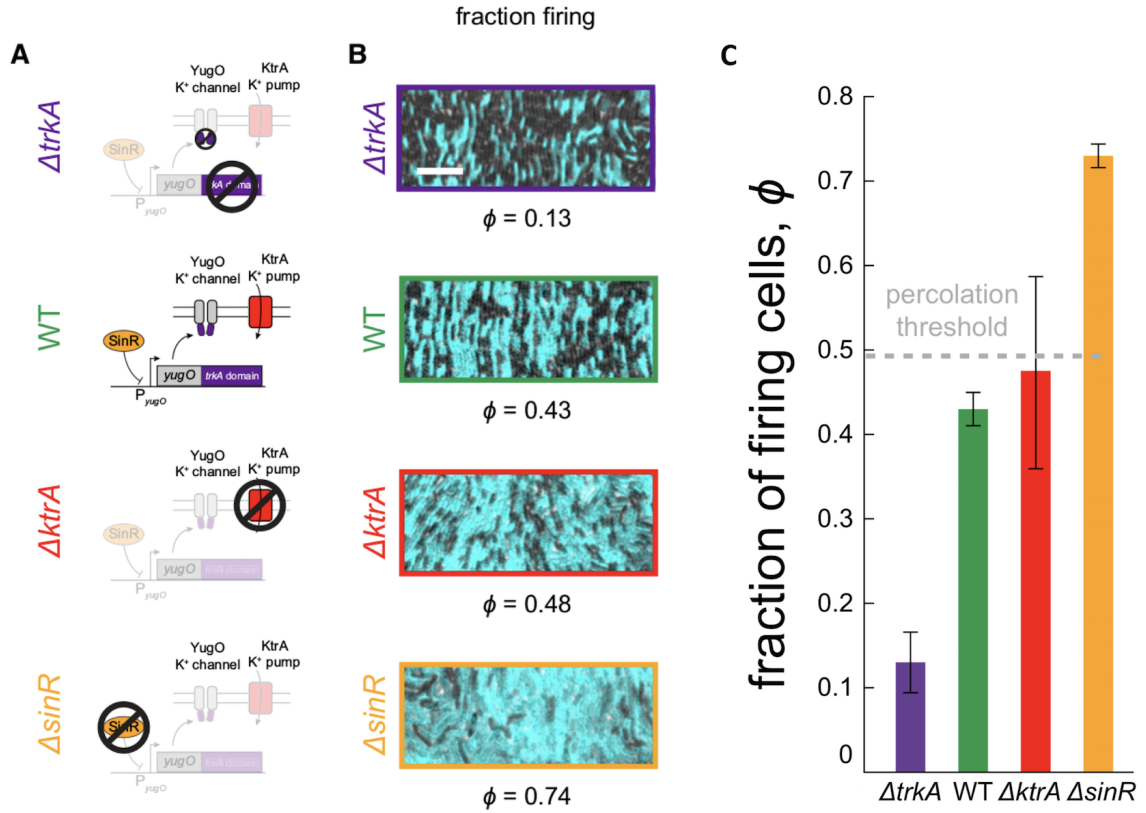
Fig. 3.7. Experimental tuning of firing cell fraction and pulse duration with mutant biofilms. (A) A series of cartoons illustrates the function of genes deleted in the mutant strains. (B) Representative images from time points of peak signaling activity depicting the fraction of firing cells for each strain (cyan ThT fluorescence). Scale bar, 10 μm. (C) Mutant strains exhibit decreased (ΔtrkA, 0.13 ± 0.04, n = 7, mean $\pm$ SEM) or increased (ΔsinR, 0.74 ± 0.04, n = 4 and ΔktrA 0.48 ± 0.11, n = 4) fraction of firing cells relative to wild-type (0.43 ± 0.02, n = 12). Wild-type is near, but slightly below, the percolation threshold, $\phi_c = 0.45$. The ΔtrkA strain (purple), which lacks the gating domain of the potassium channel YugO, is expected to exhibit reduced signaling activity. The ΔsinR mutant (orange) lacks a transcription factor (SinR) that represses expression of YugO, resulting in higher signaling activity.

3.4 Further experimental validation through mutants

We further validated the percolation theory by utilizing three gene-deletion strains that generate biofilms with altered structure (Fig. 3.7 A). ΔtrkA strain lacks the TrkA gating domain of the YugO potassium ion channel and is known to be deficient in electrochemical signaling [13, 26, 27]. Indeed, biofilms formed by the ΔtrkA strain contain a low fraction of firing cells, 0.13 ± 0.04 (mean $\pm$ SEM), compared with 0.43 ± 0.02 observed in wild-type biofilms (Fig. 3.7B and 3.7C). We also utilized a strain that lacks the KtrA potassium pump (ΔktrA) and generates biofilms with a fraction of firing cells similar to wild-type biofilms (0.48 ± 0.11). In contrast, deletion of SinR (ΔsinR), a transcription factor that represses expression of the YugO ion channel [28], results in biofilms with a higher fraction of firing cells, 0.74 ± 0.04 (Fig. 3.7 B and 3.7C). Biofilms formed by these strains thus contain structural differences as defined by differences in the fraction of firing cells. Based on percolation theory, we would predict that since wild-type, ΔktrA, and ΔsinR have fractions at or above ϕ_c, signals should percolate and their amplitudes should be constant in the transmission. In contrast, since ΔtrkA has a fraction which is below ϕ_c, we would predict that the signal cannot reach the periphery and the amplitude should decay very quickly. We see in Fig. 3.8 that these predictions are observed in experiments.

A

WT

ΔtrkA

propagation direction

B
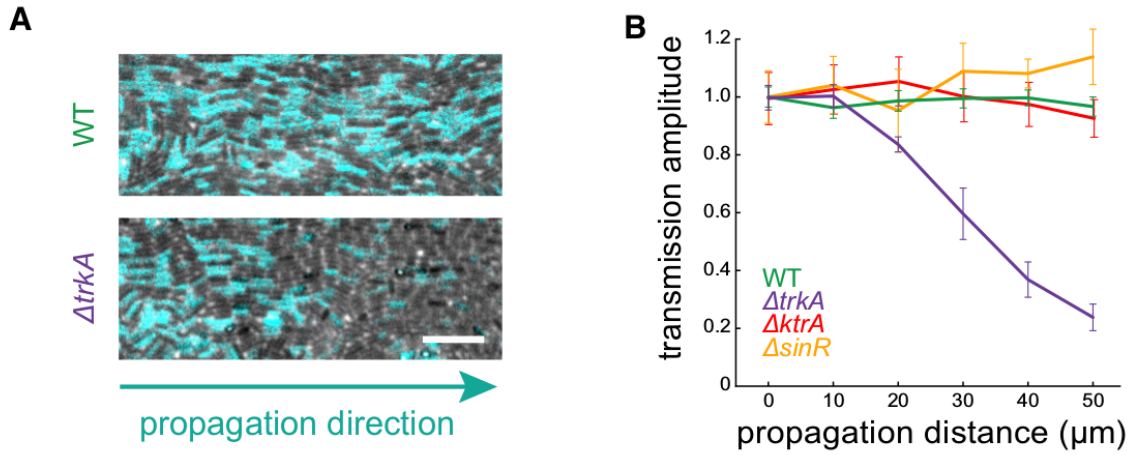
Fig. 3.8. Signal transmission occurs near or above the percolation threshold (A) Phase images with overlaid ThT intensity (cyan) during peak signaling show steady signal propagation in wild-type (top) and spatial signal decay in ΔtrkA (bottom). Scale bar, 10 μm. (B) Transmission amplitude measurements show that wild-type (n = 7), ΔktrA (n = 4), and ΔsinR (n = 4) propagate the signal at a constant amplitude, while Δ trkA (n = 5) does not. Transmission amplitude is defined as the fraction of firing cells at a given position divided by the firing fraction at the beginning of the field of view (error bars, ± SEM).

4. DYNAMIC MODEL OF ELECTRICAL SIGNALING IN A BACTERIAL COMMUNITY

Parts of this chapter have been published as J. W. Larkin, X. Zhai, K. Kikuchi, S. Redford, A. Prindle, J. Liu, S. Greenfield, A. M. Walczak, J. Garcia-Ojalvo, A. Mugler, G. M. Süel, "Signal percolation within a bacterial community," Cell Systems 7(2):137-145, 2018.

Signal transmission is an inherently dynamic process that unfolds over time. In our system, the signal propagates from one cell to the next, where each cell undergoes an excitable pulse (firing) in its membrane potential. The amplitude of the pulse must be sufficiently high to trigger a response in the neighboring cell. It is also important that the cell does not spend excessive time in the firing (and thus non-growing) state, as this would result in unnecessary cost (Fig. 3.1 B). In its simplest form, percolation theory is a statistical framework that does not account for such pulse durations and signaling dynamics of cells. Therefore, we created a model that takes into account both the spatial arrangement of firing cells and the single-cell dynamics during signal transmission.

4.1 Dynamic model

To model the single-cell dynamics of electrical pulses in the biofilm, we utilized the FitzHugh-Nagumo (FN) model (Fig. 4.1A) [19]. The FN model is a minimal model of excitable dynamics and is commonly utilized for studying action potential dynamics in neurons. Our model accounts for excitable dynamics in individual cells as well as the transmission of signals between neighboring cells (Fig. 4.1B, 4.1C). The model contains three parameters: The first is the activation or firing threshold
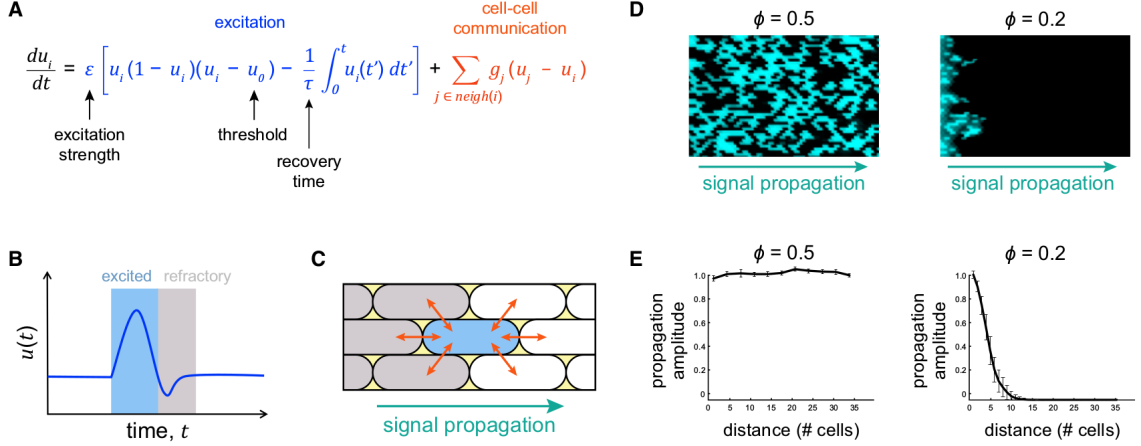
Fig. 4.1. An Excitable Model for Signal Propagation in Biofilms. (A) Model equation combines excitation (blue) and cell-cell communication (orange) to give rise to excitable propagation. The geometric factor g_j is one-fourth at the cell poles and one-half otherwise. (B) A cartoon trace illustrates firing (blue-shading) followed by a refractory period (gray-shading) for a given excitable cell. (C) Cell-cell communication (arrows) allows directional signal propagation from one cell to another. Refractory cells are gray and excited cells are blue. (D) Example model snapshots depict complete signal propagation (direction indicated by arrow) in the regime above the percolation threshold (left, $\phi = 0.5$) and incomplete signal propagation below the percolation threshold (right, $\phi = 0.2$). Both cases have the same values for the dynamic parameters, $\epsilon = 10$, $\mu_0 = 0.01$, $\tau = 300$ for firing cells or $\tau = 5$ for non-firing cells. (E) Example amplitude profiles for the images shown in (D) (error bars indicate $\pm$ SEM, N = 3).

μ_0, which defines the amplitude that an external signal has to exceed in order to trigger a response in the form of a pulse. The second parameter is the recovery time τ, which sets the pulse duration of a given response. The third parameter is the ratio of excitation to cell-to-cell coupling strength, which when sufficiently high supports pulse-coupled wave dynamics. Specifically, we use a discretized Laplacian term to account for the cell-cell communication (Fig. 4.1A and 4.1C). In general, the parameters of this phenomenological model do not have a precise mechanistic interpretation, but rather are calibrated from the experiments as described in section 4.3.

In all dynamical simulations, cells in the first row are initialized with $\mu = 1$ to trigger the excitable wave; all other cells are initialized with $\mu = 0$. We use a lattice of $L' = 100$ rows by $W = 200$ and record from a window of $L = 35$ by $W = 200$ that is positioned just after the first row. Choosing $L' > L$ avoids boundary effects at the last row. We use an absorbing boundary at the last row and reflecting boundaries on the other three sides. To evolve the dynamics, we discretize the FN model in time using the fourth-order Runge-Kutta method with time step $\Delta t = 0.02$. For the cell-cell coupling we use $g_j = \frac{1}{2}$ and $\frac{1}{4}$ (Fig. 4.1A) for the two short-edge and four long-edge neighbors, respectively, corresponding to a rectangular cell with a 2-to-1 aspect ratio on a triangular lattice.

To account for heterogeneity in signaling, a fraction ϕ of cells are firing and are positioned randomly in accordance with percolation theory as described above. All firing cells have the same FN parameters, given below. Non-firing cells have the same parameters as firing cells, except that we reduce the recovery time τ by a factor of 60, which we find strongly reduces the firing propensity of these cells (Fig. 4.1D and 4.1E). We integrated the FN model with percolation theory by evolving the dynamics on a two-dimensional lattice of excitable cells. Simulations show that successful signal propagation through the lattice of cells depends on both the fraction of firing cells and their excitable dynamics. For the same dynamic parameters, a fraction of firing cells near or above the percolation threshold enables successful signal transmission, while a fraction below the threshold fails to propagate the signal (Fig. 4.1D and 4.1E). For the same fraction of firing cells, a low activation threshold (high excitability) enables successful signal transmission, while a high activation threshold (low excitability) prevents signal propagation (Fig. 4.2A). While successful signal transmission depends on the spatial distribution of cell-to-cell heterogeneity, the dynamics of firing cells also play a role and can for example enhance signal propagation (Fig. 4.2B). Without requiring a precise mechanistic description at the molecular level, this phenomenological model generates testable predictions to determine the relationship between a

spatially heterogeneous population of electrically active cells and long-range signal propagation.
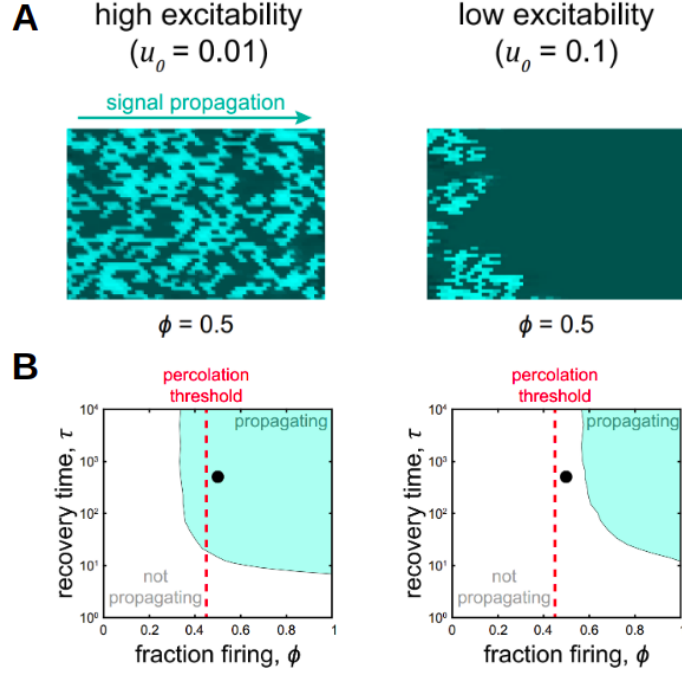
Fig. 4.2. A percolation theory-based model for electrochemical signaling in biofilms accounting for both structure and dynamics. (A) Example model snapshots depicting complete signal propagation (direction indicated by cyan arrow) in the high excitability regime (left) and incomplete signal propagation in the low excitability regime (right). (B) Phase space diagrams defined by recovery time and fraction firing illustrate the parameter region (cyan shading) capable of complete signal propagation. The high excitability regime (left) has a large region of complete signal propagation, while the low excitability regime has a small region of propagation, including areas where propagation fails despite being above the percolation threshold (red dotted line).
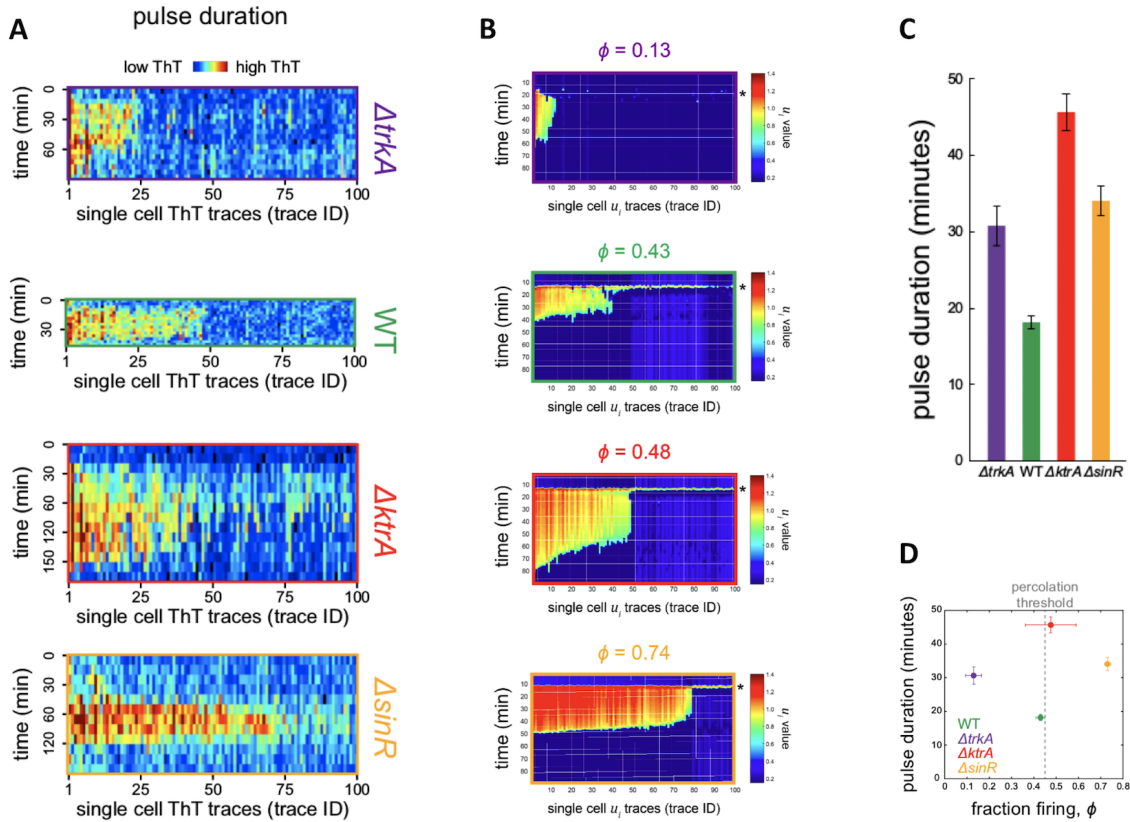
Fig. 4.3. Experimental tuning of firing cell fraction and pulse duration with mutant biofilms. (A) Heatmaps depict single-cell ThT trajectories (N = 100) for all strains. Each column is one cell trace, with time progressing downward. The color scale varies across strains due to baseline fluorescence differences among experiments). (B)The model predicts heterogeneous single-cell time traces. Related to Fig. 4.1. Heatmaps displaying time traces from the model for 100 randomly chosen cells from biofilms with parameters matched to those of the four experimental strains. For each heatmap, a single column is that trace from one cell and time moves from top to bottom. (C) Pulse duration measurements, where pulse duration is defined as the amount of time membrane polarization remains above baseline level. All mutant strains (ΔtrkA 30.6 ± 2.6, 124 cells, three biofilms, and ΔktrA 45.7 ± 2.4, 204 cells, three biofilms, and ΔsinR 34.1 ± 2.0, 165 cells, three biofilms, mean ± SEM) have larger pulse durations than wild-type (18.1 ± 1.0, 383 cells, three biofilms). (D) A phase plot of pulse duration and fraction firing for each strain. ΔtrkA lies below the percolation threshold (dotted line) and ΔsinR above, both with longer pulse duration than wild-type. Wild-type and ΔktrA lie near the threshold, but with different pulse times (error bars, ± SEM).

4.2 Experimental dynamics

To experimentally investigate how biofilm dynamics and spatial structure jointly determine signal transmission and to integrate our findings with mathematical predictions, we utilized the three gene-deletion strains described in the previous chapter that generate biofilms with altered structure and dynamics (Fig. 3.7 A). To characterize the signaling dynamics of each strain, we tracked hundreds of individual cells within the wild-type and genetically modified biofilms and measured their electrical activity during signal transmission (Fig. 4.3 A). We found that the wild-type biofilm has the shortest pulse duration, followed by ΔsinR and ΔtrkA biofilms (Fig. 4.3 C). The absence of the KtrA potassium uptake pump extends the pulse duration, presumably by delaying the recovery of intracellular potassium stores. Notably, wild-type and ΔktrA biofilms have a similar fraction of firing cells, despite their difference in average pulse durations. In contrast, ΔtrkA and ΔsinR biofilms have similar pulse durations, even though ΔtrkA biofilms contain the lowest and ΔsinR biofilms the highest fraction of firing cells (see Fig. 4.3B for single-cell traces from the model). Together, these strains show that the fraction of firing cells and average pulse durations can be separately modulated, allowing us to experimentally explore the phase space defined by the structure and dynamics of biofilms during signal transmission (Fig. 4.3 D).

4.3 Model calibration and validation

We calibrate the parameters of the model (Fig. 4.1A) from the wild type (WT) data in the following way. The fraction of firing cells $\phi = 0.43$ is obtained directly from the experiments (Fig. 3.7C). The excitation strength ϵ must be larger than 1 because otherwise diffusion outpaces excitation and the wave does not propagate; therefore we set $\epsilon = 10$ (note that because the model is phenomenological, the diffusion we describe here is effective and does not correspond to the diffusion of, say, the potassium ions between cells). The threshold u0 must be significantly less than 1 because otherwise

signal from a neighboring cell is insufficient to trigger an excitation and the wave does not propagate; we find that $\mu_0 = 0.02$ suffices (Fig. 4.1D). The recovery time of firing cells $\tau = 300$ is set such that the mean wavelength over 10 simulations is equal to the approximate experimental wavelength of 35 cells. Finally, we convert from dimensionless time t to minutes by equating the mean pulse duration in the simulations to the experimental value (Fig. 4.3C). Pulse duration is averaged over all firing cells and defined as the time over which u > 0.6. See Fig. 4.3B for single-cell time traces from model biofilms with parameters corresponding to each experimental strain.

We validate the model using one of the mutant strains, ΔsinR. This strain has a higher fraction $\phi = 0.74$ of firing cells than WT. We anticipate that because structure and dynamics are connected in the integrated model, changing the fraction of firing cells will also change the mean pulse duration. We test this expectation in the model, setting $\phi = 0.74$ and keeping all other parameters the same as WT. We observe in the simulations that the mean pulse duration rises from 18.1 min (WT) to 33.2 min (ΔsinR). In the experiments, we measure the mean pulse duration for ΔsinR to be 34.1 min, which agrees very closely with the value from the simulations. This validates the model and demonstrates that structure and dynamics are tightly connected in the integrated model.

4.4   Cost and benefit
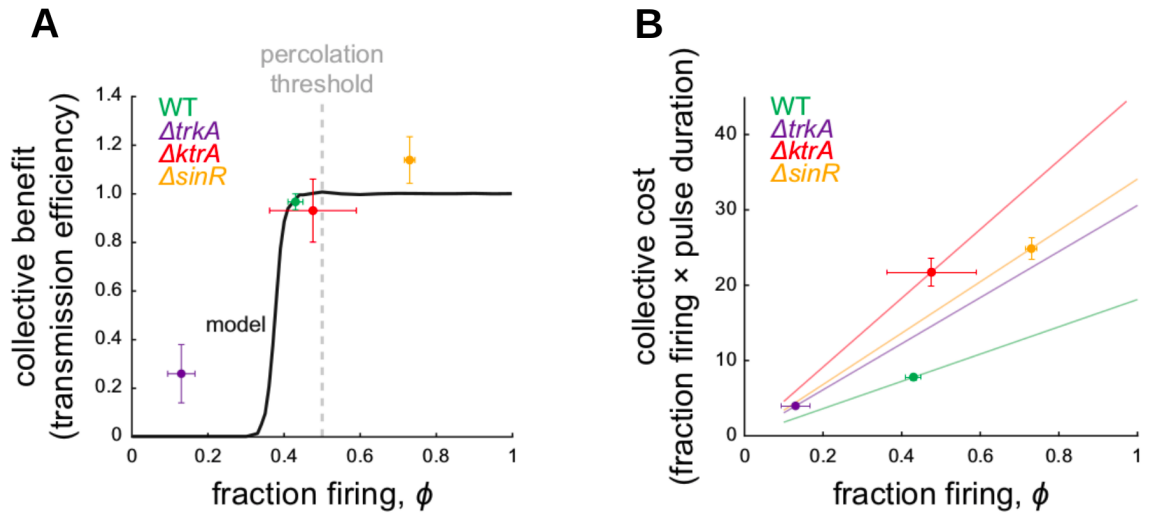
Fig. 4.4. The definition of collective benefit and collective cost. (A) Collective benefit of signaling is defined as the ratio of transmission amplitudes at the biofilm edge and at the beginning of the field of view. Experimental data are shown by points (error bars, $\pm$ SEM). The model output for wild-type parameters (black curve) illustrates the nonlinear nature of collective benefit. (B) Collective cost of signaling is defined as the product of the firing cell fraction, ϕ, and mean pulse time. Experimental data are shown as points (error bars, $\pm$ SEM). Lines represent the cost that would be incurred for each strain given its mean pulse time.

The different combinations of biofilm structure and dynamics that are accessible through genetic perturbations provide an opportunity to investigate why the wild-type cell-to-cell heterogeneity is organized near the critical percolation threshold. Motivated by the notion that biological processes carry not only a benefit, but also a cost, we asked whether the observed spatial organization of wild-type biofilms could be explained by the balance between the benefit and cost of signal transmission. The benefit is defined by the ability to successfully transmit the signal within the biofilm, since such signaling has been previously shown to increase the population-level fitness against chemical attack [5]. Therefore, we can experimentally define the population-

level benefit of signaling based on the fidelity of signal transmission. Specifically, we measure the relative fraction of cells that relay the signal at the two most distant locations within the field of view of our experimental set up (approximately 25 cell lengths in Fig. 4.4 B). We find that the wild-type and mutant biofilms that contain a fraction of firing cells that are near or above the critical percolation threshold can successfully transmit the signal without a decay in its amplitude (Fig. 4.4A and 4.4B). In contrast, the ΔtrkA strain, which has a fraction of firing cells well below the percolation threshold (Fig. 3.7C and 4.3D), fails to transmit the signal (Fig. 4.4A and 4.4B). We can now relate this experimentally determined benefit to the mathematical model based on the fidelity of signal transmission. In particular, the model predicts that as a function of ϕ, the benefit will sharply rise in a sigmoidal manner (Fig. 4.4 C). This sudden rise in the population-level benefit is due to the sudden transition in connectivity at the percolation threshold that enables signal transmission through the system. Beyond the percolation threshold, the benefit is predicted to saturate, since a fully connected conduit for signaling has already been formed, and a further increase in the fraction of firing cells does not qualitatively alter signal transmission. Our experimental data are consistent with the mathematically predicted benefit function (Fig. 4.4 C).
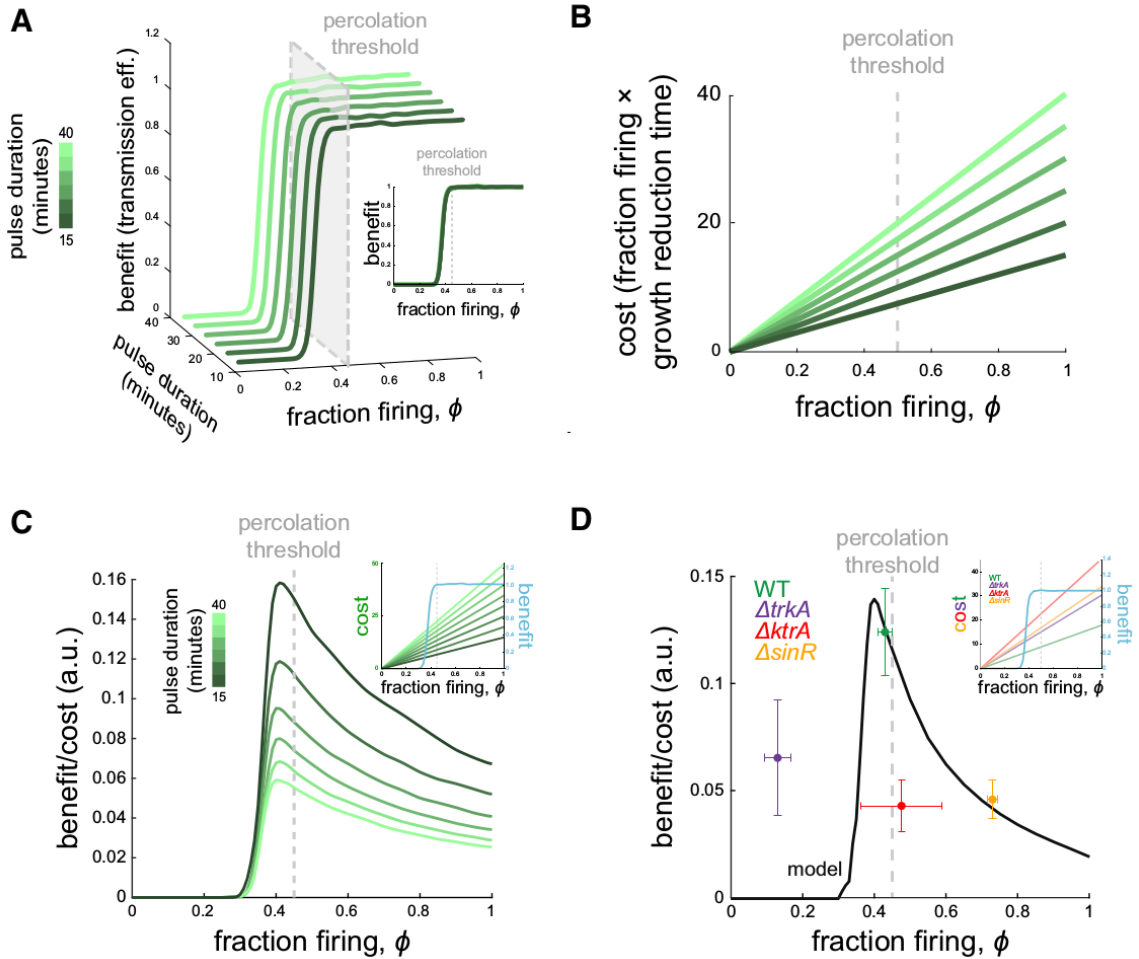
Fig. 4.5. Cost-benefit negotiation in signal transmission. (A) The benefit (transmission efficiency) is plotted for different dynamic parameters as a function of ϕ and resulting pulse time (green color scale). When plotted as a function of ϕ only, the curves line up with benefit rising near the threshold (inset) (B) The cost function is plotted for the corresponding benefit curves from (A). (C) Benefit/cost ratio is plotted as a function of ϕ for the different model curves in (A) and (B), illustrating that, no matter the dynamic model parameters, benefit/cost ratio has a peak near the percolation threshold. This comes from the fact that benefit is highly nonlinear in ϕ, while cost increases smoothly for any set of dynamic parameters (inset). (D) Measured benefit/cost ratio is plotted for each strain (dots, error bars indicate $\pm$ SEM), along with the model output given wild-type parameters (curve). The ratio exhibits a peak due to the linear cost but highly nonlinear benefit, with wild-type near the maximum (see also Fig. 4.6). Inset plot overlays cost and benefit on separate y axes.
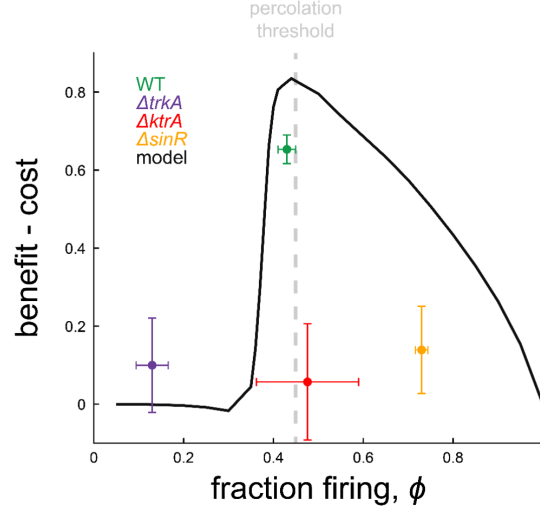
Fig. 4.6. Benefit minus cost yields a peak near the percolation threshold. Related to Fig. 4.5. Benefit minus cost is plotted as a function of fraction of firing cells for experimental data (colored points) and the model with wild-type parameter values (black line). Because benefit is a number between 0 and 1 and cost unbounded, we normalize cost by dividing it by the highest pulse time value measured. The curve bends down at higher ϕ values because the pulse time from the model slightly increases with ϕ for the same τ value. As with benefit divided by cost, this function exhibits a peak near the percolation threshold.

On the other hand, community-level benefit is also associated with a single-cell-level cost. Specifically, firing cells incur a metabolic burden during their electrical activity, as illustrated by the experimentally observed reduction in their cell elongation rate (Fig. 3.1B). Therefore, we define population-level cost as the fraction of firing cells multiplied by their mean signaling duration (Fig. 4.4B). The biofilm incurs greater cost with an increasing number of firing cells, or longer firing durations per cell. Consequently, the cost function increases gradually with the fraction of firing cells. While both the cost and benefit increase as a function of the fraction of firing cells, the smooth rise of the cost function and the sharp sigmoidal shape of the benefit function imply an intriguing cost-benefit relationship (Fig. 4.4A and 4.4B).

To determine the cost and benefit curves in Fig. 4.4 and 4.5, we use the following procedure. In Fig. 4.4A, we vary ϕ while keeping all other parameters as calibrated above. For each ϕ value, we calculate the benefit as the average over 100 simulations of the ratio of the number of firing cells in the final five rows to that in the initial five rows. In Fig. 4.5D, we calculate the cost as the average over 100 simulations of the product of the fraction of firing cells and the mean pulse duration. In Fig. 4.5A$-$C, for each ϕ value, we vary τ in the range 5 to 1000 and measure the mean duration and benefit-to-cost ratio over 30 simulations for each τ value. Then we use linear interpolation to find the benefit-to-cost ratio corresponding to a particular duration. This produces curves of benefit-to-cost ratio vs. ϕ at fixed duration. Finally, we smooth these curves using a Gaussian filter of width 0.01, producing the result in Fig. 4.5C.

We find that the intersection of a nonlinear benefit function and a linear cost function gives rise to a non-monotonic benefit-to-cost relationship. Specifically, the cost rises at a constant rate, while the benefit jumps at the percolation threshold and then saturates (Fig. 4.5A and 4.5B). This suggests that the benefit-to-cost ratio would be highest near the percolation threshold. Indeed, when we plot the benefit-to-cost ratio from the model as a function of the fraction of firing cells, we find a well-defined peak near the percolation threshold (Fig. 4.5C and 4.5D). The result does not depend on the specific way in which benefit and cost are compared: subtracting the cost from the benefit, for instance, also yields a peak near the percolation threshold (Fig. 4.6). The experimentally determined values place the wild-type biofilm near this region defined by the peak, while the mutant biofilms are located away from this region (Fig. 4.5D). These results indicate that the spatial organization of heterogeneity in the wild-type biofilm promotes efficient signal transmission by residing near the percolation threshold.

We note that given a sharp rise in the benefit due to the critical phase transition, the benefit will outweigh the cost near the percolation threshold for a broad range of slopes of the cost function (Fig. 4.5C and 4.5D inset). We also note that linearity is

not required, for as long as the cost function increases gradually, the benefit-to-cost function will always be dominated by the jump in the benefit.

4.5 Discussion

It has been suggested that biological systems across different scales exhibit properties consistent with critical phase transitions. This claim is often justified by the observation of scale-free behaviors, such as power-law dependencies [20, 29, 30]. However, two common concerns are that many biological systems lack an underlying theoretical justification of a critical phase transition, and that the biological purpose of operating near a phase transition is unclear [31]. Here we demonstrate that the spatial organization of a bacterial biofilm is consistent with percolation theory, which is well-known to exhibit a critical phase transition. Specifically, we observe a power law that arises at the predicted value (percolation threshold) and with the predicted exponent. Furthermore, we offer a biological rationale for why the system would be at criticality, by showing that the benefit outweighs the cost near the critical point. The scale-free nature of the critical point also suggests that efficient signal transmission is independent of the size of the biofilm. In other words, signals can be efficiently transmitted as the biofilm grows, without the biofilm having to adjust the fraction of firing cells. It is thus intriguing to speculate that a cost-benefit negotiation may be an organizing principle that drives the biofilm structure to the critical percolation threshold. Our findings suggest that the cost and benefit of signal transmission may play a role in promoting spatial heterogeneity that is organized near criticality. Consequently, the theory developed in statistical physics to describe criticality may also describe the spatiotemporal organization of diverse biological systems and provide a conceptual framework to uncover the functional pressures that drive these systems to phase transition points.

5. STATISTICS OF CORRELATED PERCOLATION IN A BACTERIAL COMMUNITY

Parts of this chapter have been accepted for publication as X. Zhai, J. W. Larkin, K. Kikuchi, S. E. Redford, U. Roy, G. M. Süel, A. Mugler, "Statistics of correlated percolation in a bacterial community," PLoS Computaitonal Biology.

Signal propagation over long distances is a ubiquitous feature of multicellular communities, but cell-to-cell variability can cause propagation to be highly heterogeneous. Simple models of signal propagation in heterogenous media, such as percolation theory, can potentially provide a quantitative understanding of these processes, but it is unclear whether these simple models properly capture the complexities of multicellular systems. In the previous chapters we describe how in biofilms of the bacterium *Bacillus subtilis*, the propagation of an electrical signal is statistically consistent with percolation theory, and yet it is reasonable to suspect that key features of this system go beyond the simple assumptions of basic percolation theory. Indeed, we will show here that the probability for a cell to signal is not independent from other cells as assumed in percolation theory, but instead is correlated with its nearby neighbors. We will develop a mechanistic model, in which correlated signaling emerges from cell division, phenotypic inheritance, and cell displacement, that reproduces the experimentally observed correlations. We find that the correlations do not significantly affect the spatial statistics, which we rationalize using a renormalization argument. Moreover, the fraction of signaling cells is not constant in space, as assumed in percolation theory, but instead varies within and across biofilms. We find that this feature lowers the fraction of signaling cells at which one observes the characteristic power-law statistics of cluster sizes, consistent with our experimental results. We validate the model using a mutant biofilm whose signaling probability decays along

the propagation direction. Our results reveal key statistical features of a correlated signaling process in a multicellular community. More broadly, our results identify extensions to percolation theory that do or do not alter its predictions and may be more appropriate for biological systems.

5.1 Applications of percolation theory to complex biological systems

Long-range signal transmission is central to the function of many multicellular communities. However, cell-to-cell variability within these communities [32, 33] can cause some cells not to participate in signaling, which may degrade or attenuate the signal [34–36]. In physics, signal transmission in the presence of non-propagating agents is the domain of percolation theory [37]. As a result, many investigators have turned to percolation theory to describe signal transmission in multicellular systems. In bacterial communities, percolation theory has been used to predict the scaling laws that result from signal disruption during quorum sensing [38]. In neuroscience, percolation theory has been used to describe (i) the transition from a fully connected to a disconnected electrical network in rat hippocampus cultures [39, 40], (ii) the spatiotemporal structure of viral propagation within astrocyte monolayers [41], and (iii) the transition from conscious to unconscious brain activities during general anesthesia [18]. In pancreatic islets, percolation theory has been used to understand the dependence of calcium wave propagation on the coupling strength of gap junctions between the islet cells [42]. In colonies of *Spirostomum* (an aquatic worm-like cell), percolation theory was recently shown to describe how the propagation of a hydrodynamic cell-to-cell trigger-wave depends on the colony density [43].

In the previous chapters we demonstrated that the transmission of an electrical signal from the interior to the periphery of a biofilm of *Bacillus subtilis* bacteria is consistent with the predictions of percolation theory [36]. In this system, starvation of the interior cells causes release of intracellular potassium, which leads to depolarization and potassium release in neighboring cells, resulting in a cell-to-cell relay wave

that propagates to the biofilm periphery [5, 13, 46]. The signal temporarily prevents peripheral cells from taking up nutrients and thus allows nutrients to diffuse to the interior cells, preserving biofilm viability and increasing its overall fitness [5]. However, it turns out that not all cells participate in the potassium release: we discovered that the fraction of participating cells is near the percolation threshold, and that clusters of participating cells have a size distribution that follows a power law with an exponent predicted by percolation theory [36]. Operating near the percolation threshold allows the biofilm to maintain successful signal transmission while minimizing the number of cells that undergo the costly potassium release [36].

Despite the success of percolation theory as a description of signal transmission within this system, it is reasonable to suspect that several key assumptions of percolation theory may require scrutiny in this and many similar multicellular systems [36]. First, percolation theory assumes that the probability for each cell to participate in signal transmission is independent of other cells. However, in reality it may be that the participation probability of a cell is correlated with that of its neighbors. For example, if the molecular mechanism governing participation is heritable, then one expects the participation of a given cell to be correlated with other cells in its lineage, which are most likely to be nearby in the densely packed biofilm. Second, percolation theory assumes that the participation probability does not vary from one biofilm to another, or from location to location within a biofilm. However, in reality we know that there is variability across biofilms, and particular mutant strains have spatial variability in the participation fraction [36]. These considerations raise the question of when and how percolation theory remains a predictive description of signal transmission in biological systems. Conversely, they suggest a strategy by which deviations from percolation theory would give important insights about the ways in which a biological system differs from the model assumptions [47]. They also raise the broader question of which predictions of a model from statistical physics are dependent on the model details, and which predictions are universal.

Here we use a combination of simulations and experiments to investigate the statistical properties of signal percolation in a bacterial biofilm. We find that signal correlations exist between cells, due to a combination of phenotypic inheritance and spatial proximity of a cell to its progeny. We find that while these correlations lower the percolation threshold, they are not sufficiently long-range to affect the cluster size statistics. Instead, we find that variability in the signaling fraction within and across biofilms affects the statistics by widening the range of fractions at which one observes the power-law distribution of cluster sizes. We validate our findings using a mutant biofilm whose participation fraction decays as a function of propagation distance. Our results demonstrate that certain community-level signaling properties are robust to cell-level features whereas others are not, and we discuss the implications for biofilm function.

5.2   Results

We first review the key features of electrical signaling in the biofilm [5, 13, 36, 46], and those of percolation theory, as these features will motivate our present results. The electrical signal is transmitted by cells across the biofilm in a wave-like manner (Fig 5.1A). We measure the membrane potential of cells during the peak of signal transmission using a fluorescent dye (cyan in Fig 5.1B; see Materials and methods). We previously observed a bimodal distribution of dye intensity across cells [36], which provides a threshold above or below which we define cells as "on" (participating in the signal) or "off" (not participating in the signal), respectively. This observation motivates our use of percolation theory, as percolation theory describes the connectivity and spatial statistics of systems on a lattice in which each cell has a probability ϕ to be on.

We alert the reader that in typical applications of percolation theory, one can measure both the input (the ability of each component to signal or not) and the output (whether or not each component actually participates in the signal as it propagates).
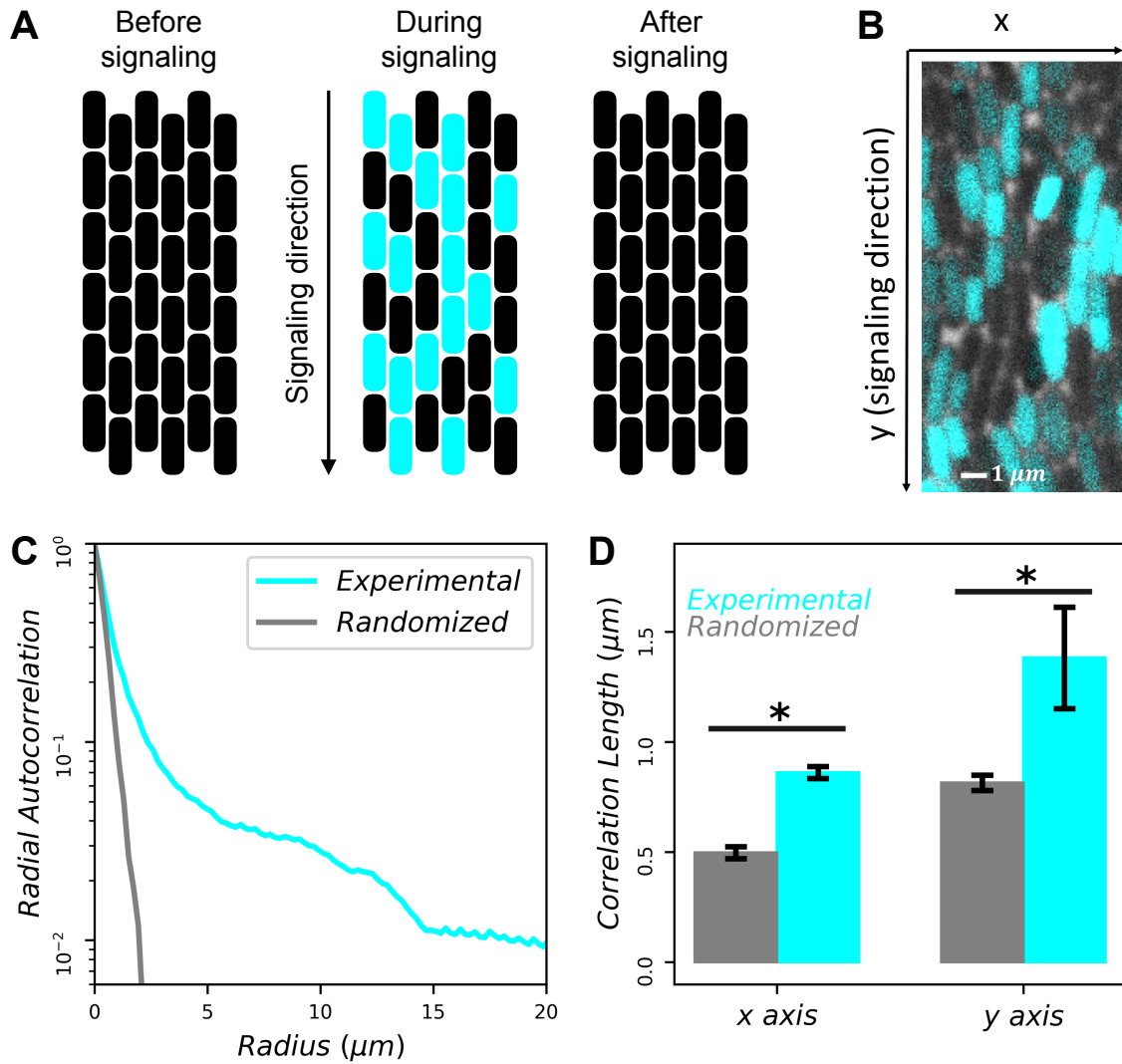
Fig. 5.1. Signaling probability of each cell is correlated with neighboring cells. (A) Cartoon illustrating electrical signaling wave transmitted across biofilm. Cyan represents cells that participate in signaling. (B) Zoomed-in snapshot of cells in biofilm during peak of signal transmission (actual experimental window is approximately 35 cells tall by 230 cells wide). Cyan indicates fluorescence intensity of ThT dye, proportional to membrane potential. (C) Correlation function is longer-range than that from randomized data ($N = 3$ biofilms). (D) Correlations are significantly longer than random both perpendicular (x) and parallel (y) to the signaling direction ($p < 0.001$ and $p = 0.007$ assuming Gaussian errors, respectively).

Here, because we do not know the molecular mechanism that confers the ability to signal, we can only measure the output. Nonetheless, we observe in [36] that (i) isolated clusters participate in signaling, and (ii) the percolation threshold remains predictive of whether the signal propagates across the biofilm. Therefore, as in [36], we conclude that the signaling mechanism is sufficiently short-range that percolation is a relevant criterion for propagation, but sufficiently long-range that the output can be treated as a reasonably good proxy for the input.

Our experiments focus on a 2D cell monolayer at the edge of the biofilm (see Materials and methods). We previously found that cells are most likely to have six neighbors [36]. For an infinite 2D, six-neighbor lattice, percolation theory predicts that (i) a connected path of on-cells emerges above the critical value $\phi_c = 1/2$, and that (ii) at ϕ_c, the distribution of on-cell cluster sizes $P(n)$ becomes a power law [37].

In the experiments, we image a finite window of approximately 35 by 230 cells (see Materials and methods). Finite-size effects can change the value of ϕ_c at which connectivity sets in, which we call ϕ_c^{conn} [37]. Indeed, simulations predict that $\phi_c^{\mathrm{conn}} = 0.45$ in this finite geometry [36]. Finite-size effects should not change the value of ϕ_c at which $P(n)$ becomes a power law, which we call $\phi_c^{\mathrm{pow}} = 1/2$, so long as $\sqrt{n}$ is sufficiently below the smaller lattice dimension. However, at larger n values the distribution will deviate from a power law, even at ϕ_c^{pow}, due to finite-size effects.

We previously observed that the fraction of on-cells in the experiments is $\phi = 0.43 \pm 0.02$ (mean $\pm$ standard error), and that the distribution $P(n)$ of on-cell cluster sizes is a power law over three decades [36]. The fact that $\phi \approx \phi_c^{\mathrm{conn}}$ suggests that the system sits at the connectivity threshold. However, the fact that $\phi < \phi_c^{\mathrm{pow}}$ raises the question of why a power law is observed, particularly one with no apparent finite-size effects at large n. To address this question, as well as the broader question of what features of percolating systems are expected to be robust to the underlying assumptions about the components, we now investigate the effects of signal correlations and of variability in the signaling fraction.

5.2.1 Participation in signaling is spatially correlated

Percolation theory assumes that a fraction ϕ of on-cells are situated randomly in space. However, in the biofilm one might expect that on-cells are spatially co-located, for example if participating in the signal is a heritable phenotype. To determine whether there are spatial correlations in on-cells, we measure the radial autocorrelation function

$$C(r) = \langle s_i s_j \rangle_r - \phi^2, \tag{5.1}$$

where $s = 1$ for on-cells, $s = 0$ for off-cells, and the average is taken over all pixels i and j whose separation is r (see Materials and methods). We find that $C(r)$ is a decreasing function of r, as expected (Fig 5.1C, cyan curve). We then compare $C(r)$ to the autocorrelation function computed with the locations of on-cells randomized. Specifically, we retain the locations of all cells and the number of on-cells, but we randomize which cells are on (as would be the case in percolation theory). We see in Fig 5.1C that $C(r)$ falls off more steeply in this case (gray curve). These results suggest that on-cells are more spatially correlated than expected from random placement.

We next investigate the strength of correlation perpendicular (x) and parallel (y) to the direction of signal transmission (Fig 5.1B). We define the correlation lengths as $\xi_x = \int dx\ C(x)$ and $\xi_y = \int dy\ C(y)$, where $C(x)$ and $C(y)$ are defined as in Eq 5.1 but restricted to separations perpendicular (x) or parallel (y) to the signaling direction, and the integrals run from zero to the maximal separation values. Even in the randomized data, we see that the correlation length is larger in the y direction than in the x direction (compare the gray bars in Fig 5.1D) because cells are longer than they are wide, and the long axis of each cell is generally oriented in the signaling direction (Fig 5.1B). In the actual (non-randomized) data, the correlation lengths are 70% larger than random in both the x and y directions, and both differences are significant ($p < 0.01$; Fig 5.1D). These results suggest that on-cells are significantly correlated both parallel and perpendicular to the signaling direction.

To quantify the correlation at the single-cell level, we consider the conditional probabilities $p(\text{on}|\text{on})$ and $p(\text{off}|\text{off})$, where $p(\text{on}|\text{on})$ is the probability that a cell is on given that the cell above it is also on, and similarly for $p(\text{off}|\text{off})$. We then calculate the order parameter

$$\rho = p(\text{on}|\text{on}) - p(\text{on}|\text{off}), \tag{5.2}$$

where $p(\text{on}|\text{off}) = 1 - p(\text{off}|\text{off})$. With no correlation, we have $p(\text{on}|\text{on}) = p(\text{on}|\text{off}) = \phi$, and therefore $\rho = 0$. With perfect correlation, we have $p(\text{on}|\text{on}) = 1$ and $p(\text{on}|\text{off}) = 0$, and therefore $\rho = 1$. Thus, ρ quantifies the cell-to-cell correlation in the signaling direction on a scale from zero to one.

We estimate the conditional probabilities, and thus ρ, in two ways (Fig 5.2). First, because cell division is usually parallel to the signaling direction, we track division events that occur in between signal pulses (Fig 5.2A; see Materials and methods). We then count the number of times that the top cell has the same or different signaling state as the bottom cell. From this method we obtain $\rho_{\text{div}} = 0.38$ (Fig 5.2B). Second, we estimate the conditional probabilities directly from pairs of cells that are adjacent to each other in the signaling direction during signaling (Fig 5.2C; see Materials and methods). From this method we obtain $\rho_{\text{adj}} = 0.17$ (Fig 5.2D). These results confirm at the single-cell level that spatial correlations exist in the signaling direction ($\rho_{\text{adj}} > 0$) but suggest that these correlations are less strong than those produced directly by division ($\rho_{\text{adj}} < \rho_{\text{div}}$).

5.2.2 Mechanistic model of correlated signaling

To understand the experimental results above, we propose a mechanistic model of spatially correlated cell signaling. We hypothesize that the signaling state is heritable during cell division with a certain probability, and that cell displacement can occur at the leading edge as the biofilm grows. The assumption that cells possess a signaling state variable is supported by the observation that a cell generally does not switch its on/off signaling behavior between successive pulses in the experiments [36].
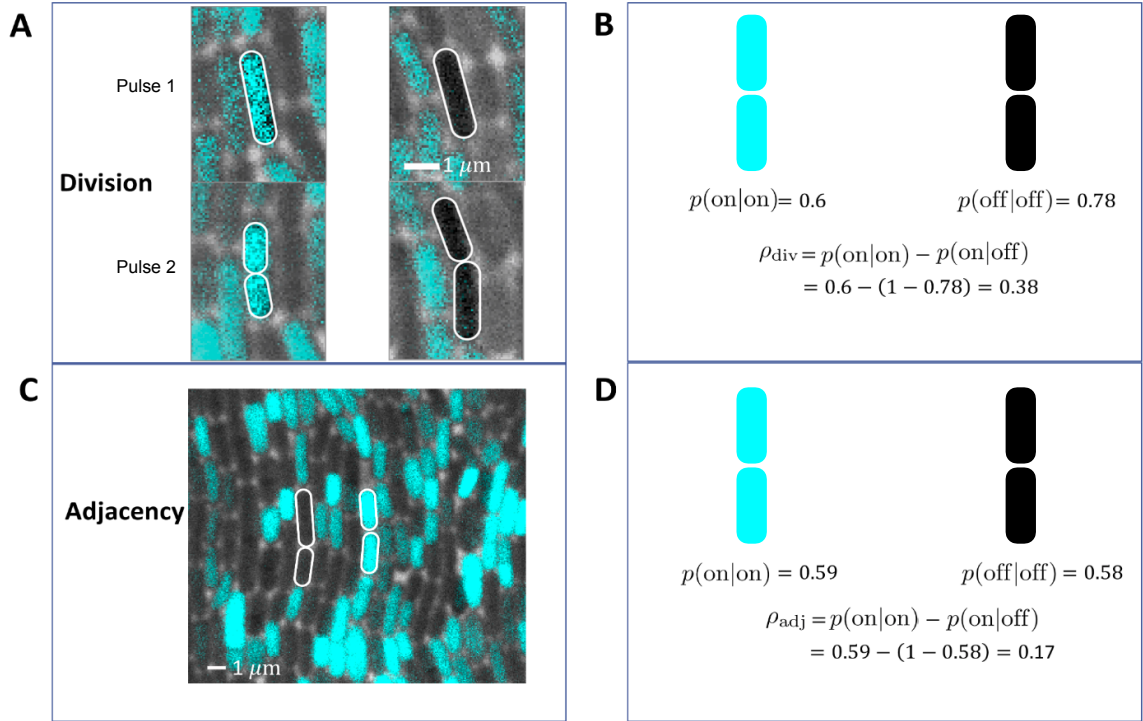
Fig. 5.2. Order parameter ρ quantifies degree of spatial correlations. (A, B) Lineage-tracing experiments yield $\rho_{\mathrm{div}} = 0.38$ ($N = 49$ division events). (C, D) Spatial analysis of the biofilm images yield $\rho_{\mathrm{adj}} = 0.17$ ($N = 51$ cell pairs).

Specifically, as shown in Fig 5.3A, we generate a 2D, six-neighbor lattice of rectangular cells with aspect ratio 2 (the approximate experimental value) in the following way. Each cell divides after a time τ drawn from a Gaussian distribution with mean $\bar{\tau}$ and standard deviation $\delta\tau$. The "mother" cell (m) retains its location and signaling state, while the "daughter" cell (d) occupies one of the eligible neighboring locations with equal probability. Eligibility requires that the neighboring location either be empty or be occupied by a neighboring cell (n) that, when displaced by the division along the same direction, would occupy an empty location (Fig 5.3A). Because the biofilm is growing downward, the eligible locations will most often be the location directly below and, with lower probability, the locations below-and-to-the-right and below-and-to-the-left. The signaling state of the daughter, given that of the mother, is determined from the division parameter ρ_{div} and the fraction of on-cells ϕ according to

$$p(\mathrm{on}|\mathrm{on}) = \phi + \rho_{\mathrm{div}} - \phi\rho_{\mathrm{div}}, \tag{5.3}$$

$$p(\mathrm{on}|\mathrm{off}) = \phi - \phi\rho_{\mathrm{div}}, \tag{5.4}$$

which follow from Eq 5.2 and the requirement that the fraction of on-cells remains ϕ throughout the process (see Materials and methods). We produce a 100 by 230 lattice of cells by initializing the top row randomly and generating the next 99 rows according to the above mechanism. Then we remove the top 55 and bottom 10 rows, leaving a 35 by 230 cell window as in the experiments. This procedure allows the mechanism to achieve statistical steady state and focuses on the biofilm edge as in the experiments.

We find that the spatial statistics are not sensitive to the value of $\delta\tau/\bar{\tau}$, so long as it is greater than zero, and therefore we average our results over the range $0 < \delta\tau/\bar{\tau} < 1$ (rejecting samples with $\tau \leq 0$ for large $\delta\tau$). We also find that allowing neighbor cell displacement is necessary to generate correlations in the x direction, but that allowing two or more levels of displacement does not qualitatively change the results. Thus,
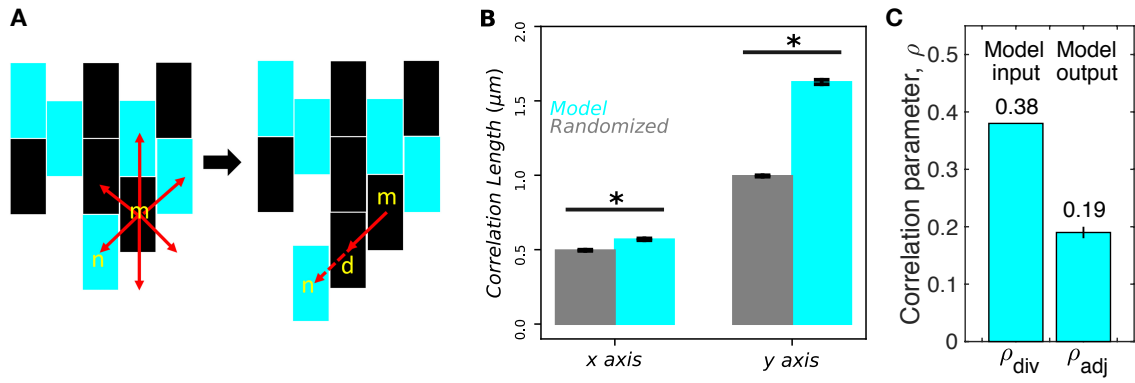
Fig. 5.3. Mechanistic model of correlated signaling captures experimental features. (A) Mother cell (m) produces daughter cell (d) with correlated signaling state at any neighboring site at which a maximum of one neighbor cell (n) is displaced. Cyan indicates that cell has the ability to signal. (B) Correlations are significantly longer than random both perpendicular (x) and parallel (y) to the signaling direction ($N = 10^4$ lattices; $p < 0.001$ for both assuming Gaussian errors). Compare to experiments in Fig 5.1D. (C) Stochasticity in division times, neighbor selection, and cell displacement reduces correlation parameter from $\rho_{\mathrm{div}} = 0.38$ to $\rho_{\mathrm{adj}} = 0.19 \pm 0.01$, close to experimentally measured $\rho_{\mathrm{adj}} = 0.17$ ($N = 10^4$ lattices).

the only parameters in the model are ϕ and ρ_{div}, which we set from the experiments as $\phi = 0.43$ [36] and $\rho_{\mathrm{div}} = 0.38$ (Fig 5.2B).

This model, with no free parameters, makes three predictions. Specifically, the model predicts that (i) the correlation length in the x direction is significantly different from random (Fig 5.3B), (ii) the correlation length in the y direction is significantly different from random (Fig 5.3B), and (iii) the spatial correlation parameter measured from adjacent cells in the y direction after the biofilm is generated is $\rho_{\mathrm{adj}} = 0.19 \pm 0.01$ (Fig 5.3C). The model output ρ_{adj} is reduced from the model input $\rho_{\mathrm{div}} = 0.38$ due to the stochasticity in division times, neighbor selection, and cell displacement. Predictions (i) and (ii) are consistent with the experiments, as both the x and y correlation lengths were found to be significantly different than random (Fig 5.1D). Prediction (iii) is also consistent with the experiments, as ρ_{adj} was measured to be 0.17 (Fig 5.2D), which is very close to 0.19 ± 0.01. We have also checked that these predictions remain unchanged when accounting for the fact that on-cells grow more slowly than off-cells [36] (see Materials and methods). The fact that all three predictions are validated by the experiments gives us confidence that the model captures the basic underlying mechanism, especially because it has no free parameters.

5.2.3   Impact of correlations on spatial statistics

We now use our mechanistic model to investigate the impact of the spatial correlations on the statistical properties of the biofilm. First we focus on the connectivity: the probability, over an ensemble of simulated biofilms, that a connected path of on-cells exists from the top to the bottom of the lattice. The connectivity is expected to show a sharp transition from 0 to 1 at a critical fraction of on-cells ϕ_c^{conn}. For an infinite lattice (in 2D with six neighbors), $\phi_c^{\mathrm{conn}} = 1/2$ [37]. Finite-size effects reduce the sharpness, but ϕ_c^{conn} can still be defined as the value of ϕ for which the connectivity is 50%. For a finite lattice of the approximate size of the experimental window (35 cells tall by 230 cells wide), without correlations, we previously found
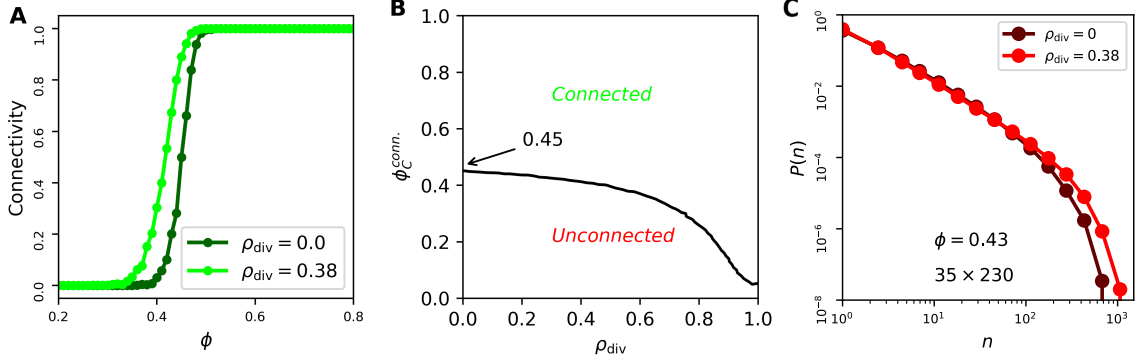
Fig. 5.4. Spatial correlations increase connectivity but have little effect on cluster size distribution. (A) Connectivity, defined as probability that a connected path of on-cells exists, occurs at lower on-cell fraction ϕ as correlation parameter ρ_{div} increases ($N = 10^3$ lattices). (B) Connectivity threshold ϕ_c^{conn}, defined as ϕ value for which connectivity is 50%, decreases with ρ_{div} ($N = 10^3$ lattices). (C) Spatial correlations ($\rho_{\mathrm{div}} = 0.38$) have little effect on distribution, in particular not removing exponential rolloff at large n ($N = 10^3$ lattices).

$\phi_c^{\mathrm{conn}} = 0.45$ [36] (Fig 5.4A, dark green curve). With correlations, using our mechanistic model with $\rho_{\mathrm{div}} = 0.38$, we find $\phi_c^{\mathrm{conn}} = 0.4$ (Fig 5.4A, light green curve). More generally, the connectivity threshold is shown as a function of ρ_{div} in Fig 5.4B, and we see that as $\rho_{\mathrm{div}} \to 1$, ϕ_c^{conn} becomes close to zero, even with the stochasticity inherent in the model. Thus, spatial correlations reduce the connectivity threshold. This makes sense, as correlations increase the probability of connected on-cells, particularly in the signaling direction, and this lowers the fraction of on-cells needed to created a connected path.

Second, we investigate the impact of correlations on the distribution of on-cell cluster sizes $P(n)$. The distribution is expected to become a power law at a critical fraction of on-cells $\phi_c^{\mathrm{pow}} = 1/2$ [37]. The experimental fraction of on-cells is $\phi = 0.43 \pm 0.02$ [36], which is lower than ϕ_c^{pow}. In simulations without correlations, at $\phi = 0.43$, we find that $P(n)$ acquires a rolloff (when viewed on a log-log scale) at large n (Fig 5.4C, dark red curve). The rolloff indicates that the distribution is
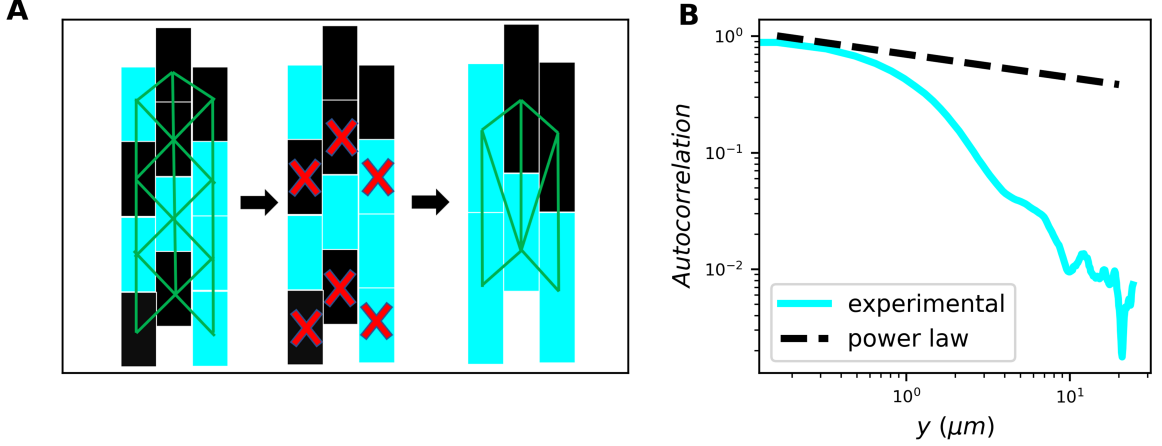
Fig. 5.5. Short-range correlations do not affect critical properties. (A) Illustration of the renormalization argument: upon site decimation, lattice remains triangular, ϕ remains constant, and ρ vanishes. (B) Correlation function in experiments is short-range, i.e. sub-power-law ($N = 3$ biofilms).

becoming more exponential, as expected for $\phi < \phi_c^{\mathrm{pow}}$. However, in experiments, we find that $P(n)$ maintains the power law dependence, with no rolloff, for three decades, i.e. out to $n = 10^3$ [36]. Because we have seen that spatial correlations preserve connectivity at lower ϕ (Fig 5.4A and B), we hypothesize that correlations may also preserve the power law dependence of $P(n)$ at lower ϕ, and thus explain the experimental observation. Surprisingly, using our mechanistic model, we find that the spatial correlations actually have little impact on $P(n)$ (Fig 5.4C, light red curve): the rolloff is slightly shifted to larger n, but it is certainly still present over the three-decade range.

Why do correlations not change the distribution of cluster sizes? Renormalization-group arguments from statistical physics imply that correlations do not change the critical properties of percolation theory if the correlations are sufficiently short-range [48]. The intuitive reason can be seen from a site-decimation procedure [37], as illustrated in Fig 5.5A. We imagine decimating every other cell in each column (red X's), with each remaining cell expanding to fill the space below it. Fig 5.5A illustrates

that the resulting lattice remains triangular (green lines). Furthermore, because the probability of any cell to be on is ϕ, the fraction of on-cells remains ϕ after decimation. Finally, the new conditional probabilities after one round of decimation are

$$p_1(\text{on}|\text{on}) = p(\text{on}|\text{on})p(\text{on}|\text{on}) + p(\text{on}|\text{off})p(\text{off}|\text{on}), \tag{5.5}$$

$$p_1(\text{on}|\text{off}) = p(\text{on}|\text{on})p(\text{on}|\text{off}) + p(\text{on}|\text{off})p(\text{off}|\text{off}), \tag{5.6}$$

which follow from the rules of probability and the assumption that the signaling state is spatially Markovian, i.e. the daughter is conditionally independent of the grandmother given the mother (see Materials and methods). As a result, the correlation parameter after one round of decimation is $\rho_1 = p_1(\text{on}|\text{on}) - p_1(\text{on}|\text{off}) = [p(\text{on}|\text{on}) - p(\text{on}|\text{off})]^2 = \rho^2$, where the first and last steps use the definition in Eq 5.2, and the middle step inserts the expressions in Eqs 5.5 and 5.6 and simplifies (see Materials and methods). Similarly, after j rounds of decimation we have $\rho_j = \rho^{j+1}$. Because $\rho < 1$, we see that $\rho_j \to 0$ as $j \to \infty$. Thus, correlations vanish upon repeated rounds of decimation and renormalization. This means that correlations are not expected to change the critical properties of the distribution $P(n)$.

The above intuition only holds if the correlations are sufficiently short-range. Indeed, Eqs 5.5 and 5.6 assume that the correlations are minimally short-range, namely Markovian. In general, it has been shown that spatial correlations only affect the critical properties of percolation if they decay as a power law, specifically $C(r) \sim r^{-a}$ with $a > 3/2$ in 2D [48]. As seen in Fig 5.5B, the correlations in the experimental data are much shorter-range than a power law. This suggests that the spatial correlations that we observe in the biofilm are not sufficiently long-range to affect the critical properties. Together with Fig 5.4C, we conclude that spatial correlations are not sufficient to explain the experimentally observed power law dependence of $P(n)$ over three decades [36].
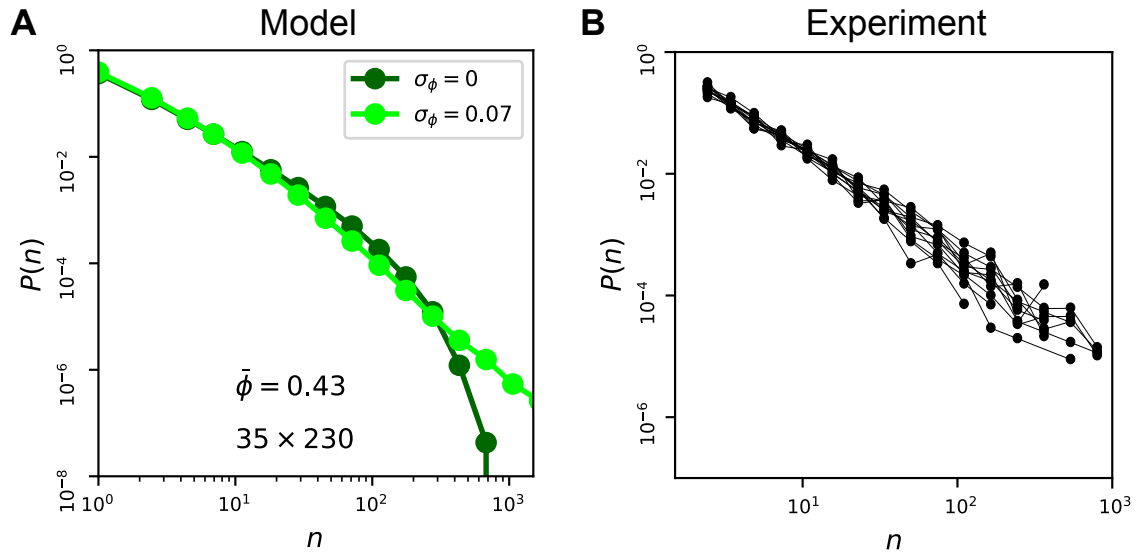
Fig. 5.6. Variability can lead to power-law cluster size distribution, even for $\phi < \phi_c$. (A) In the model, variability ($\sigma_\phi = 0.07$) removes rolloff, causing distribution to approach a power law over three decades ($N = 10^3$ lattices). (B) In the experiments, cluster size distributions from individual biofilms are power laws without significant rolloff, consistent with the model and the fact that we find variability in ϕ within each biofilm. Data are from [36] but processed individually for each biofilm.

5.2.4 Variability in signaling fraction

If spatial correlations cannot explain the experimentally observed power law, then what can? An important feature of the experiments that is not yet accounted for in the model is variability in the on-cell fraction ϕ. In particular, we previously observed that the value of ϕ is roughly Gaussian-distributed across 12 experiments with a mean of $\bar{\phi} = 0.43$ and a standard deviation of $\sigma_\phi = 0.07$ (from which the standard error of $0.07/\sqrt{12} = 0.02$ comes) [36]. Furthermore, subdividing each of the 12 images into either 4 or 16 equal parts with the same aspect ratio as the original image, we find that the standard deviation of the on-cell fraction across parts (averaged over all images) is $\sigma_\phi = 0.04$ (4 parts) or $\sigma_\phi = 0.05$ (16 parts). Because these values are similar to $\sigma_\phi = 0.07$, we conclude that the variability within biofilms is similar to that across the biofilms in our experiments.

Some variability is expected from finite size effects. Specifically, in basic percolation theory, binomial statistics dictate that the standard deviation in the fraction of on-cells would be $\sqrt{N\bar{\phi}(1 - \bar{\phi})}/N = 0.006$ in a biofilm with $N = 230 \times 35 = 8{,}050$ cells. In our mechanistic model with correlations, we find that the standard deviation is similarly small at 0.009. Because these values are much smaller than the observed value of $\sigma_\phi = 0.07$, we conclude that the experimental variability is not due to finite size effects alone, and that it is necessary to explicitly incorporate variability into the model.

To incorporate variability in the on-cell fraction, we draw ϕ for each lattice from a Gaussian distribution with standard deviation σ_ϕ. Because we have found that correlations have little effect on $P(n)$, we set $\rho_{\text{div}} = 0$ from here on for simplicity. The results are shown in Fig 5.6A, and we see that σ_ϕ has a significant effect on the distribution. In particular, for the experimental value $\sigma_\phi = 0.07$ (light green curve), we see that the exponential rolloff at large n is removed, extending the range of the power law out to $n \sim 10^3$ as observed in the experiments [36]. The intuitive reason is that a non-negligible fraction of lattices in the ensemble have ϕ values that are equal

to or greater than $\phi_c^{\text{pow}} = 1/2$. Because ϕ is higher in these lattices, they are more likely to have large clusters. Therefore, these lattices dominate the distribution at large n, eliminating the rolloff. Thus, variability in ϕ effectively widens the range of mean $\bar{\phi}$ values at which a power law distribution is observed. We conclude that the experimental variability in ϕ across biofilms is sufficient to explain the experimentally observed power-law distribution.

Given that we also observe variability in ϕ within each biofilm, to a similar degree as across biofilms, our results suggest that the cluster size distribution from each biofilm individually should follow a power law without a significant rolloff. We test this hypothesis in Fig 5.6B by plotting the data from [36] separately for each biofilm. We see that indeed, the individual distributions follow a power law and do not exhibit significant rolloffs. This result suggests that the mechanism we identify above, in which variability widens the range of $\bar{\phi}$ values at which a power law distribution is observed, also applies at the individual biofilm level. It also shows that the signaling statistics are reproducible from biofilm to biofilm and thus constitute a plausible feature that could be optimized for biological function, as suggested in our previous work [36].

5.2.5   Model validation using mutant strain

How can our model be tested with further experiments? One approach is to investigate a system with a different fraction of on-cells and see if our model remains valid. We previously investigated mutant strains with different on-cell fractions, including the $\Delta trkA$ strain with $\bar{\phi} = 0.13$ and $\sigma_\phi = 0.1$ [36]. As seen in Fig 5.7A (light red curve), basic percolation theory ($\rho_{\text{div}} = 0$, $\sigma_\phi = 0$) predicts that a system with an on-cell fraction of $\phi = 0.13$ would have a distribution of cluster sizes $P(n)$ that is entirely exponential because 0.13 is much lower than $\phi_c^{\text{pow}} = 1/2$.

However, the $\Delta trkA$ strain differs from the wild-type strain in that the fraction of on-cells is not constant in space, but rather decreases along the signaling direction
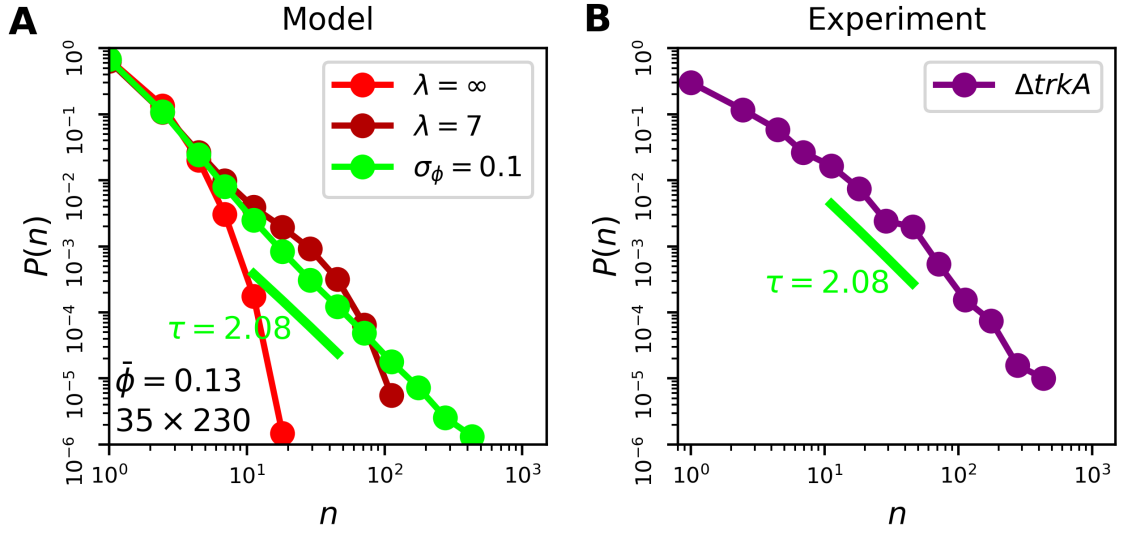
Fig. 5.7. Statistics of mutant $\Delta trkA$ strain. (A) We progressively incorporate into the model the on-cell fraction $\phi = 0.13$ (light red), the exponential decay of ϕ in space with lengthscale $\lambda = 7$ cells (dark red), and the variability $\sigma_\phi = 0.1$ across lattices (green); $N = 10^3$ lattices for each. Resulting $P(n)$ is a power law (green) despite the fact that 0.13 is far below the critical fraction $\phi_c^{\text{pow}} = 1/2$. (B) $P(n)$ from $\Delta trkA$ data is a power law whose exponent is consistent with the model ($N = 7$ biofilms).

[13] with a characteristic lengthscale of approximately $\lambda = 15$ μm, or about 7 cell lengths [36]. The reason for this decrease is likely that the signal is dying out due to insufficient connectivity of the on-cells. Therefore, in the case of $\Delta trkA$, the on-cell fraction is sufficiently low that it is likely no longer fair to treat the ability to signal and the act of signaling as equivalent. Because the experiments measure the latter, we must incorporate the observed spatial decrease into the model. To do so, we allow the on-cell fraction to vary as $\phi(y) = \phi_0 e^{-y/\lambda}$, where ϕ_0 is set to ensure that the spatial average of $\phi(y)$ is 0.13. We see in Fig 5.7A (dark red curve) that this feature extends the distribution to larger cluster sizes n. The reason is similar to that given above regarding variability: the portions of the lattice in which ϕ is large contain large clusters, thereby enhancing the large-n region of the distribution. Nonetheless, the distribution remains far from a power law in its shape. In particular, a clear exponential rolloff at large n is evident.

If our main finding above is correct, namely that variability in ϕ across biofilms is a crucial determinant of the shape of $P(n)$, then we must also incorporate into our model the variability $\sigma_\phi = 0.1$ observed for the $\Delta trkA$ strain. Indeed, we find that doing so has a major effect on the distribution (Fig 5.7A, green curve). Specifically, it removes the exponential rolloff, resulting in a power-law distribution over almost three decades. This is a strong prediction, considering that $\bar{\phi} = 0.13$ is much lower than $\phi_c^{\text{pow}} = 1/2$, and that without variability the shape is far from a power law even after accounting for the spatial dependence of ϕ.

To test this prediction, we measure the distribution of cluster sizes in the $\Delta trkA$ biofilms (see Materials and methods). Remarkably, the result, shown in Fig 5.7B, is a distribution that is roughly a power law over almost three decades, consistent with the model prediction. Indeed, the power-law exponent of 2.08 estimated from the model distribution via a maximum likelihood technique [49] (Fig 5.7A, green line) is consistent with the slope of the experimental distribution (Fig 5.7B, green line). This result validates our model. In particular, it supports the finding that variability of

the signaling fraction across biofilms plays an important role in shaping the statistical properties of the system.

5.3   Discussion

We have shown that experimentally observed features that go beyond the basic assumptions of percolation theory, including spatial correlations, variability, and non-uniformity, can have important consequences for signal propagation in a bacterial community. Using a mechanistic model that accounts for heritability in a cell's propensity to participate in signaling, we have found that signal correlations decrease the fraction of participating cells needed to create a connected path, but have little effect on the cluster statistics. In contrast, variability of the signaling fraction across samples has a significant effect on the statistics, in particular producing a power-law distribution of cluster sizes at signaling fractions lower than the expected critical fraction from percolation theory. We have validated our model using a mutant strain, in particular finding that both spatial decay and variability in the signaling fraction play a crucial role in shaping the signaling statistics.

While it is clear that key observations in this system are consistent with the predictions of percolation theory (the fraction of signaling cells is very close to the percolation threshold and the cluster size distribution is a power law with the predicted exponent [36]), the deviations of other observations from either the assumptions or predictions of percolation are informative. In this sense we recognize that percolation theory is a toy model. Searching for deviations from the toy model has allowed us infer information about the biological mechanism, and then develop an enhanced model of percolation that is more appropriate. The approach of extending percolation to account for additional features has a long precedent in the literature, with variants including explosive percolation, fractional percolation, correlated percolation, bootstrap percolation, invasion percolation, and dynamical percolation [37, 50–52]. This approach is particularly suitable for biological systems, where it is natural to expect

that the complexities of growth and variability may lead to observable departures from simple textbook models.

We found that incorporating the experimentally observed variability and non-uniformity of the signaling fraction into the model was necessary to explain the experimentally observed cluster statistics, whereas incorporating the experimentally observed spatial correlations in signaling was not necessary. This finding implies that certain underlying cell-level features are important in determining population-level statistical properties, whereas others are not. This categorization is consistent with approaches from statistical physics, particularly the renormalization group, which reflect the powerful notion that some microscopic details are relevant for macroscopic properties, whereas others are provably irrelevant [53]. Indeed, we explain our finding that spatial correlations do not affect the cluster statistics using a renormalization argument (Fig 5.5), as well as more rigorous known results from statistical physics [48]. It will be interesting to see what other cell-level features are relevant or irrelevant for capturing population-level phenomena in multicellular systems.

Finite-size effects play an important role in our results. In particular, our experimental observation window is sufficiently short in the signaling direction ($\sim$35 cells) that spatial correlations in the signaling propensity have a measurable effect on the connectivity (Fig 5.4). Yet, the window is wide perpendicular to signaling ($\sim$230 cells), and thus the window area is sufficiently large that the spatial correlations have little effect on the cluster size statistics. This choice of window size follows from experimental constraints and the desire to focus on the short and wide biofilm edge, where signaling is most important for function [13]. Nonetheless, it is an interesting open question how the finite size and aspect ratio of the system set distinct thresholds for the relevance of correlations to the connectivity and cluster statistics.

Dimensionality also plays an important role in our results. Because the biofilm edge is where cell growth is most pronounced, it is quasi-two-dimensional. In fact, biofilm formation itself can promote cell spreading via osmotic pressure gradients, reducing biofilm thickness at the edge [25]. This is part of the reason that our experi-

ments have focused on 2D monolayers of cells. However, the properties of percolation theory depend critically on the dimensionality of the system [37]. In particular, the percolation threshold is generally smaller in 3D lattices than in 2D lattices [54] because there are more available paths for the signal to take. This observation suggests that a lower fraction of signaling cells is necessary in the bulk of the biofilm than at its edge. This prediction is currently difficult to test, as the 2D nature of our experiments is crucial for obtaining fluorescence data at the single-cell level.

The fact that spatial correlations lower the connectivity threshold in a finite system may help explain why the biofilm has an on-cell fraction of $\phi = 0.43 \pm 0.02$ [36]. Naive percolation theory predicts a threshold of $\phi_c^{\text{conn}} = 1/2$ [37], which the biofilm does not meet. Accounting for finite-size effects lowers the threshold to $\phi_c^{\text{conn}} = 0.45$ [36] (Fig 5.4), which the biofilm barely meets. Accounting for correlations lowers the threshold further to $\phi_c^{\text{conn}} = 0.4$ (Fig 5.4), which the biofilm meets comfortably. Thus, correlations provide some leeway between the necessary and observed signaling fraction, which may enhance the reliability of signaling or make it robust to errors.

Although we observe spatial correlations in the signaling activity, and the results are consistent with a model that assumes inheritance of the signaling state, the inheritance mechanism is unknown. *B. subtilis* cells maintain phenotypic states through intracellular genetic networks that control the production of transcription factors [55]. Moreover, the inheritance of transcription factors and other proteins from parent cells to daughter cells can maintain specific cell types for several generations, leading to spatial correlation of cell types [56]. *B. subtilis* has even evolved the ability to control the number of generations over which certain phenotypic states are maintained [57]. Such a mechanism could drive the inheritance in signaling state that we observe here: the transcription factors regulating the expression or non-expression of ion channels, for example, could be passed from mother to daughter.

The effect of spatial correlations is a general question that is fundamental to understanding multicellular behaviors. The length scale of cell-to-cell signaling in quorum sensing bacterial communities depends on the establishment of spatial corre-

lations [38,58]. Moreover, the interplay of spatial heterogeneity and signaling length-scale dictates the cooperativity of pathogenic *Pseudomonas aeruginosa* biofilms [59]. In eukaryotes, spatial correlations in cell-substrate interactions can drive collective cell migration [60], which is a fundamental multicellular process in tissue development [61] and wound healing [62].

Our study motivates further avenues of exploration in both statistical physics and cell biology. In statistical physics, our study motivates more general investigations of whether and how particular microscopic features affect macroscopic properties of percolation. The effects of spatial correlations in the site occupation probability are relatively well understood [50, 52, 63–66], whereas the effects of variability and non-uniformity in the site occupation probability are still relatively open questions [67,68]. In cell biology, our study builds on previous work [18, 36, 39–43] that demonstrates the utility of percolation theory as a quantitative and predictive description of multicellular phenomena. It will be interesting to see in what biological systems ideas from percolation theory will provide useful insights next.

5.4   Materials and methods

5.4.1   Analysis of experiments

Computation of correlation function

To compute correlation functions, we first thresholded ThT images so that they were binary: biofilm regions above the ThT threshold would appear white and sub-threshold regions would appear black. We then applied a 2-pixel radius median filter to thresholded images so that clusters of on-cells became contiguous white regions. From this image, we created a 2D autocorrelation plot using the ImageJ command FD Math. The resulting plot was mean-subtracted and normalized such that the origin had a value of 1 and decayed to 0 away from the origin (see source code for the Radially Averaged Autocorrelation ImageJ plugin for further details).

To compute the radial autocorrelation curves (Fig 5.1C), we took a radial average of this 2D correlation plot. For x and y correlation curves, we took profiles of the correlation plot along the x and y axes, respectively.

To construct randomized images for such correlation computations, we took segmented biofilm images and randomly assigned a fraction of cells to be on and made them white. We then computed the autocorrelation curve on these images the same way as with the experimental images.

Lineage tracing for ρ_{div}

To determine ρ_{div}, we tracked individual cell lineages over time within biofilms using the mTrackJ imageJ plugin [69]. For each lineage, we recorded the firing state (i.e. on or off) of the parent cell and the daughter cells. Using many lineages, we computed the conditional probabilities $p(\mathrm{on}|\mathrm{on})$, $p(\mathrm{on}|\mathrm{off})$, $p(\mathrm{off}|\mathrm{on})$, and $p(\mathrm{off}|\mathrm{off})$. We then computed the order parameter ρ_{div} using Eq 5.2.

Spatial analysis for ρ_{adj}

To determine ρ_{adj}, we segmented cells in static images taken during signal pulses and determined the firing state of each cell (i.e. on or off). Because the electrical signal propagates in the direction of cell growth, cells are generally oriented along the signaling direction (Fig 5.1B). The adjacent cell in each case was defined as the cell whose bottom edge was closest to the given cell's top edge, and whose centroid was within half the average cell width. We then computed the conditional probabilities $p(\mathrm{on}|\mathrm{on})$, $p(\mathrm{on}|\mathrm{off})$, $p(\mathrm{off}|\mathrm{on})$, and $p(\mathrm{off}|\mathrm{off})$ for the firing state of a cell given the state of the adjacent cell. We then computed the order parameter ρ_{adj} using Eq 5.2.

Image analysis for $\Delta trkA$

We evaluated the cluster size distribution for $\Delta trkA$ biofilms in Fig 5.7B by first segmenting single biofilm cells in phase images using the Trainable Weka Segmentation plugin in ImageJ. We then thresholded the corresponding ThT images as described in the above section on computing correlation curves. Each contiguous white region in the thresholded image was a cluster of on-cells. We then counted how many segmented cells had the majority of their area within each cluster. The curve in Fig 5.7B plots the normalized histogram of these cluster sizes.

5.4.2 Theoretical methods

Mechanistic model

To derive Eqs 5.3 and 5.4, we require that the fraction of on-cells is ϕ at each step in the growth process. Specifically, the rules of probability state that

$$p(d) = \sum_m p(d, m) = \sum_m p(d|m)p(m), \tag{5.7}$$

where d is the signaling state (on, off) of the daughter, and m is the signaling state (on, off) of the mother. Taking $d =$ on and requiring that $p(\text{on}) = \phi$ and $p(\text{off}) = 1 - \phi$, Eq 5.7 becomes

$$\phi = p(\text{on}|\text{on})\phi + p(\text{on}|\text{off})(1 - \phi). \tag{5.8}$$

Solving for ϕ, we obtain

$$\phi = \frac{p(\text{on}|\text{off})}{1 + p(\text{on}|\text{off}) - p(\text{on}|\text{on})}. \tag{5.9}$$

Combining this equation with Eq 5.2 and solving for the conditional probabilities, we obtain Eqs 5.3 and 5.4.

Differential growth rates

We previously observed that signal participation reduces the cell elongation rate [36], implying that on-cells grow more slowly than off-cells. Specifically, Fig 1B of [36] shows that the elongation rate is reduced by a factor of about 4 at peak signaling activity. On-cells signal for about 20 minutes (Fig 4E of [36]), whereas pulses occur every 80 minutes or so (Fig S4 of [36]). Therefore the net growth rate ratio of on-cells to off-cells is approximately $\gamma = (1/4)(20/80) + (1)(60/80) \approx 80\%$.

To incorporate this feature into the model, we take the mean division time to be $\bar{\tau}$ and $\bar{\tau}/\gamma$ for off-cells and on-cells, respectively. Differential growth rates change the resulting fraction of on-cells in the lattice, and therefore Eqs 5.3 and 5.4 must be modified to maintain this fraction at ϕ. Specifically, using the shorthand $q \equiv p(\text{on}|\text{on})$ and $r \equiv p(\text{on}|\text{off})$ and recognizing that $p(\text{off}|\text{on}) = 1 - q$ and $p(\text{off}|\text{off}) = 1 - r$, the deterministic dynamics of the number of on- and off-cells are

$$\dot{n}_{\text{on}} = \gamma q n_{\text{on}} + r n_{\text{off}}, \tag{5.10}$$

$$\dot{n}_{\text{off}} = \gamma(1 - q)n_{\text{on}} + (1 - r)n_{\text{off}}, \tag{5.11}$$

where time is scaled by $\bar{\tau}$. At long times, the larger of the two eigenvalues of this linear dynamical system is

$$\lambda_+ = \frac{1}{2}\left[1 + \gamma q - r + \sqrt{(1 + \gamma q - r)^2 - 4\gamma(q - r)}\right], \tag{5.12}$$

and the ratio of the two components of the corresponding eigenvector gives the ratio of n_{on} and n_{off}. Setting the ratio of n_{on} and $n_{\text{on}} + n_{\text{off}}$ to ϕ obtains

$$\phi = \frac{r}{\lambda_+ + r - \gamma q}. \tag{5.13}$$

Note that taking $\gamma = 1$ makes $\lambda_+ = 1$, and Eq 5.13 recovers Eq 5.9. Combining Eqs 5.12 and 5.13 with $\rho = q - r$ (Eq 5.2) and solving for q and r obtains

$$p(\text{on}|\text{on}) = \phi + \frac{\rho(1 - \phi)}{1 - (1 - \gamma)\phi}, \tag{5.14}$$

$$p(\text{on}|\text{off}) = \phi - \frac{\gamma\phi\rho}{1 - (1 - \gamma)\phi}. \tag{5.15}$$

These expressions replace Eqs 5.3 and 5.4, respectively. This derivation ignores the differential crowding effects in the simulation due to the differential growth rates, but for $\phi = 0.43$, $\rho = 0.38$, and $\gamma = 0.8$ we still find that the resulting fraction of on-cells in the lattice is 0.428 ± 0.009, which includes 0.43 within error.

In this model with differential growth rates, we find that all of the predictions of Fig 3 remain unchanged: the correlation lengths in both the x and y directions are significantly larger than random ($p < 0.001$ for both), and $\rho_{\mathrm{adj}} = 0.19 \pm 0.02$, which actually now agrees with the measured 0.17 within error.

Renormalization argument

To derive Eqs 5.5 and 5.6, we recognize that the conditional probability of the daughter given the mother after one round of decimation is the conditional probability of daughter given the grandmother before the decimation. Again using the rules of probability, we write the latter as

$$p(d|g) = \sum_m p(d, m|g) = \sum_m p(d|m, g)p(m|g), \tag{5.16}$$

where g is the signaling state (on, off) of the grandmother. The spatial Markovian assumption states that d is conditionally independent of g given m. Therefore we have $p(d|m, g) = p(d|m)$, and Eq 5.16 becomes

$$p(d|g) = \sum_m p(d|m)p(m|g). \tag{5.17}$$

Setting $d = $ on and $g = $ on gives Eq 5.5. Setting $d = $ on and $g = $ off gives Eq 5.6.

To derive the relation $\rho_1 = \rho^2$ below Eq 5.6, we insert Eqs 5.5 and 5.6 into the definition $\rho_1 = p_1(\mathrm{on}|\mathrm{on}) - p_1(\mathrm{on}|\mathrm{off})$. Again using the shorthand $q \equiv p(\mathrm{on}|\mathrm{on})$ and $r \equiv p(\mathrm{on}|\mathrm{off})$ and recognizing that $p(\mathrm{off}|\mathrm{on}) = 1 - q$ and $p(\mathrm{off}|\mathrm{off}) = 1 - r$, this insertion obtains

$$\rho_1 = q^2 + r(1 - q) - qr - r(1 - r) = q^2 - 2qr + r^2 = (q - r)^2. \tag{5.18}$$

Because $\rho = q - r$ (Eq 5.2), we see that $\rho_1 = \rho^2$.

6. SPIRAL WAVE PROPAGATION IN COMMUNITIES WITH SPATIALLY CORRELATED HETEROGENEITY

Parts of this chapter have been submitted for publication as X. Zhai, J. W. Larkin, G. M. Süel, A. Mugler, "Spiral wave propagation in communities with spatially correlated heterogeneity."

Excitable wave propagation is ubiquitous in multicellular communities. However, the effects of cell-to-cell heterogeneity on excitable wave propagation are still poorly understood. In particular, in many multicellular communities such as bacterial biofilms the heterogeneity is spatially correlated along the signal direction. Here we use an excitable wave model to investigate wave propagation in communities with correlated heterogeneity. Surprisingly, we find that correlations can either promote or suppress the formation of spiral waves, depending on the excitation timescale. We explain this and related phenomena using a combination of minimal mathematical modeling, dynamic simulations, and percolation theory. Our work sheds light on how cell-level spatial statistics affect community-level signaling dynamics, and expands the understanding of wave propagation in heterogeneous media.

6.1 Heterogeneity and spiraling in biological systems

Collective behaviors are omnipresent in natural systems. They exist in diverse systems such as animal flocking, microbial colony formation and synchronization, traffic jamming, and social segregation in human populations [70–74]. Many of these systems span a hierarchy of scales and complexity, but the collective behavior at larger scales can often be understood without knowledge of many details at smaller scales [75–78]. This coarse-grained approach is often used to describe communities

where a directed signal travels from agent to agent to serve a function, which permits connections to reaction-diffusion systems of excitable media [79].

Directed signal propagation in multicellular communities is an important and commonly observed phenomenon. In the nervous system, a neuron passes an electrochemical signal to another neuron directly through a synapse. In a biofilm of *Bacillus subtilis* bacteria, the interior cells transmit an electrochemical wave to the periphery to mediate the metabolic activity [5, 13]. In pancreatic islets, gap junction coupling mediates electrical communication between cells [42]. The social amoebae *Dictyostelium discoideum* communicate via the signaling molecule cyclic adenosine monophosphate (cAMP) to coordinate aggregation [75].

Heterogeneity in these communities may pose a challenge to directed wave propagation. The stochastic expression of genes leads to non-uniform protein distributions across cells in a population. As a result, cells have heterogeneous responses to the wave propagation, and obstacles are naturally generated. For example, in the biofilm, a fraction of cells do not participate in the signal transmission, which can cause propagation failure [36, 80]. In cardiac cells, cell death can result in large patches of non-conductive tissue [81, 82], which are related to heart disease such as fibrosis and ischemia [81, 83]. Heterogeneities play an important role in deciding the wave pattern and result in a variety of wave behaviors, including wave death and spirals [82]. However, the impact of heterogeneity on wave propagation is still not fully understood.

The influence of heterogeneity on wave propagation has been investigated experimentally using cell monolayers [84] and patterned chemical systems [85–87], and theoretically using the FitzHugh-Nagumo model and cellular automata models [81]. When the length scales of the heterogeneities in the medium are close to the length scales associated with the propagating front, propagating waves can develop breaks, which can either block wave propagation or cause spiraling [81]. There are several mechanisms to explain the formation of spirals. For example the heterogeneity of the reaction field can stochastically generate unidirectional sites, which can induce spirals [82]. Spiral waves can also form as a result of an interaction between chemical

waves [88, 89]: when a chemical wave comes close to another wave from the back, part of the wave vanishes because of the refractory region of the preceding wave, and as a result spiral cores are formed.

Spiral waves can be either beneficial or detrimental to function. For example, spiral reentry of the action potential can induce heart failure [90, 91], whereas a spiral pattern formed on the nest of honeybees is an effective protection mechanism [92]. Therefore it is important to understand the formation of spiral waves in order to better understand community-level function in living systems.

Here we focus on excitable wave propagation in a two-dimensional heterogeneous community. We use a minimal FitzHugh-Nagumo-type model to describe the excitability of cells and introduce heterogeneity in the model parameters. Our model predicts three dynamic regimes (directed propagation, wave death, and spiraling), and we demonstrate how these regimes depend on the heterogeneity. We then introduce spatial correlations in the heterogeneity, which naturally arise due to lineage-based inheritance and cell-to-cell interactions [80]. Intuitively, one expects correlations to cause channeling and therefore promote directed propagation, and we indeed find this result in particular parameter regimes. However, we also find in other parameter regimes that correlations promote the emergence of spiral waves, a surprising feature that we explain by distinguishing between two different spiraling mechanisms. Finally, we characterize the dependence of the spiral period on the degree of heterogeneity in the system using percolation theory. Our results suggest that the spatial structure of cell-to-cell heterogeneity can have important consequences for signal propagation in cellular communities.

6.2   Materials and methods

We construct an integrated model combining the FitzHugh-Nagumo (FN) model [93, 94] and spatial heterogeneity. We use the FN model to describe the excitation of a single cell, which is coupled to its four neighbors in a square lattice. Heterogeneities

are introduced by randomly assigning each cell to be "on" or "off" which determines its parameter values (Fig. 6.1), as described below.

6.2.1 Excitable wave model

Hodgkin and Huxley proposed the first quantitative mathematical model to describe action potential propagation through very careful experimentation on the squid giant axon [95]. Modifying the Hodgkin and Huxley model for excitable media, FitzHugh and Nagumo established a partial differential equation model of two variables [93,94]. The FN model is a simplified variant of the Hodgkin and Huxley model, which traces the fast-slow dynamics of an excitable system [96].
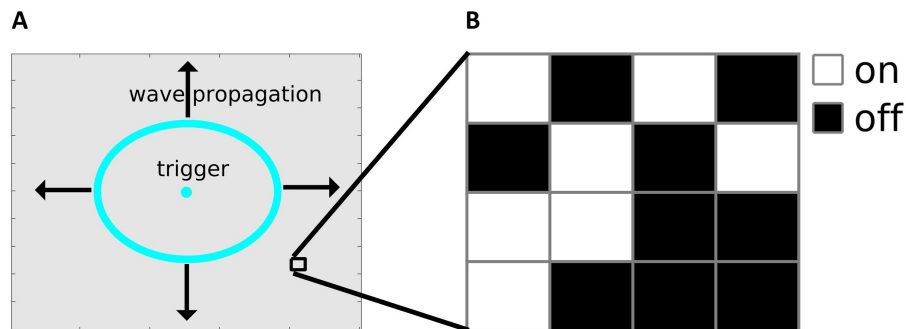
Fig. 6.1. Excitable wave propagation model in a two-dimensional heterogenous medium. *(A)* We evolve the dynamics on a 100×100 square lattice. A wave is triggered by the central 6 by 6 cells and propagates outward to the edges (cyan). *(B)* To introduce the heterogeneity, each cell is randomly assigned to be "on" (small τ) or "off" (large τ). Cyan indicates cells undergoing an excitation ($u \to 1$), whereas on and off refer to the propensity of a cell to fire, regardless of its current value of u.

We use a minimal FitzHugh-Nagumo-type model [97] to describe excitable wave propagation in a two-dimensional heterogeneous community. This minimal model is

$$\frac{du_i}{dt} = \epsilon[u_i^2(1 - u_i) - w_i] + \sum_{j \in \mathcal{N}(i)} (u_j - u_i), \tag{6.1}$$

$$\frac{dw_i}{dt} = \frac{1}{\tau}u_i, \tag{6.2}$$

where i indexes the cells, and $\mathcal{N}(i)$ denotes the four neighbors of cell i. The variables u and w are often called the excitation and recovery variables, respectively. The parameters in this reaction-diffusion system are the excitation strength ϵ, which when sufficiently high supports pulse-coupled wave propagation [98], and the recovery time τ, which sets the pulse duration of the signal and thus governs the dynamics. The second term in Eq. 6.1 is a discretized Laplacian term to account for the cell-cell communication. The minimalistic nature of this model promotes the interpretation of dynamics for single cells in excitable media.

In all dynamical simulations, cells in the center are initialized with $u = 1$ to trigger the excitable wave; all other cells are initialized with $w = 0$ (Fig. 6.1A). We use a square lattice of 100×100 cells with absorbing boundaries on four sides. To evolve the dynamics, we discretize the FN model in time using the fourth-order Runge-Kutta method with time step $\Delta t = 0.02$. We have checked that the simulation results are qualitatively the same with $\Delta t = 0.0001$, 0.001, and 0.01, but qualitatively change with a time step of $\Delta t = 0.1$, which justifies our choice of Δt on the order of 0.01.

6.2.2   Introduction of heterogeneity

We start with a homogeneous community (all cells have the same parameter values), and set the parameters in the following way to support directed propagation. The excitation strength ϵ must be larger than 1 because otherwise diffusion outpaces excitation and washes away the signal; therefore we set $\epsilon = 10$ [36]. This places the model in a diffusion-limited regime, which is consistent with signaling in the biofilms of *Bacillus subtilis* [13]. We find that the recovery time τ needs to be sufficiently large

($\tau > 7$) because otherwise the excitation is too short-lived to trigger its neighbors with $\epsilon = 10$.

To introduce heterogeneity, we must choose (i) the parameter to which heterogeneity will be introduced, and (ii) the distribution from which the parameter values will be drawn. For the parameter, we choose τ (we find that choosing ϵ has little effect and the wave always propagates). For the distribution, we use a binary distribution for heterogeneity in the parameter τ: each cell has probability ϕ to be on with $\tau_{\text{on}} > 7$, and probability $1 - \phi$ to be off with $\tau_{\text{off}} = 5$. Here we compare this distribution to two others, a log-uniform and a lognormal distribution (both ensure that τ stays positive), in terms of the resulting wave dynamics. To compare all distributions on equal footing, we plot the dynamic phases in the space of the distribution's mean and standard deviation. We see in Fig. 6.2 that the phase diagram of wave death (blue), radial propagation (green), and spirals (red) are qualitatively similar in all three cases. We conclude that the relationship between wave dynamics and heterogeneity is largely independent of the distribution from which the heterogeneity is drawn in our model. Therefore we focus only on binary heterogeneity in what follows.

6.2.3   Spatial correlations

We introduce radially directed spatial correlations using the following procedure. First, we randomly assign the cells in the central 6 by 6 grid to be on with probability ϕ, and off otherwise. Then, for each cell with unassigned neighbors (in random order), we choose a neighbor at random. With probability ρ we assign the neighbor to the same on/off state as the original cell. Otherwise, we assign the on/off state from the binary distribution. We repeat these steps until all cells are assigned. Therefore, ρ is the probability that a cell has the same on/off state as its radially inward neighbor, as opposed to being randomly assigned. In the limit of $\rho = 0$, the on-cells are randomly distributed in the excitable medium. Conversely, in the limit of $\rho = 1$, radii of perfectly correlated on or off-cells extend from the center to the periphery of the
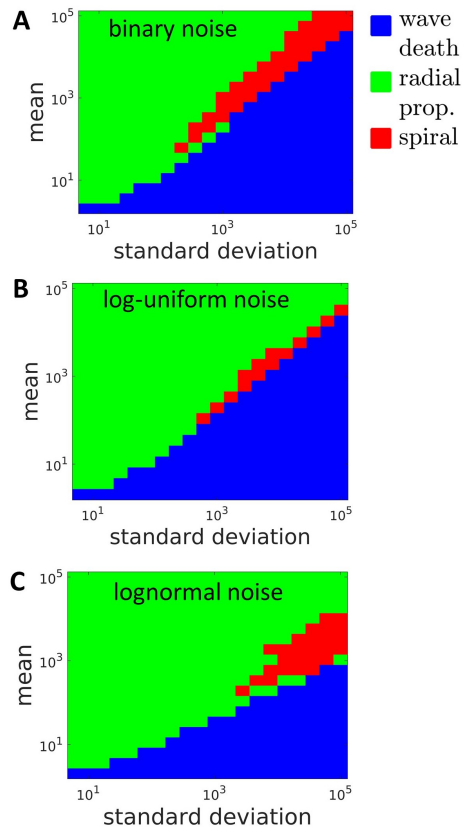
Fig. 6.2. Phase diagrams in the parameter space of mean and standard deviation with three different choices for the distribution of τ values: *(A)* binary, *(B)* log-uniform, and *(C)* lognormal. We see that the structure of the phase diagram is largely insensitive to the choice of distribution.
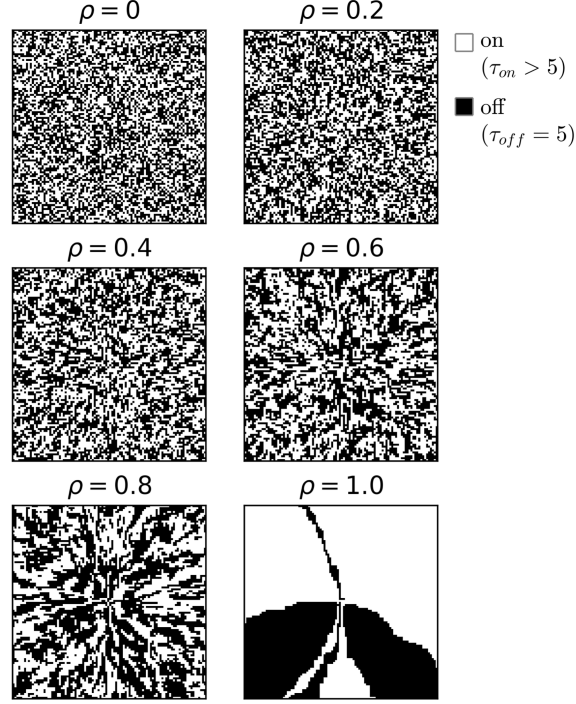
Fig. 6.3. Example lattices as in Fig. 6.5A, but for the full range of values $0 \leq \rho \leq 1$.

excitable medium. Thus, ρ serves as an order parameter for the system. Examples of lattices with ρ values from 0 to 1 are shown in Fig. 6.3.

6.3 Results

6.3.1 Heterogeneity produces three dynamic regimes

First we focus on uncorrelated heterogeneity ($\rho = 0$). As we vary the fraction of on-cells ϕ and their response timescale τ_{on}, we find three dynamic regimes, which we denote wave death, radial propagation, and spiral (Fig. 6.4). Wave death means that the wave dies ($u \to 0$) before reaching any edge (Fig. 6.4A). Radial propagation means that the wave propagates from the center to the edge (Fig. 6.4B). Spiral means that the wave forms a spiral pattern and can survive indefinitely (Fig. 6.4C). We

distinguish between radial propagation and spiral using the following criterion: if each cell undergoes at most one excitation we define the dynamics as radial propagation; otherwise we define the dynamics as spiral.

For $\rho = 0$ (Fig. 6.5A, left), the phase diagram of these dynamic regimes in the space of ϕ and τ_{on} is shown in Fig. 6.5B (left). We see that for sufficiently small ϕ, there are not enough on-cells to support the excitable wave; the wave cannot transmit
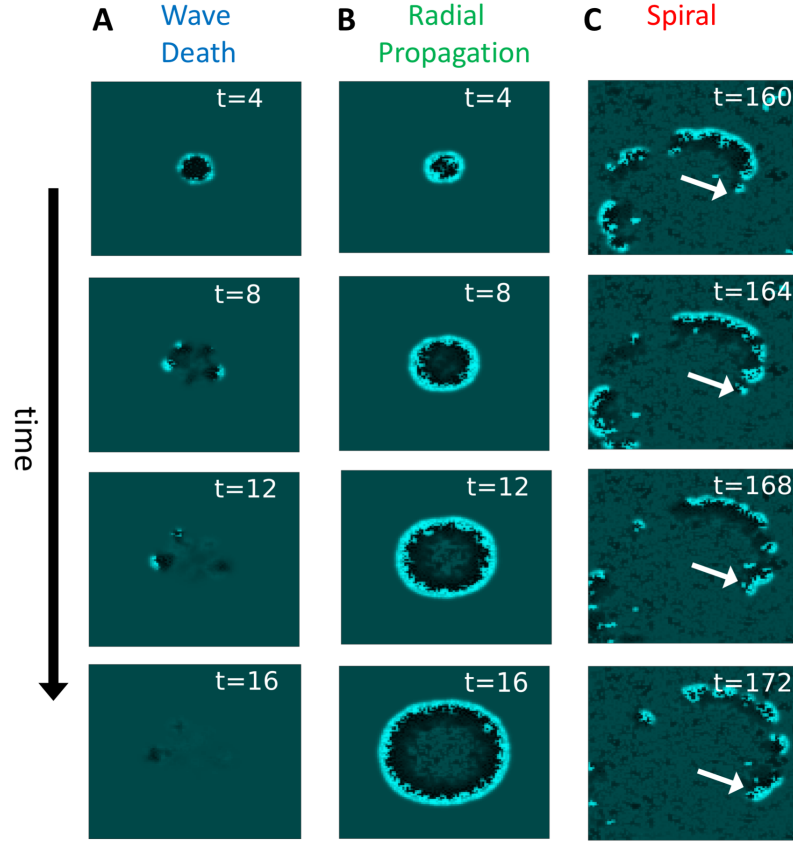
Fig. 6.4. Examples of the three dynamic regimes. No spatial correlations are present ($\rho = 0$). Brightness is proportional to signal strength u, showing wavefront (cyan, $u \to 1$) and refractory wave back (black, $u < 0$). *(A)* Wave death: signal dies before reaching any edge. *(B)* Radial propagation: wave propagates to edge and is absorbed at boundaries. *(C)* Spiral: wave spins back on itself and persists indefinitely; white arrow indicates spiral head. Here $\phi = 0.22$ and $\tau_{\mathrm{on}} = 281$ in A, $\phi = 0.49$ and $\tau_{\mathrm{on}} = 49$ in B, and $\phi = 0.49$ and $\tau_{\mathrm{on}} = 281$ in C.
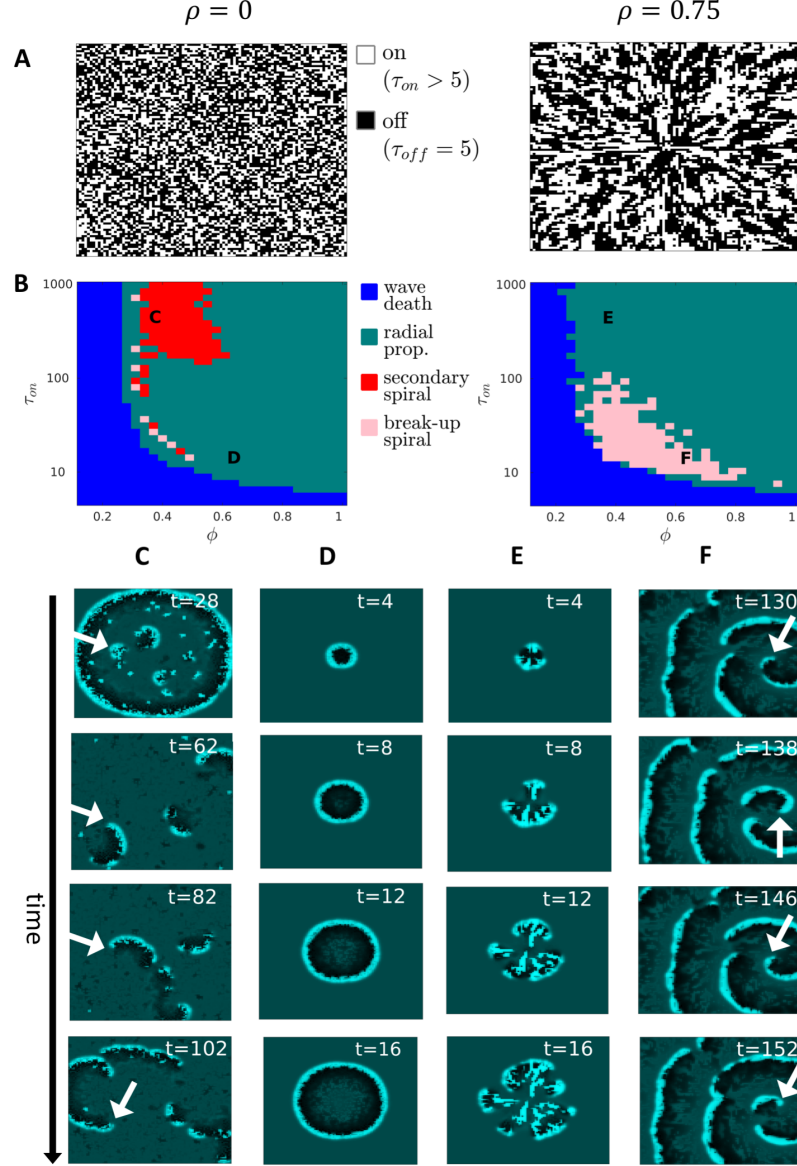
Fig. 6.5. Correlated heterogeneity can either suppress or promote spiral waves. *(A)* With no correlation ($\rho = 0$, left), on-cells are randomly distributed in the medium. Radial correlation ($\rho = 0.75$, right) produces channels of on-cells. Here $\phi = 0.46$. *(B)* Correlation suppresses spiraling at large τ_{on} (top red regime) but promotes spiraling at small τ_{on} (bottom light red regime). We refer to these subregimes as secondary spirals and breakup spirals, respectively. Phase diagrams in B contain 20 trials; spiral phase means that a spiral was observed in at least one trial, and otherwise we label with wave death or radial propagation, whichever is more frequent (see Fig. 6.6 for frequencies of all phases). Labels C-F in *B* correspond to the dynamics shown in panels *C-F*. White arrows in *C-F* indicate spiral head.
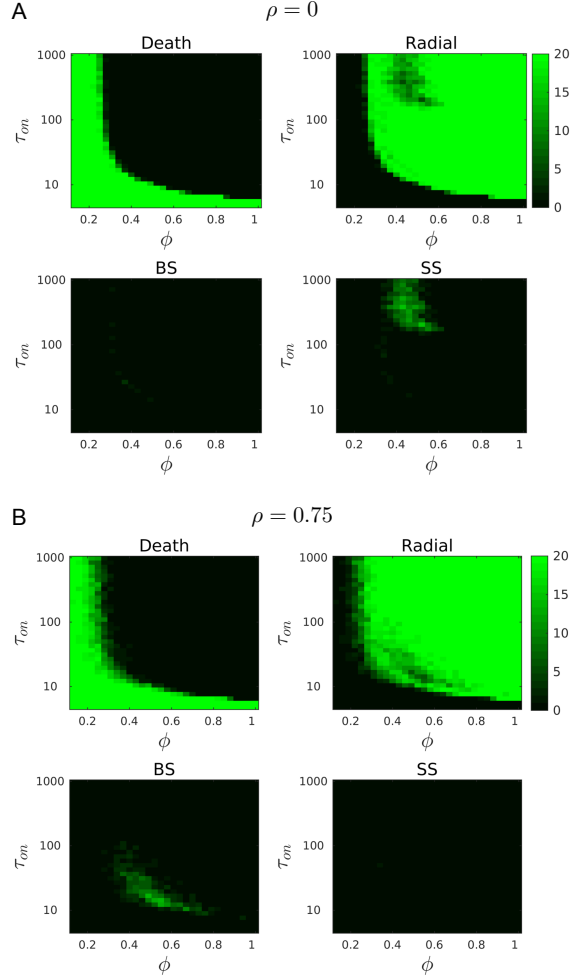
Fig. 6.6. Data used to plot phase diagrams in Fig. 6.5B. Color shows, at each point, the number of trials out of 20 that fall into each of the four dynamic regimes.

to the edge, resulting in wave death (blue). In contrast, for intermediate and large ϕ there are enough on-cells to support the wave, and we have mostly radial propagation (green). However, for a specific range of ϕ and when τ_{on} is sufficiently large, the wave becomes long-lived, and we see that this gives rise to spiraling (red; the difference between red and light red will be discussed below).

6.3.2   Spatial correlation can either suppress or promote spiraling

Next, we investigate the effects of spatially correlated heterogeneity ($\rho > 0$). Correlation can occur, for example, if excitation properties are inherited from cell to cell as the cells grow radially outward to form the community [80]. Radial correlation creates channels of on-cells, as seen in Fig. 6.5A (right) for $\rho = 0.75$ (see Fig. 6.3 for other values of ρ). Intuitively, we would expect that channeling should promote radial propagation and suppress spiraling. However, we find that it can either suppress or promote spiraling depending on the parameter regime. Specifically, as seen in Fig. 6.5B, the top portion of the red spiral regime in the phase diagram shrinks compared to the $\rho = 0$ case, as expected, whereas the bottom portion of the red spiral regime expands (Fig. 6.5B, right, light red). The latter is a surprising feature because one expects channeling to be beneficial to radial propagation and thus detrimental to spiraling.

Because of the different responses to correlated heterogeneity, we hypothesize that spirals in the top and bottom portions of the spiral regime are formed by different mechanisms. To investigate this hypothesis, we focus on specific examples within these regimes (see the labels C-F in Fig. 6.5B, which correspond to Fig. 6.5C-F). In the top regime, when the heterogeneity is uncorrelated, we see in Fig. 6.5C that some cells remain on after the wave has passed. These cells then trigger secondary excitations that become spirals. We therefore refer to these spirals as secondary spirals. When the heterogeneity is correlated, we see in Fig. 6.5E that these secondary spirals are suppressed by the channeling effect, and the wave propagates radially via the channels.

In the bottom regime, when the heterogeneity is uncorrelated, we see in Fig. 6.5D that the wave propagates radially. However, when the heterogeneity is correlated, we see in Fig. 6.5F that spirals form. The formation mechanism is different here than it is for the secondary spirals. Here, when the wavefront confronts a barrier of off-cells between channels, the wavefront breaks. Broken pieces of the wavefront then become

spirals. We therefore refer to these spirals as breakup spirals. Because the channeling is what causes the breakup, breakup spirals are enhanced by correlated heterogeneity, in contrast to secondary spirals.

To make this distinction quantitative, we define the following criterion. In the time before the first excitation of a boundary cell occurs, if the fraction of cells that undergo an excitation is more than (less than) the fraction of on-cells ϕ, then we define the spiral as secondary (breakup) and color that point red (light red). The reason for this definition is that secondary spirals generally form after the passage of a radial wavefront that initially excites most cells (Fig. 6.5C), whereas breakup spirals generally form from a broken wavefront that initially excites only some on-cells (Fig. 6.5F). Using this definition, we see a clear distinction between secondary spirals at $\rho = 0$ (left, red) and breakup spirals at $\rho = 0.75$ (right, light red). At intermediate ρ values, we see that as one type of spiral regime shrinks, the other one grows, as expected (see Fig. 6.7). These results demonstrate that the distinct spiral mechanisms we identify qualitatively are quantitatively supported by the data.

We can now understand why secondary spirals form at large τ_{on}, whereas breakup spirals form at small τ_{on} (Fig. 6.5B). τ_{on} sets the timescale for the excitation, including the refractory period. For a secondary spiral to form, large τ_{on} is necessary because this allows some of the on-cells—specifically, those that are surrounded by other on-cells—to remain excited long after the wave has passed. In contrast, for a breakup spiral to form, small τ_{on} is necessary because this means that the cells near the broken piece have already completed their refractory period. They are able to become excited again, which allows propagation of the breakup spiral.

6.3.3 Dependence of spiral period on anchor size

Our investigation of specific examples in Fig. 6.5C-F suggests that when spirals form, they circulate around clusters of off-cells in the medium, which we refer to as anchors. We will specifically test this hypothesis in the next section. Here, however,
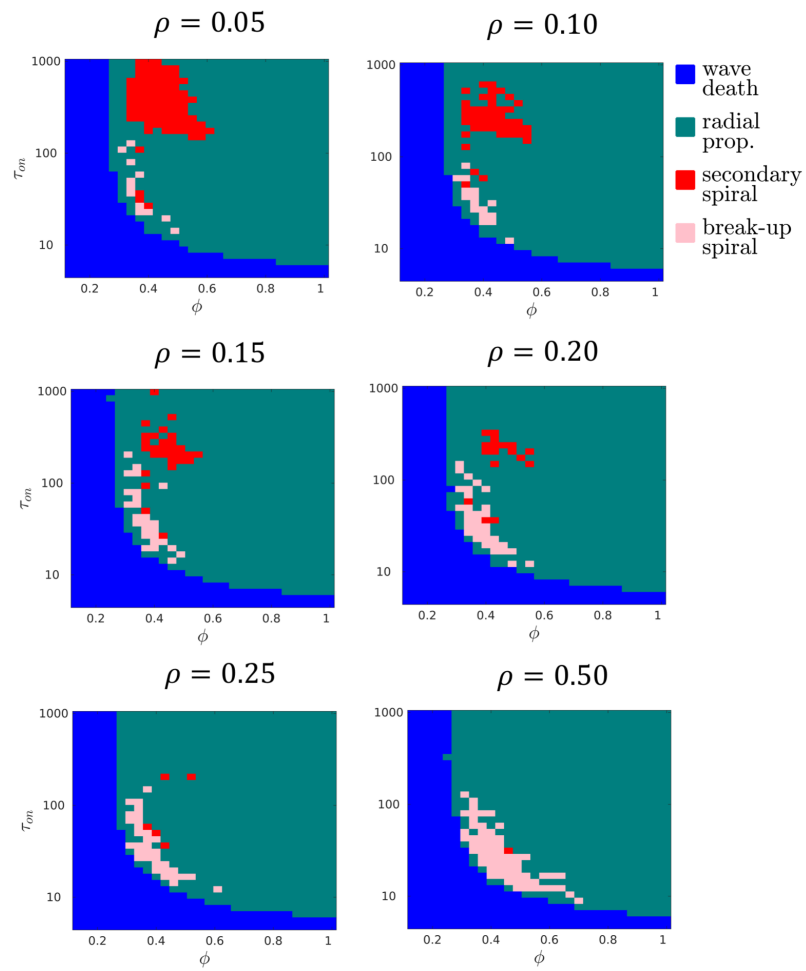
Fig. 6.7. Phase diagrams as in Fig. 6.5B, but for intermediate value of ρ.
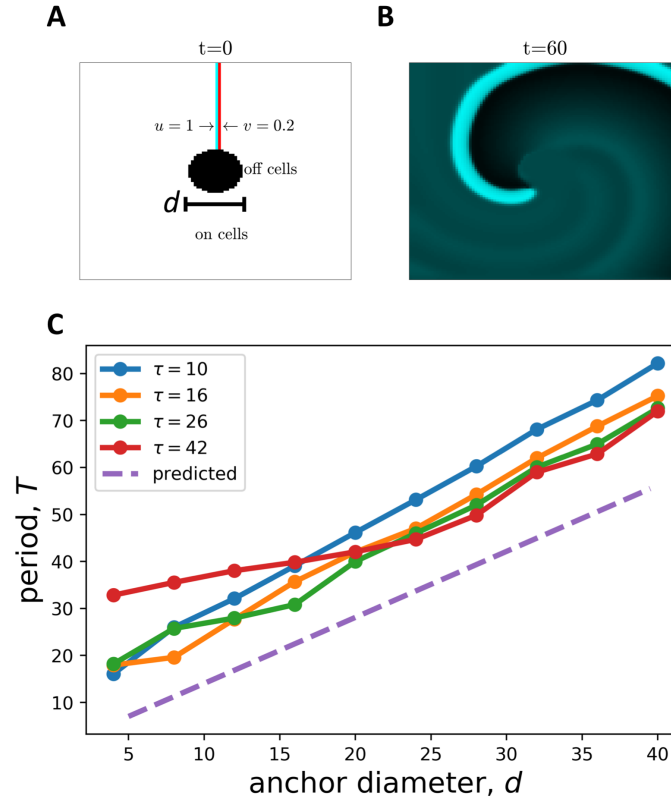
Fig. 6.8. Simplified example to investigate spiral period. *(A)* A circular off-cell anchor (black) with diameter d is surrounded by on-cells (white). Cells are initialized to trigger a counter-clockwise spiral, shown in *B*. *(C)* Period T as a function of d with various values of τ.

we first consider a simplified example to investigate the relationship between anchor size and spiral period. In Fig. 6.8A, a circular off-cell anchor with diameter d is surrounded by on-cells. The two central columns of cells above the anchor are initiated with $u = 1$ to trigger the wave, and $w = 0.2$ (a refractory state) to prevent wave propagation to the right, respectively. As a result, a spiral forms that travels around the anchor in a counter-clockwise direction (Fig. 6.8B).

In a homogeneous medium, the speed of a wave propagating according to Eqs. 6.1 and 6.2 is known [97] in the limit of $\tau \to \infty$ to be $v = \sqrt{\epsilon/2}$. Because the distance that the spiral travels around the anchor is πd, the period of rotation is $T = \pi d/v$, or

$$T = \frac{\pi d}{\sqrt{\epsilon/2}}. \tag{6.3}$$

Fig. 6.8C shows a test of this prediction in our simple example. We see that the measured period approaches the predicted period as τ increases, as expected. However, we see that the measured period remains larger than the predicted period, even for large τ. This is because the spiral head propagates at a slower speed than a radial wave would. Indeed, we have estimated in the secondary spiral regime of our heterogenous lattices (Fig. 6.5B left, $\phi = 0.49$, $\tau_{\mathrm{on}} = 281$) that spiral heads propagate about 15% slower than the initial radially propagating wavefront.

We also see in Fig. 6.8C a deviation from the prediction for small d when τ is large, which can be understood as follows. When the anchor size is small enough that the period is less than the recovery time τ, the wavefront is disrupted by the previous wave back. That is, the spiral head returns to its starting point before the cells at that point have completed their recovery. The progress of the spiral is delayed by the completion of the recovery, which increases the period. Quantitatively, this condition will occur when the predicted period in Eq. 6.3 is larger than τ, which sets a value of $d > \tau \sqrt{\epsilon/2}/\pi$ below which the prediction should fail. For example, with $\tau = 42$ and $\epsilon = 10$, we expect a deviation below $d \approx 30$, which is consistent with Fig. 6.8C (red curve).

6.3.4 Dependence of spiral period on heterogeneity

In the heterogeneous system, the anchors consist of the naturally occurring clusters of off-cells. The spatial statistics of these clusters are given by percolation theory [99], which describes the probabilistic and connectivity properties of regular lattices in which each site is either on or off. Therefore, the goal of this section is to use percolation theory to investigate how the heterogeneity parameters ϕ and ρ affect the

spatial structure of the community and in turn, the spiral dynamics. Percolation theory has been recently used to describe wave propagation in various multicellular systems, including electrical signaling in bacterial biofilms [36, 80] and neuronal populations [18, 39–41], quorum sensing in bacterial communities [38]. calcium wave propagation in pancreatic islets [42], and hydrodynamic waves in aquatic cells [100].

Intuitively we expect that at any ρ, the spiral period is a monotonically decreasing function of ϕ because the off-cell clusters shrink with ϕ. To make this expectation quantitative, we turn to percolation theory. Two-dimensional percolation theory on a square lattice applies when $\rho = 0$ and predicts a critical threshold $\phi_c \approx 0.59$, above which there exists a giant on-cell cluster spanning the medium. We expect this regime to be dominated by radial propagation. Conversely, below a complementary threshold of $\phi = 1 - \phi_c \equiv p_c \approx 0.41$, there exists a giant off-cell cluster. We expect this regime to be dominated by wave death. Indeed, we see in Fig. 6.5B (left) that, roughly speaking, radial propagation occurs for $\phi > \phi_c$, wave death occurs for $\phi < p_c$, and spirals occur within $p_c < \phi < \phi_c$. These regimes are rough because percolation theory accounts for the static structure of the lattice but not the excitable dynamics.

Near either percolation threshold, percolation theory provides scaling relations for the cluster properties. Therefore, we use percolation theory to understand how the anchor size scales with ϕ. Specifically, above p_c, the mean off-cell cluster size scales as [99]

$$n_{\text{off}} \sim (\phi - p_c)^{-\gamma} \tag{6.4}$$

where $\gamma = 43/18 \approx 2.39$. We confirm this scaling with progressively larger lattice sizes in the inset of Fig. 6.9A. We see that the mean anchor size is indeed a decreasing function of ϕ.

The period should depend on the circumference of the off-cell cluster being circulated. To the extent that the fractal dimension [99] of the off-cell cluster is near
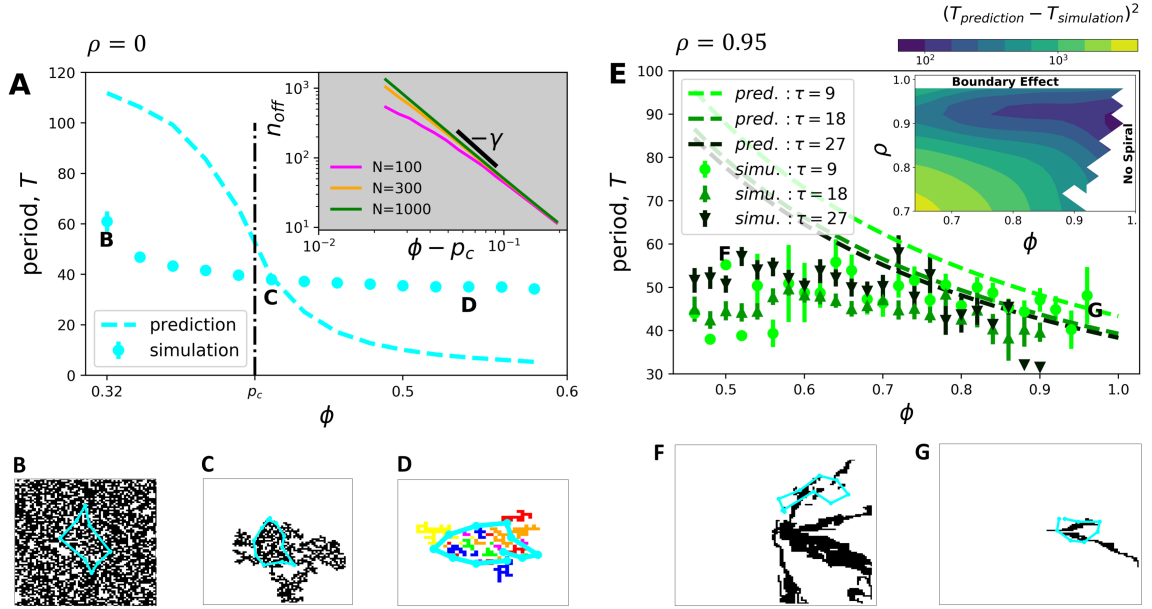
Fig. 6.9. Dependence of spiral period on heterogeneity parameters with predictions from percolation theory. *(A-D)* Uncorrelated heterogeneity ($\rho = 0$). A shows period T vs. fraction of on-cells ϕ predicted by two-dimensional percolation theory and computed from simulations. Prediction fails as described in text and illustrated in B-D. Inset confirms scaling prediction of percolation theory for various $N \times N$ system sizes. B-D show examples (labeled in A) of spiral dynamics (cyan, trace of spiral head; see Fig. 6.10 for full spiral in C) and anchoring cluster(s) of off-cells (in D there are many clusters, distinguished by color). *(E-G)* Strongly correlated heterogeneity ($\rho = 0.95$). E is as in A but with one-dimensional percolation theory to describe quasi-one-dimensional clusters. Prediction succeeds at large ϕ. Inset: Squared deviation between prediction and simulation as a function of ϕ and ρ. Data smoothed using two-dimensional Gaussian filter with standard deviation 0.04. F and G are as in B-D. In A-D, $\tau_{\mathrm{on}} = 240$; in E (inset), F, and G, $\tau_{\mathrm{on}} = 9$. In A and E, period is calculated as average time between excitations ($u > 0.6$) from cases out of 1000 trials where spiraling occurred; error bars are standard error.
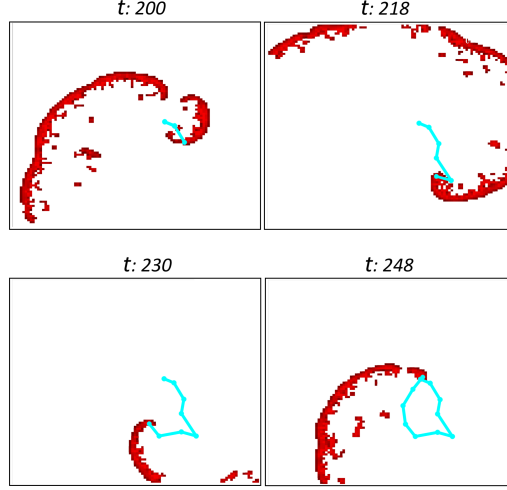
Fig. 6.10. Cumulative path of spiral head (cyan) and instantaneous excited cells that make up spiral (red) at various times, corresponding to Fig. 6.9C. For clarity, we color excited cells red to distinguish them from cyan path, and we do not show other cells.

two (at $\phi = p_c$ it is $91/48 \approx 1.90$), the mean circumference should be roughly $\pi\sqrt{n_{\text{off}}}$. Therefore, following Eq. 6.3, we predict that the spiral period should be

$$T = \frac{\pi\sqrt{n_{\text{off}}}}{\sqrt{\epsilon/2}}. \tag{6.5}$$

This prediction is shown in Fig. 6.9A (cyan dashed line), where n_{off} is computed numerically. Above $\phi = p_c$ we see the power-law decay from percolation theory, while below $\phi = p_c$ the divergence of n_{off} and thus T is prevented by the finite size of the lattice. We then compare this prediction to the dynamic simulation results by plotting the average spiral period (cyan data points in Fig. 6.9A). We see for both the prediction and the simulation results that T decreases with ϕ as expected, but that otherwise the agreement is poor.

To understand the deviation between the prediction and the simulations, we investigate the dynamics of individual spirals at various values of ϕ. We plot the path of the spiral head over a full period (Fig. 6.9B-D; see Fig. 6.10 for an example of the full spiral). When $\phi < p_c$ (Fig. 6.9B), the giant off-cell cluster spans the whole system.

In contrast, the spiral typically circulates only a small part of the cluster. Therefore the observed period is less than predicted, as seen in Fig. 6.9A. When $\phi \approx p_c$ (Fig. 6.9C), the spiral typically circulates the bulk of a single off-cell cluster. The spiral avoids the fractal "arms" of the cluster, but the cluster is also not maximally dense. These two effects compensate, such that the predicted and observed periods generally agree. When $\phi > p_c$ (Fig. 6.9D), the mean off-cell cluster size is small, but the spiral typically circulates multiple nearby clusters. Therefore the observed period is greater than predicted, as seen in Fig. 6.9A.

Thus, we conclude that with uncorrelated heterogeneity ($\rho = 0$), percolation theory confirms that the spiral period decreases with the on-cell fraction, but it does not provide quantitative predictions due to the fact that it cannot capture the details of the propagation dynamics. What about highly correlated heterogeneity, when ρ is large?

Standard percolation theory assumes $\rho = 0$ and therefore does not apply for general ρ. However, when ρ is very large ($\rho \to 1$), the off-cell clusters become highly distended in the radial direction due to the correlation. Therefore, they become quasi-one-dimensional, and we may expect that tools from one-dimensional percolation theory [99] could provide a predictive understanding. Indeed, if we consider any radius of the system as a one-dimensional lattice, we can calculate, for a randomly chosen off-cell in that lattice, the mean length of the chain of off-cells of which it is a member.

Considering any radius of the system as a one-dimensional lattice of L cells. Denote the center and edge of the radius as the left and right end of the lattice, respectively. Calling any cell in this lattice a "mother" cell m, and its rightward neighbor

a "daughter" cell d, the conditional probabilities $P(d|m)$ of the state of the daughter given the state of the mother are

$$P(d = \text{on}|m = \text{on}) = \rho + (1 - \rho)\phi, \tag{6.6}$$

$$P(d = \text{off}|m = \text{off}) = \rho + (1 - \rho)(1 - \phi), \tag{6.7}$$

$$P(d = \text{on}|m = \text{off}) = (1 - \rho)\phi, \tag{6.8}$$

$$P(d = \text{off}|m = \text{on}) = (1 - \rho)(1 - \phi). \tag{6.9}$$

In Eqs. 6.6 and 6.7, the daughter is guaranteed to be in the same state as the mother with probability ρ (first term), and with probability $1 - \rho$ it could also be in the same state by chance, either on with probability ϕ or off with probability $1 - \phi$, respectively (second term). In Eqs. 6.8 and 6.9, the daughter is in the opposite state as the mother, which requires both anti-correlation with probability $(1 - \rho)$ and selection of the opposite state by chance with probability ϕ or $1 - \phi$, respectively.

Given these conditional probabilities, we calculate the probability q_s that a randomly chosen cell is at the left end of a chain of off-cells of size s. It must be off with probability $1 - \phi$, its mother must be on with probability $P(m = \text{on}|d = \text{off})$, the next $s - 1$ rightward cells must be off with probability $P(d = \text{off}|m = \text{off})$, and the next cell after that must be on with probability $P(d = \text{on}|m = \text{off})$, giving

$$\begin{aligned} q_s &= (1 - \phi)P(m = \text{on}|d = \text{off}) \\ &\quad \times P(d = \text{off}|m = \text{off})^{s-1} \\ &\quad \times P(d = \text{on}|m = \text{off}) \tag{6.10} \\ &= \phi^2(1 - \phi)(1 - \rho)^2[\rho + (1 - \rho)(1 - \phi)]^{s-1}. \tag{6.11} \end{aligned}$$

The second step follows from Eqs. 6.7 and 6.8 and Bayes' theorem,

$$\begin{aligned} P(m = \text{on}|d = \text{off}) &= \frac{P(m = \text{on})P(d = \text{off}|m = \text{on})}{P(d = \text{off})} \\ &= \frac{\phi(1 - \rho)(1 - \phi)}{1 - \phi} = \phi(1 - \rho), \tag{6.12} \end{aligned}$$

where we have used Eq. 6.9.

The probability q_s is equivalent to the number N_s of chains of size s, divided by the lattice size L. Similarly, the probability that a randomly chosen cell is a member of a chain of size s (not just the left end) is $N_s s/L$. Finally, the probability P_s that a randomly chosen cell is a member of a chain of size s, given that it is an off-cell, is $N_s s/L$ divided by the probability of being an off-cell, $1 - \phi$. Therefore, we have

$$P_s = \frac{q_s s}{1 - \phi}.$$ (6.13)

Thus, the mean length of a chain containing a randomly chosen off-cell is

$$n_{\text{off}}^{\text{1D}} = \sum_{s=1}^{\infty} P_s s = \frac{1}{1 - \phi} \sum_{s=1}^{\infty} q_s s^2 = \frac{2}{(1 - \rho)} \frac{1}{\phi} - 1,$$ (6.14)

as in Eq. 6.14, where we have used Eq. 6.11 and the properties of a geometric series. Note that the mean chain size decreases with ϕ and increases with ρ until diverging for $\rho \to 1$, as expected.

The circumference of the chain (ignoring the ends) is twice this length, such that the predicted spiral period is

$$T = \frac{2}{v(\tau_{\text{on}})} \left[\frac{2}{(1 - \rho)} \frac{1}{\phi} - 1 \right].$$ (6.15)

For $v(\tau_{\text{on}})$ we use the radial wave speed measured in a uniform lattice of on-cells with $\tau = \tau_{\text{on}}$ instead of the large-τ approximation $\sqrt{\epsilon/2}$ because τ_{on} is constrained to be small as discussed below.

When ϕ is small, there are many off-cells in the system. Chains of off-cells from neighboring radii will fall next to each other, the quasi-one-dimensional nature of the clusters will be lost, and we expect this analysis to fail. On the other hand, when ϕ is large, chains of off-cells will be rare, and we expect this analysis to be valid. Therefore, we expect Eq. 6.15 to hold at large $\rho \to 1$ and large $\phi \to 1$.

The prediction in Eq. 6.15 is compared with simulations in Fig. 6.9E for $\rho = 0.95$ (main panel). As expected, we see that the prediction fails at small ϕ but succeeds at large ϕ. Indeed, as seen in Fig. 6.9F, at small ϕ, chains of off-cells from neighboring radii fall next to each other, and the clusters are no longer quasi-one-dimensional. In

contrast, as seen in Fig. 6.9G, at large ϕ, the clusters quasi-one-dimensional and well separated, and the spiral generally circulates one of the clusters.

To check that the agreement between the prediction and simulations holds beyond the particular choice of parameters in Fig. 6.9E (main panel), we perform a more comprehensive exploration of the parameter space, defined by ϵ, τ_{on}, ρ, and ϕ. We find that spiral formation is highly sensitive to the value of ϵ. This makes intuitive sense because if ϵ is too small then diffusion outpaces excitation and the wave cannot propagate; whereas if ϵ is too large then propagation is too fast and only radial waves form. These constraints confine us to the regime of our current value $\epsilon = 10$.

With regard to τ_{on}, the relevant range is constrained by two effects. On the one hand, propagation requires $\tau_{\mathrm{on}} > 7$, which is the criterion for on- vs. off-cells. On the other hand, Fig. 6.5B (right) illustrates that small τ_{on} is necessary in order to have spiral formation out to large ϕ, where Eq. 6.15 is valid. These constraints overlap in the regime $\tau_{\mathrm{on}} \sim 10$. Therefore, Fig. 6.9E shows results for $\tau_{\mathrm{on}} = 9$, 18, and 27 (main panel). We see that both the prediction curves and the simulation data each converge to a fixed trend as τ_{on} increases, as expected, and that the data agree with their respective prediction as ϕ increases, as expected.

This leaves ϕ and ρ. We plot the deviation between Eq. 6.15 and the simulations as a function of ϕ and ρ for $\tau_{\mathrm{on}} = 9$ in the inset of Fig. 6.9E. We see that the deviation is smallest (dark blue) for large ϕ and ρ as expected, but we also see that this trend breaks down if either ϕ or ρ become too large. The reason that the trend breaks down at very large ϕ is simply, as mentioned above, that spirals do not form if ϕ is too large. The reason that the trend breaks down at very large ρ is that the mean length of the quasi-one-dimensional off-cell anchors exceeds the boundary of the system. Specifically, from Eq. 6.14, this length is approximately $2/(1 - \rho)$ for large ϕ, which exceeds the system half-width of 50 cells when ρ exceeds about 0.96. Indeed, we see in the inset of Fig. 5E that the agreement begins to diverge beyond $\rho \approx 0.96$.

Thus, apart from these limitations at the extremes of ϕ and ρ, we find that the predictions of percolation theory agree with the simulations in the regimes were we expect them to be valid. These more comprehensive checks validate our theory.

6.4 Discussion

We have developed a model that describes wave propagation in a spatially correlated heterogeneous medium. Despite the minimal nature of the model, and the idealization of cells as squares on a regular lattice, our model supports multiple dynamic regimes including wave death, radial propagation, and spiraling. We have discovered that spirals arise via two distinct mechanisms—secondary triggers and wavefront breakup—and that spatial correlations in the heterogeneity suppress the former and promote the latter, in two distinct regimes within parameter space. Furthermore, we have shown using percolation theory that the structural properties of the heterogeneity influence the dynamic properties of spiraling (the period), and that the predictive power of percolation theory is best when the spatial correlation is strong. Taken together, our results suggest that the spatial structure of cell-to-cell heterogeneity can have important consequences for directed signal propagation in cellular communities.

The minimal nature of the model facilitates its application as a phenomenological description of experiments on signaling in cellular communities. Because there are only two parameters describing the dynamics (the time scale and the excitation strength), and two parameters describing the heterogeneity (the fraction and spatial correlation of on-cells), these parameters could be easily calibrated to experimental observations. Because the parameters and variables are dimensionless, the cell length scale and signal time scale would set the units of length and time, and then other observables such as the wavelength and fraction of signaling cells could calibrate other parameters to the point where predictions could be made and tested with no further free parameters [36].

Spatially correlated heterogeneity is a common feature in many multicellular systems. Electrical signaling in *Bacillus subtilis* biofilms is spatially correlated along the signaling direction [80], potentially due to the maintenance and inheritance of a phenotypic state over several cell generations [55–57]. Similarly, the lengthscale of cell-to-cell signaling in quorum sensing bacterial communities has been shown to depend on the establishment of spatial correlations [38,58]. In eukaryotes, spatial correlations in cell-substrate interactions can drive collective cell migration [60], which is a fundamental multicellular process in tissue development [61] and wound healing [62]. Thus, our findings on how spatial correlations influence excitable signal propagation could find broad application across multicellular biology.

Our work could also provide insights on how one might engineer heterogeneous media to produce spiral waves. First, the excitability threshold must be low; in this work we set it to zero (in the typical FN there is an additional threshold parameter in Eq. 6.1). Second, an intermediate degree of heterogeneity is required, with not too many or too few excitable cells (Fig. 6.5B), which could be controlled by genetic engineering [36] or different fractions of a multi-species cell mixture. Third, either a large or a small excitation timescale is required depending on the degree of spatial correlation (Fig. 6.5B). The excitation timescale could be changed by mutation [36], and the spatial correlation could be controlled by modulating the degree of cell redistribution in a microfludic device or by using strains with differential growth rates.

Our model has limitations, and several extensions are natural. Although we check that our results are insensitive to the heterogeneity distribution (Fig. 6.2), we only add heterogeneity to one parameter (the timescale). It may be more realistic to add heterogeneity to all parameters [101], including the excitation strength and, if included, the excitation threshold. Moreover, we assume that cells exist on a regular square lattice and that heterogeneity is only correlated in the radial direction. It may be more realistic to add disorder to either the lattice structure, cell size [36], or spatial direction of the heterogeneity [80]. Finally, we assume that noise only enters spatially in the assignment of cell on/off states, not dynamically in the excitable system of Eqs.

6.1 and 6.2. Noise could cause untriggered excitations even for off-cells (especially because we set the threshold to zero), and it may be more realistic to include noise terms in the dynamics. Such noise has been shown to alter the boundaries between dynamic regimes in excitable systems, including in *Bacillus subtilis* [102]. It will be interesting to see how our model can be generalized, as well as how it can be used to understand or engineer experimental systems in future work.

7. SUMMARY

Signal transmission among cells enables long-range coordination in biological systems. However, the scarcity of quantitative measurements hinders the development of theories that relate signal propagation to cellular heterogeneity and spatial organization. We address this problem in a bacterial community that employs electrochemical cell-to-cell communication. We developed a model based on percolation theory, which describes how signals propagate through a heterogeneous medium. Our model predicts that signal transmission becomes possible when the community is organized near a critical phase transition between a disconnected and a fully connected conduit of signaling cells. By measuring population-level signal transmission with single-cell resolution in wild-type and genetically modified communities, we confirm that the spatial distribution of signaling cells is organized at the predicted phase transition. Our findings suggest that at this critical point, the population-level benefit of signal transmission outweighs the single-cell level cost. The bacterial community thus appears to be organized according to a theoretically predicted spatial heterogeneity that promotes efficient signal transmission.

However, we find experimentally that key features of this system go beyond the simple assumptions of basic percolation theory, which include site-to-site independence and spatial uniformity of the signaling probability. Why are the predictions of percolation theory still upheld? Using a computational model, we find that the cell-to-cell dependence does not change the predictions due to the universal nature of percolation theory near its critical point, and the spatial variability of the signaling probability actually expands the parameter range over which the predictions hold. We validate our findings using a mutant bacterial strain. Our work explores the robustness of percolation theory to its underlying assumptions, and the resulting consequences for long-range bacterial signaling.

Finally, motivated by experimental systems that exhibit spiral waves, we use our minimal FitzHugh-Nagumo-type model to investigate excitable wave propagation in a two-dimensional heterogeneous community more generally. The model shows three dynamic regimes in which waves either propagate directionally, die out, or spiral indefinitely, and we characterize how these regimes depend on the heterogeneity parameters. We find that in some parameter regimes, spatial correlations in the heterogeneity enhance directional propagation and suppress spiraling. However, in other regimes, spatial correlations promote spiraling, a surprising feature that we explain by demonstrating that these spirals form by a second, distinct mechanism. We characterize the dependence of the spiral period on the degree of heterogeneity in the system by using techniques from percolation theory. Overall, our results reveal that the spatial structure of cell-to-cell heterogeneity can have important consequences for signal propagation in cellular communities.

REFERENCES

REFERENCES

[1] D. Debanne, E. Campanac, A. Bialowas, E. Carlier, and G. Alcaraz, "Axon physiology," *Physiological reviews*, vol. 91, no. 2, pp. 555–602, 2011.

[2] M. Notaguchi and S. Okamoto, "Dynamics of long-distance signaling via plant vascular tissues," *Frontiers in Plant Science*, vol. 6, p. 161, 2015.

[3] Y. Cao, M. D. Ryser, S. Payne, B. Li, C. V. Rao, and L. You, "Collective space-sensing coordinates pattern scaling in engineered bacteria," *Cell*, vol. 165, no. 3, pp. 620–630, 2016.

[4] J. L. Connell, J. Kim, J. B. Shear, A. J. Bard, and M. Whiteley, "Real-time monitoring of quorum sensing in 3d-printed bacterial aggregates using scanning electrochemical microscopy," *Proceedings of the National Academy of Sciences*, vol. 111, no. 51, pp. 18 255–18 260, 2014.

[5] J. Liu, A. Prindle, J. Humphries, M. Gabalda-Sagarra, M. Asally, D. L. Dong-yeon, S. Ly, J. Garcia-Ojalvo, and G. M. Süel, "Metabolic co-dependence gives rise to collective oscillations within biofilms," *Nature*, vol. 523, no. 7562, p. 550, 2015.

[6] C. M. Waters and B. L. Bassler, "Quorum sensing: cell-to-cell communication in bacteria," *Annu. Rev. Cell Dev. Biol.*, vol. 21, pp. 319–346, 2005.

[7] B. Li and L. You, "Predictive power of cell-to-cell variability," *Quantitative Biology*, vol. 1, no. 2, pp. 131–139, 2013.

[8] A. Raj and A. van Oudenaarden, "Nature, nurture, or chance: stochastic gene expression and its consequences," *Cell*, vol. 135, no. 2, pp. 216–226, 2008.

[9] O. Symmons and A. Raj, "Whats luck got to do with it: single cells, multiple fates, and biological nondeterminism," *Molecular cell*, vol. 62, no. 5, pp. 788–802, 2016.

[10] J.-M. Cao, Z. Qu, Y.-H. Kim, T.-J. Wu, A. Garfinkel, J. N. Weiss, H. S. Karagueuzian, and P.-S. Chen, "Spatiotemporal heterogeneity in the induction of ventricular fibrillation by rapid pacing: importance of cardiac restitution properties," *Circulation research*, vol. 84, no. 11, pp. 1318–1331, 1999.

[11] B. E. Steinberg, L. Glass, A. Shrier, and G. Bub, "The role of heterogeneities and intercellular coupling in wave propagation in cardiac tissue," *Philosophical Transactions of the Royal Society A: Mathematical, Physical and Engineering Sciences*, vol. 364, no. 1842, pp. 1299–1311, 2006.

[12] S. G. Waxman, "Axonal conduction and injury in multiple sclerosis: the role of sodium channels," *Nature Reviews Neuroscience*, vol. 7, no. 12, p. 932, 2006.

[13] A. Prindle, J. Liu, M. Asally, S. Ly, J. Garcia-Ojalvo, and G. M. Süel, "Ion channels enable electrical communication in bacterial communities," *Nature*, vol. 527, no. 7576, p. 59, 2015.

[14] M. Bär, A. Bangia, I. Kevrekidis, G. Haas, H.-H. Rotermund, and G. Ertl, "Composite catalyst surfaces: Effect of inert and active heterogeneities on pattern formation," *The Journal of Physical Chemistry*, vol. 100, no. 49, pp. 19 106–19 117, 1996.

[15] I. Sendiña-Nadal, A. Muñuzuri, D. Vives, V. Pérez-Muñuzuri, J. Casademunt, L. Ramírez-Piscina, J. M. Sancho, and F. Sagués, "Wave propagation in a medium with disordered excitability," *Physical review letters*, vol. 80, no. 24, p. 5437, 1998.

[16] O. Steinbock, P. Kettunen, and K. Showalter, "Anisotropy and spiral organizing centers in patterned excitable media," *Science*, vol. 269, no. 5232, pp. 1857–1860, 1995.

[17] P. Bak, K. Chen, and C. Tang, "A forest-fire model and some thoughts on turbulence," *Physics letters A*, vol. 147, no. 5-6, pp. 297–300, 1990.

[18] D. W. Zhou, D. D. Mowrey, P. Tang, and Y. Xu, "Percolation model of sensory transmission and loss of consciousness under general anesthesia," *Physical review letters*, vol. 115, no. 10, p. 108103, 2015.

[19] H. C. Tuckwell, *Introduction to theoretical neurobiology: volume 2, nonlinear and stochastic theories.* Cambridge University Press, 1988, vol. 8.

[20] L. Dai, K. S. Korolev, and J. Gore, "Slower recovery in space before collapse of connected populations," *Nature*, vol. 496, no. 7445, p. 355, 2013.

[21] J. Katz, "A model of propagating brittle failure in heterogeneous media," *Journal of Geophysical Research: Solid Earth*, vol. 91, no. B10, pp. 10 412–10 420, 1986.

[22] G. Bub, A. Shrier, and L. Glass, "Spiral wave generation in heterogeneous excitable media," *Physical review letters*, vol. 88, no. 5, p. 058101, 2002.

[23] D. Stauffer and A. Aharony, *Introduction to percolation theory.* Taylor & Francis, 2018.

[24] A. Aharony, "Universal critical amplitude ratios for percolation," *Physical Review B*, vol. 22, no. 1, p. 400, 1980.

[25] A. Seminara, T. E. Angelini, J. N. Wilking, H. Vlamakis, S. Ebrahim, R. Kolter, D. A. Weitz, and M. P. Brenner, "Osmotic spreading of bacillus subtilis biofilms driven by an extracellular matrix," *Proceedings of the National Academy of Sciences*, vol. 109, no. 4, pp. 1116–1121, 2012.

[26] J. Humphries, L. Xiong, J. Liu, A. Prindle, F. Yuan, H. A. Arjes, L. Tsimring, and G. M. Süel, "Species-independent attraction to biofilms through electrical signaling," *Cell*, vol. 168, no. 1-2, pp. 200–209, 2017.

[27] J. Liu, R. Martinez-Corral, A. Prindle, D. L. Dong-yeon, J. Larkin, M. Gabalda-Sagarra, J. Garcia-Ojalvo, and G. M. Süel, "Coupling between distant biofilms and emergence of nutrient time-sharing," *Science*, vol. 356, no. 6338, pp. 638–642, 2017.

[28] M. E. Lundberg, E. C. Becker, and S. Choe, "Mstx and a putative potassium channel facilitate biofilm formation in bacillus subtilis," *PloS one*, vol. 8, no. 5, p. e60993, 2013.

[29] W. Bialek, A. Cavagna, I. Giardina, T. Mora, O. Pohl, E. Silvestri, M. Viale, and A. M. Walczak, "Social interactions dominate speed control in poising natural flocks near criticality," *Proceedings of the National Academy of Sciences*, vol. 111, no. 20, pp. 7212–7217, 2014.

[30] P. J. Steiner, R. J. Williams, J. Hasty, and L. S. Tsimring, "Criticality and adaptivity in enzymatic networks," *Biophysical journal*, vol. 111, no. 5, pp. 1078–1087, 2016.

[31] T. Mora and W. Bialek, "Are biological systems poised at criticality?" *Journal of Statistical Physics*, vol. 144, no. 2, pp. 268–302, 2011.

[32] B. Li and L. You, "Predictive power of cell-to-cell variability," *Quantitative Biology*, vol. 1, no. 2, pp. 131–139, Jun 2013. [Online]. Available: https://doi.org/10.1007/s40484-013-0013-3

[33] O. Symmons and A. Raj, "Whats luck got to do with it: Single cells, multiple fates, and biological nondeterminism," *Molecular Cell*, vol. 62, no. 5, pp. 788 – 802, 2016. [Online]. Available: http://www.sciencedirect.com/science/article/pii/S1097276516301861

[34] B. E. Steinberg, L. Glass, A. Shrier, and G. Bub, "The role of heterogeneities and intercellular coupling in wave propagation in cardiac tissue," *Philosophical Transactions of the Royal Society A: Mathematical, Physical and Engineering Sciences*, vol. 364, no. 1842, pp. 1299–1311, 2006.

[35] S. G. Waxman, "Axonal conduction and injury in multiple sclerosis: the role of sodium channels," *Nature Reviews Neuroscience*, vol. 7, no. 12, p. 932, 2006.

[36] J. W. Larkin, X. Zhai, K. Kikuchi, S. E. Redford, A. Prindle, J. Liu, S. Greenfield, A. M. Walczak, J. Garcia-Ojalvo, A. Mugler *et al.*, "Signal percolation within a bacterial community," *Cell systems*, vol. 7, no. 2, pp. 137–145, 2018.

[37] D. Stauffer and A. Aharony, *Introduction to percolation theory*. Taylor & Francis, 1994.

[38] K. P. T. Silva, T. I. Yusufaly, P. Chellamuthu, and J. Q. Boedicker, "Disruption of microbial communication yields a two-dimensional percolation transition," *Physical Review E*, vol. 99, no. 4, p. 042409, 2019.

[39] I. Breskin, J. Soriano, E. Moses, and T. Tlusty, "Percolation in living neural networks," *Physical review letters*, vol. 97, no. 18, p. 188102, 2006.

[40] J.-P. Eckmann, O. Feinerman, L. Gruendlinger, E. Moses, J. Soriano, and T. Tlusty, "The physics of living neural networks," *Physics Reports*, vol. 449, no. 1-3, pp. 54–76, 2007.

[41] B. Gönci, V. Németh, E. Balogh, B. Szabó, Á. Dénes, Z. Környei, and T. Vicsek, "Viral epidemics in a cell culture: novel high resolution data and their interpretation by a percolation theory based model," *PloS one*, vol. 5, no. 12, p. e15571, 2010.

[42] R. K. P. Benninger, M. Zhang, W. S. Head, L. S. Satin, and D. W. Piston, "Gap junction coupling and calcium waves in the pancreatic islet," *Biophysical Journal*, vol. 95, no. 11, pp. 5048–5061, 2008.

[43] A. Mathijssen, J. Culver, M. S. Bhamla, and M. Prakash, "Collective intercellular communication through ultra-fast hydrodynamic trigger waves," *Nature*, vol. 571, pp. 560–564, 2019.

[44] J. Liu, A. Prindle, J. Humphries, M. Gabalda-Sagarra, M. Asally, D. yeon D. Lee, S. Ly, J. Garcia-Ojalvo, and G. M. Sel, "Metabolic co-dependence gives rise to collective oscillations within biofilms," *nature*, vol. 523, pp. 550–554, 7 2015.

[45] A. Prindle, J. Liu, M. Asally, S. Ly, J. Garcia-Ojalvo, and G. M. Sel, "Ion channels enable electrical communication in bacterial communities," *nature*, vol. 527, p. 5963, 11 2015.

[46] J. Humphries, L. Xiong, J. Liu, A. Prindle, F. Yuan, H. A. Arjes, L. Tsimring, and G. M. Süel, "Species-independent attraction to biofilms through electrical signaling," *Cell*, vol. 168, no. 1-2, pp. 200–209, 2017.

[47] X. Shao, A. Mugler, J. Kim, H. J. Jeong, B. R. Levin, and I. Nemenman, "Growth of bacteria in 3-d colonies," *PLoS computational biology*, vol. 13, no. 7, p. e1005679, 2017.

[48] A. Weinrib, "Long-range correlated percolation," *Physical Review B*, vol. 29, no. 1, p. 387, 1984.

[49] A. Clauset, C. R. Shalizi, and M. E. Newman, "Power-law distributions in empirical data," *SIAM review*, vol. 51, no. 4, pp. 661–703, 2009.

[50] J. W. Essam, "Percolation theory," *Reports on progress in physics*, vol. 43, no. 7, p. 833, 1980.

[51] J. E. Steif, "A survey of dynamical percolation," in *Fractal geometry and stochastics IV*. Springer, 2009, pp. 145–174.

[52] A. A. Saberi, "Recent advances in percolation theory and its applications," *Physics Reports*, vol. 578, pp. 1–32, 2015.

[53] N. Goldenfeld, *Lectures on phase transitions and the renormalization group*. CRC Press, 2018.

[54] J. Wang, Z. Zhou, W. Zhang, T. M. Garoni, and Y. Deng, "Bond and site percolation in three dimensions," *Physical Review E*, vol. 87, no. 5, p. 052107, 2013.

[55] A. Eldar and M. B. Elowitz, "Functional roles for noise in genetic circuits," *Nature*, vol. 467, no. 7312, p. 167, 2010.

[56] R. Chen, S. B. Guttenplan, K. M. Blair, and D. B. Kearns, "Role of the σd-dependent autolysins in bacillus subtilis population heterogeneity," *Journal of bacteriology*, vol. 191, no. 18, pp. 5775–5784, 2009.

[57] T. M. Norman, N. D. Lord, J. Paulsson, and R. Losick, "Memory and modularity in cell-fate decision making," *Nature*, vol. 503, no. 7477, p. 481, 2013.

[58] K. P. Silva, P. Chellamuthu, and J. Q. Boedicker, "Signal destruction tunes the zone of activation in spatially distributed signaling networks," *Biophysical journal*, vol. 112, no. 5, pp. 1037–1044, 2017.

[59] S. E. Darch, O. Simoska, M. Fitzpatrick, J. P. Barraza, K. J. Stevenson, R. T. Bonnecaze, J. B. Shear, and M. Whiteley, "Spatial determinants of quorum signaling in a pseudomonas aeruginosa infection model," *Proceedings of the National Academy of Sciences*, vol. 115, no. 18, pp. 4779–4784, 2018.

[60] T. E. Angelini, E. Hannezo, X. Trepat, J. J. Fredberg, and D. A. Weitz, "Cell migration driven by cooperative substrate deformation patterns," *Physical review letters*, vol. 104, no. 16, p. 168104, 2010.

[61] P. Friedl, Y. Hegerfeldt, and M. Tusch, "Collective cell migration in morphogenesis and cancer," *International Journal of Developmental Biology*, vol. 48, no. 5-6, pp. 441–449, 2004.

[62] P. Martin and S. M. Parkhurst, "Parallels between tissue repair and embryo morphogenesis," *Development*, vol. 131, no. 13, pp. 3021–3034, 2004.

[63] S. Prakash, S. Havlin, M. Schwartz, and H. E. Stanley, "Structural and dynamical properties of long-range correlated percolation," *Physical Review A*, vol. 46, no. 4, p. R1724, 1992.

[64] M. Sahimi and S. Mukhopadhyay, "Scaling properties of a percolation model with long-range correlations," *Physical Review E*, vol. 54, no. 4, p. 3870, 1996.

[65] H. A. Makse, J. S. Andrade, M. Batty, S. Havlin, H. E. Stanley *et al.*, "Modeling urban growth patterns with correlated percolation," *Physical Review E*, vol. 58, no. 6, p. 7054, 1998.

[66] M. Sahimi, "Non-linear and non-local transport processes in heterogeneous media: from long-range correlated percolation to fracture and materials breakdown," *Physics Reports*, vol. 306, no. 4-6, pp. 213–395, 1998.

[67] S. Kundu and S. Manna, "Percolation model with an additional source of disorder," *Physical Review E*, vol. 93, no. 6, p. 062133, 2016.

[68] H. Ikeda, "Percolation in anisotropic systems: real-space renormalization group," *Progress of Theoretical Physics*, vol. 61, no. 3, pp. 842–849, 1979.

[69] E. Meijering, O. Dzyubachyk, and I. Smal, "Methods for cell and particle tracking," in *Methods in enzymology*. Elsevier, 2012, vol. 504, pp. 183–200.

[70] M. Ballerini, N. Cabibbo, R. Candelier, A. Cavagna, E. Cisbani, I. Giardina, V. Lecomte, A. Orlandi, G. Parisi, and A. Procaccini, "Interaction ruling animal collective behavior depends on topological rather than metric distance: evidence from a field study," *Proceedings of the National Academy of Sciences of the United States of America*, vol. 105, no. 4, pp. 1232–1237, 2008.

[71] E. Ben-Jacob, I. Cohen, and H. Levine, "Cooperative self-organization of microorganisms," *Advances in Physics*, vol. 49, no. 4, pp. 395–554, 2000.

[72] M. R. Flynn, A. R. Kasimov, J. C. Nave, R. R. Rosales, and B. Seibold, "Self-sustained nonlinear waves in traffic flow," in *Physical Review E*, 2009, p. 056113.

[73] T. Danino, O. Mondragnpalomino, L. Tsimring, and J. Hasty, "A synchronized quorum of genetic clocks." *Nature*, vol. 463, no. 7279, pp. 326–30, 2010.

[74] T. C. Schelling, "Dynamic models of segregation," *Journal of Mathematical Sociology*, vol. 1, no. 2, pp. 143–186, 1971.

[75] J. Noorbakhsh, D. J. Schwab, A. E. Sgro, T. Gregor, and P. Mehta, "Modeling oscillations and spiral waves in dictyostelium populations," *Physical Review E Statistical Nonlinear & Soft Matter Physics*, vol. 91, no. 6, p. 062711, 2015.

[76] M. Meier-Schellersheim, "Multi-scale modeling in cell biology," *Wiley Interdiscip Rev Syst Biol Med*, vol. 1, no. 1, p. : 414., 2009.

[77] A. A. Qutub, G. F. Mac, E. D. Karagiannis, P. Vempati, and A. S. Popel, "Multiscale models of angiogenesis," *IEEE Engineering in Medicine & Biology Magazine the Quarterly Magazine of the Engineering in Medicine & Biology Society*, vol. 28, no. 2, pp. 14–31, 2009.

[78] J. Southern, J. Pitt-Francis, J. Whiteley, D. Stokeley, H. Kobashi, R. Nobes, Y. Kadooka, and D. Gavaghan, "Multi-scale computational modelling in biology and physiology," *Progress in Biophysics and Molecular Biology*, vol. 96, no. 1, pp. 60 – 89, 2008, cardiovascular Physiome.

[79] T. Lilienkamp, J. Christoph, and U. Parlitz, "Features of chaotic transients in excitable media governed by spiral and scroll waves." *Phys.rev.lett*, vol. 119, no. 5, 2017.

[80] X. Zhai, J. W. Larkin, K. Kikuchi, S. E. Redford, G. M. Süel, and A. Mugler, "Statistics of correlated percolation in a bacterial community," *arXiv preprint arXiv:1906.06450*, 2019.

[81] G. Bub and A. Shrier, "Propagation through heterogeneous substrates in simple excitable media models," *Chaos*, vol. 12, no. 12, pp. 747–753, 2002.

[82] S. Kinoshita, M. Iwamoto, K. Tateishi, N. J. Suematsu, and D. Ueyama, "Mechanism of spiral formation in heterogeneous discretized excitable media." *Physical Review E Statistical Nonlinear & Soft Matter Physics*, vol. 87, no. 6, p. 062815, 2013.

[83] M. Uzzaman, H. Honjo, Y. Takagishi, L. Emdad, A. I. Magee, N. J. Severs, and I. Kodama, "Remodeling of gap junctional coupling in hypertrophied right ventricles of rats with monocrotaline-induced pulmonary hypertension," *Circulation Research*, vol. 86, no. 8, pp. 871–878, 2000.

[84] G. Bub, A. Shrier, and L. Glass, "Spiral wave generation in heterogeneous excitable media." *Physical Review Letters*, vol. 88, no. 5, p. 058101, 2002.

[85] O. Steinbock, P. Kettunen, and K. Showalter, "Anisotropy and spiral organizing centers in patterned excitable media," *Science*, vol. 269, no. 5232, pp. 1857–1860, 1995.

[86] M. R. Tinsley, A. F. Taylor, Z. Huang, and K. Showalter, "Complex organizing centers in groups of oscillatory particles." *Physical Chemistry Chemical Physics Pccp*, vol. 13, no. 39, pp. 17 802–17 808, 2011.

[87] R. Toth, L. C. B. De, C. Stone, J. Masere, A. Adamatzky, and L. Bull, "Spiral formation and degeneration in heterogeneous excitable media." *Physical Review E Statistical Nonlinear & Soft Matter Physics*, vol. 79, no. 2, p. 035101, 2009.

[88] M. Gmez-Gesteira, G. Fernndez-Garca, A. P. Muuzuri, V. Prez-Muuzuri, V. I. Krinsky, C. F. Starmer, and V. Prez-Villar, "Vulnerability in excitable belousov-zhabotinsky medium: from 1d to 2d," *Physica D Nonlinear Phenomena*, vol. 76, no. 4, pp. 359–368, 1994.

[89] R. R. Aliev, "Heart tissue simulations by means of chemical excitable media," *Chaos Solitons & Fractals*, vol. 5, no. 34, pp. 567–574, 1995.

[90] A. M. Pertsov, J. M. Davidenko, R. Salomonsz, W. T. Baxter, and J. Jalife, "Spiral waves of excitation underlie reentrant activity in isolated cardiac muscle." *Circulation research*, vol. 72, no. 3, pp. 631–650, 1993.

[91] S. Zimik, R. Majumder, and R. Pandit, "Ionic-heterogeneity-induced spiral- and scroll-wave turbulence in mathematical models of cardiac tissue," *arXiv preprint arXiv:1807.04546*, 2018.

[92] G. Kastberger, E. Schmelzer, and I. Kranner, "Social waves in giant honeybees repel hornets," *PLoS ONE*, vol. 3, no. 9, p. e3141, 2008.

[93] R. FitzHugh, "Impulses and physiological states in theoretical models of nerve membrane," *Biophysical Journal*, vol. 1, no. 6, pp. 445–466, 1961.

[94] J. Nagumo, S. Arimoto, and S. Yoshizawa, "An active pulse transmission line simulating nerve axon," *Proceedings of the Ire*, vol. 50, no. 10, pp. 2061–2070, 1962.

[95] A. L. Hodgkin and A. F. Huxley, "Currents carried by sodium and potassium ions through the membrane of the giant axon of loligo," *Journal of Physiology*, vol. 116, no. 4, p. 449, 1952.

[96] G. M. Osman and O. Toshiyuki, "Alternans and spiral breakup in an excitable reaction-diffusion system: A simulation study:," *International Scholarly Research Notices,2014,(2014-11-12)*, vol. 2014, no. 3-4, p. 14 pages, 2014.

[97] H. Tuckwell, *Introduction to theoretical neurobiology.* The Pitt Building, Trumpington Street, Cambridge CB2 1 RP: the Press Syndicate of the University of Cambridge, 1988.

[98] R. E. Mirollo and S. H. Strogatz, "Synchronization of pulse-coupled biological oscillators," *SIAM Journal on Applied Mathematics*, vol. 50, no. 6, pp. 1645–1662, 1990.

[99] S. D and A. A, *Introduction to percolation theory.* Boca Raton, FL: CRC Press, 1994.

[100] A. Mathijssen, J. Culver, M. S. Bhamla, and M. Prakash, "Collective intercellular communication through ultra-fast hydrodynamic trigger waves," *Nature*, vol. 571, pp. 560–564, 2019.

[101] G. D. Potter, T. A. Byrd, A. Mugler, and B. Sun, "Communication shapes sensory response in multicellular networks," *Proceedings of the National Academy of Sciences*, vol. 113, no. 37, pp. 10 334–10 339, 2016.

[102] A. Mugler, M. Kittisopikul, L. Hayden, J. Liu, C. H. Wiggins, G. M. Süel, and A. M. Walczak, "Noise expands the response range of the bacillus subtilis competence circuit," *PLoS computational biology*, vol. 12, no. 3, p. e1004793, 2016.